technische universität
dortmund

FGF4 drives intermittent oscillations of ERK activity in mouse embryonic stem cells

Dhruv Raina

Fakultät für Chemie und Chemische Biologie

Technische Universität, Dortmund

Zur Erlangung des akademischen Grades eines

Doktors der Naturwissenschaften (Dr. rer. nat.)

April 2021

Declaration

Vorgelegt im April 2021
Gutachter:
Dr. Aneta Koseska
Prof. Dr. Philippe Bastiaens

The work presented in this dissertation was performed in the group of Dr. Christian Schröter at the Department of Systemic Cell Biology, Max Planck Institute of Molecular Physiology, Dortmund, Germany

Dhruv Raina was affiliated to the International Max Planck Research School in Chemical and Molecular Biology, Dortmund, Germany

The work described in this thesis has been partly included in the following publication:
Raina D, Fabris F, Morelli LG, Schröter C. 2020. Intermittent ERK oscillations downstream of FGF in mouse embryonic stem cells. *bioRxiv* doi:10.1101/2020.12.14.422687

Abstract

Signal transduction systems often display complex activation patterns in response to steady-state ligand stimulation. It has been hypothesized that cells use signal transduction dynamics to encode information about the concentration or identity of the stimuli, but rigorous testing of this idea requires systematic characterisation of single cell responses in defined environments. Here, I used live-cell sensors to study ERK activity dynamics in mouse embryonic stem cells (ESCs) in response to fibroblast growth factor (FGF) stimulation, the main trigger for ESC differentiation and lineage commitment. I detected previously undescribed rapid and regular pulses of ERK activity in pluripotent ESCs. Using *Fgf4* mutant cells, I showed that paracrine FGF was the main driver of ERK pulses. ERK activity dynamics were heterogeneous between cells, ranging from oscillatory to stochastic behaviours. Additionally, single cells showed the ability to transit between oscillatory and non-oscillatory behaviour, leading to intermittent clusters of regular pulsing. With increasing FGF4 dose, clusters of pulses became more prevalent and pulse frequency increased correspondingly, although the duration of individual pulses had a characteristic timescale that was maintained. Increasing FGF4 dose also increased the basal phospho-ERK levels in single cells. The data in this thesis proposes that ligand levels are reflected in the combination of both the basal ppERK level, as well as the pulse frequency.

Zusammenfassung

Zelluläre Signaltransduktionssysteme erzeugen nach Stimulation mit konstanten Konzentrationen von Signalmolekülen oft komplexe dynamische Aktivierungsmuster. Zellen können diese Aktivierungsmuster nutzen, um Informationen über die Konzentration oder Identität der Stimuli zu übertragen. Um die Funktion dynamischer Aktivierungsmuster in spezifischen Zellsystemen zu verstehen, ist es notwendig, Einzelzellantworten in definierten Umgebungen systematisch zu charakterisieren.

Der Fibroblasten-Wachstumsfaktor (Fibroblast Growth Factor, FGF) ist ein zentrales Signalmolekül das die Differenzierung pluripotenter embryonaler Stammzellen (embryonic stem cells, ESCs) steuert. In dieser Arbeit habe ich Live-Zell-Sensoren verwendet, um die ERK-Aktivitätsdynamik ESCs der Maus nach FGF-Stimulation zu untersuchen.

Durch meine Experimente konnte ich bisher unbeschriebene schnelle und regelmäßige Pulse der ERK-Aktivität in ESCs nachweisen. Mithilfe von Fgf4-mutierten Zellen konnte ich zeigen, dass diese ERK-Pulse im Wesentlichen durch parakrine FGFs ausgelöst werden. Die Dynamik der ERK-Aktivität in ESC-Kulturen ist heterogen und reicht von oszillatorischem bis zu stochastischem Verhalten. Einzelne Zellen zeigen außerdem die Fähigkeit, zwischen oszillatorischem und nicht-oszillatorischem Verhalten zu wechseln, ein Verhalten das sich im Auftreten von Clustern von regelmäßigen Pulsen niederschlägt. Solche Cluster treten mit zunehmender FGF4-Dosis vermehrt auf, und die Pulsfrequenz nimmt entsprechend zu, wobei die Dauer der einzelnen Pulse allerdings eine charakteristische Zeitskala hat die unabhängig von der FGF-Dosis ist. Mit zunehmender FGF4-Dosis steigt zudem der basalen phospho-ERK-Spiegel in einzelnen Zellen an. Zusammen legen diese Daten nahe, dass das FGF/ERK Signaltransduktionssystem in ESCs Information über die Konzentration von FGF-Liganden in einer Kombination aus basalem ppERK-Spiegel und ERK-Pulsfrequenz überträgt.

"It was like walking through a door, going all around the world, and then walking through the same door but a different door."

- John Fowles

Acknowledgements

First and foremost: I would like to acknowledge the support and encouragement that Dr. Christian Schröter has given me over the years. Your mentorship and generosity with both time and advice have been invaluable. I will forever be grateful for your patience, your careful editing, and the constant stream of inspirational ideas.

Prof. Dr. Philippe Bastiaens, Dr. Aneta Koseska, and Dr. Peter Bieling for creating this incredible department filled with creativity, challenging ideas and debate, and where stepping out of your comfort zone is so normalized. I have grown enormously from listening and speaking to you all. I remain deeply grateful for all your advice throughout this project.

Our close collaborators: Dr. Luis Morelli and Fiorella Fabris – thank you for your insights, the countless hours of fruitful discussion, and all the *dulce de leche*! It has been a wonderful journey to see our ideas take shape.

To the lab: 'magic-hands' Michelle for somehow getting every experiment right the first time, Marina, Caro, Philip, Kristin, Sina, Max, and Julia – thank you all for the laughs, the conversations, the drinks, and the endless help in the lab.

To my colleagues in the Department who've welcomed me into this family with open arms and big smiles – Lißaweta, Manuela, Frau Schütz, Jutta, Kirsten, Michael Schulz, Malte, Astrid, and Tanja - thank you all for helping me get organized, for everything science-related, and for all the mountains of cake. Sven, thank you for always taking the time to dive into the nitty-gritties of microscopes with me.

Thank you Maitreyi, Akhilesh, Abhishek, Bruno, Jan, and Holger for always finding the time to help me troubleshoot lab and non-lab challenges!

Sarah, Ilaria, Johanna, Michael Reichl, Hans, Konstantin, and Lena – thank you for the friendship and always taking the time to include me. You've made the last few years wonderful and positively crammed with great memories. The Hombruch boys+1: Farid, Angel, Amit, Andrej, Wayne and Mike – for debates about diffusion, for videogames, for food, for hikes, for sanity, and above all, camaraderie – thank you.

To Tia, Adi, and the rest of my family – words cannot express how indispensable your support has been.

To Swastika, for being my sounding-board and my inspiration - without you by my side, I would have never taken this first big step into outer space.

Table of Contents

List of Figures

List of Tables

1 Introduction

1.1 How do cells sense signals?

In order to co-ordinate behaviour across all levels of organization, cells need to respond to both chemical and mechanical cues by constantly sampling their environment. This multitude of signalling cues is integrated and ultimately converted into patterns of protein activity that dictate the response of a cell to either modify the signalling field, or to undergo molecular reorganisation. While there exists a bewildering array of chemical signals that cells respond to (Alberts et al., 2002), explicit detection of molecules is often carried out by the interaction of a signalling ligand with its cognate receptor.

1.1.1 RTK signalling

Enzyme-linked receptors, such as the *receptor tyrosine kinases* (RTKs), typically consist of an extra-cellular domain responsible for ligand interaction, a single-pass trans-membrane alpha-helix that passes through the lipid membrane, and an intra-cellular domain capable of catalysing phosphorylation of tyrosine residues. In the case of growth factors such as the *fibroblast growth factor* (FGF) or *epidermal growth factor* (EGF), binding of extra-cellular ligands results in changes both in the conformation of individual receptors, as well as in their organisation on the membrane. This molecular reorganization triggers tyrosine kinase activity in the cytoplasmic domain of the receptors which is crucial for signal propagation within the cell, hence their name.

Many receptor-ligand combinations have distinct stoichiometries of association and routes to receptor activation. Growth factors such as *nerve growth factor* (NGF) and

the stem cell factor KIT can facilitate dimerization and activation of their RTKs through directly binding to two receptors at once, thereby positioning them for phosphorylation in *trans* (Yuzawa et al., 2007; Wiesmann et al., 1999). For other ligands like EGF, association between receptors can occur ligand-independently (Reviewed in Purba et al., 2017). In the case of FGFs, full receptor activation requires not only FGF and the FGF receptors, but also the co-factor *heparin sulphate proteoglycan* molecules (HSPGs). These co-factors have been variously described to participate either by creating a bridge between two FGF-FGFR complexes (Pellegrini et al., 2000), or through stabilisation of individual receptor-ligand complexes and facilitating protein-protein interactions between them (Schlessinger et al., 2000). RTKs are activated following phosphorylation of key amino acid residues either in *cis* or in *trans*, resulting in increased catalytic efficiency of the cytoplasmic kinase regions. Additional phosphorylated tyrosines within the cytoplasmic domain of the receptor act as docking sites for a number of accessory molecules and are instrumental in transducing the signal downstream. These interactions are primarily driven by 'modular' recognition domains such as the SH2/SH3 or phospho-tyrosine recognition domains on various docking proteins. While some docking proteins, such as Grb2 can promiscuously bind to different receptors and therefore see use in transducing several different signals (Reviewed in Belov & Mohammadi, 2012), others like the adaptor protein FRS2a, which binds to activated FGFRs, are more specific (Kouhara et al., 1997). These docking proteins are typically phosphorylated by their proximity to the catalytic domain of the activated RTK, and thus serve up an additional array of phospho-sites, enabling downstream signal propagation.

1.1.2 The MAPK module

The *mitogen associated protein kinase* (MAPK) signalling module is one such network that is activated downstream of FGF receptor activation. The Ras superfamily of monomeric GTPases is a central player in propagating RTK signals. Ras proteins are tethered to the membrane and are activated by *guanine exchange factors* (GEFs)

which exchange the Ras-bound GDP nucleotide for a GTP nucleotide. Adaptor proteins such as Grb2 can recruit the GEF *son-of-sevenless* (SOS) to the membrane upon receptor activation, thus positioning it to catalyse activation of the Ras proteins. The activated Ras-GTP then transmits the signal from the activated receptor at the membrane to proteins within the cytoplasm through phosphorylation and activation of a series of serine/threonine kinases called the MAPKs. 'Modules' of MAPK signalling comprise a cascade of phosphorylation reactions – starting with the *MAP kinase kinase kinases* (MAPKKKs), which activate the *MAP kinase kinases* (MAPKKs), which then activate the effector MAPKs. Once activated by serine/threonine phosphorylation, the MAPKs can phosphorylate a diverse set of targets in the cytosol and the nucleus in order to direct gene expression and cell state (reviewed in Morrison, 2012).

1.1.3 ERK signalling

A classical MAPK module that is involved in differentiation, growth, proliferation, and cell survival is the Raf-MEK-ERK cascade. Activated Ras-GTP facilitates activation of Raf-family proteins to further propagate the signal (Terrell & Morrison, 2019). Active forms of the Raf proteins subsequently phosphorylate and activate the *MAPK/ERK kinase* (MEK), which in turn phosphorylates and activates the *extracellular signal-regulated kinase* (ERK) proteins.

ERK proteins are serine/threonine kinases that catalyse phosphorylation of proteins at the consensus site S/TP, with the requirement of a proline at the +1 position (Gonzalez et al., 1991). Full activation of ERK1 and 2 requires that they are dually phosphorylated by MEK proteins, resulting in a 1000-fold increase in catalytic activity (Robbins et al., 1993). While both isoforms show a degree of functional redundancy (Reviewed in Eblen, 2018), mouse knockout experiments have demonstrated that *Erk2* knock-outs are embryonic lethal (Hatano et al., 2003), whereas the phenotype of an *Erk1* knock-out is more mild, likely due to partial redundancy (Pagès et al., 1999). As ERK1 and ERK2 are present in different amounts, these phenotypes have

been proposed to be related more to dosage-effects rather than isoform-specific effects (reviewed in Buscà et al., 2016), although in some instances isoform-specific effects have also been shown (Vantaggiato et al., 2006). As a kinase, ERK has diverse roles in activating or repressing transcription factor activity in a context-specific manner (Reviewed in Lavoie et al., 2020). Recent chromatin immunoprecipitation experiments have even shown direct binding of ERK proteins to DNA, suggesting it has a role as a direct modulator of RNA polymerase loading (Tee et al., 2014; Göke et al., 2013). A vast list of ERK target substrates has been assembled into a database showing over 600 direct ERK targets (Ünal et al., 2017), demonstrating the pleiotropic effects of ERK.

Signals from different growth factors and diverse inputs such as integrin signalling (Schlaepfer et al., 1997), TGF-beta signalling (Reviewed in Zhang, 2009), and GPCR signalling (Reviewed in Goldsmith & Dhanasekaran, 2007), among others all converge on the phosphorylation and activation of ERK. Despite this 'hourglass' construction of signalling where many inputs share a few common effector molecules (Kitano, 2004), cells are able to execute distinct ligand-specific responses.

Several models have been proposed to resolve this conundrum. Combinatorial encoding of signal identity, where distinct signals elicit activation of different spatial pools of an effector (Vartak & Bastiaens, 2010; Kholodenko, 2009) or different subsets of common effector molecules might be one means by which stimulus identity is preserved during signal transduction. With advances in multiplexing capabilities, both in fluorophore detection (Cutrale et al., 2017), as well as in protein-staining (Gut et al., 2018), it has become possible to measure the activation state of many effectors simultaneously, and develop a map for combinatorial encoding of ligand identity (Kramer & Pelkmans, 2019). An alternative means of encoding ligand identity that has been described in recent years is the notion of dynamic encoding, wherein different growth factors have been demonstrated to elicit time-resolved differences in ERK activation (Santos et al., 2007; Marshall, 1995).

1.1.4 Feedbacks in FGF/ERK signalling

How are dynamics of protein activity generated within cells? In the simplest case, a delayed negative feedback is sufficient to produce repeated oscillations of protein activity, given appropriate kinetics and timescales (Novák & Tyson, 2008). In the case of MAPK signalling, many levels of feedback have been described (Reviewed in Lake et al., 2016). For signalling via the FGF receptor, direct inhibitory phosphorylation of the receptor by ERK has been demonstrated *in vitro* (Zakrzewska et al., 2013). Additionally, ERK has also been shown to phosphorylate and downregulate activity of the SOS proteins. This regulation is both direct, demonstrated via *in vitro* phosphorylation of SOS-1 by ERK (Corbalan-Garcia et al., 1996), as well as indirectly mediated via activity of the *ribosomal S6 kinase* (RSK-1) protein (Douville & Downward, 1997). Additional prominent feedback links have also been described at the Raf proteins (Reviewed in Lavoie & Therrien, 2015), where phosphorylation by ERK leads to their inactivation.

However, despite this extensive list of possible feedbacks, the exact molecular interactions that predominate in a given signalling context are likely to be a limited subset of these links. The relevant interactions in the diagram shown in **Fig 1.1** will have to be identified for each stimulus regime, and might even show differences in strength or timescale based on the type of stimulus and the identity of the cell. Thus, the precise dynamics of ERK activity and its importance for signalling can vary greatly based on cellular context.

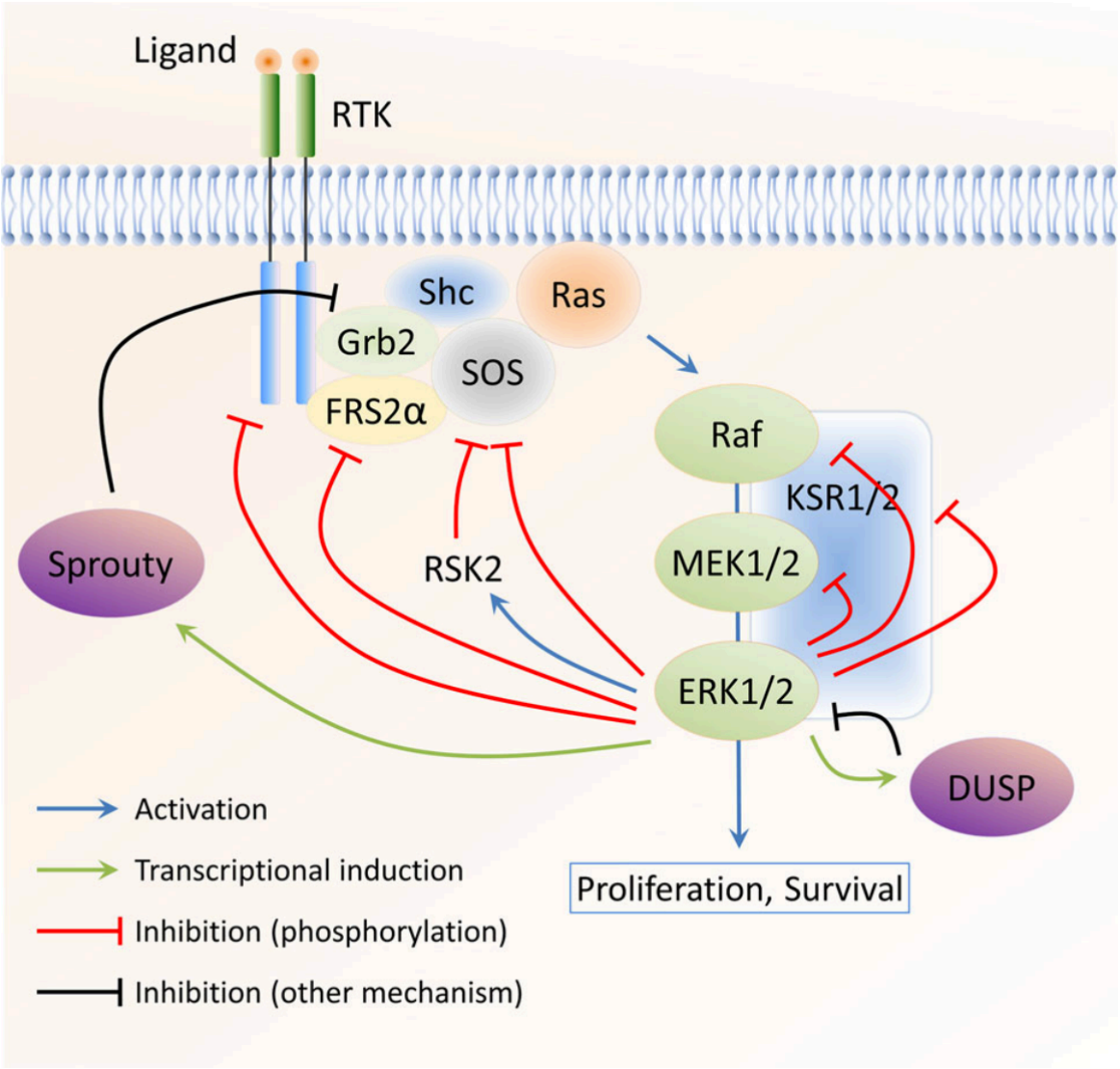

Fig 1.1: Negative feedback links in RTK/MAPK signalling
Links are coloured according the legend displayed in the lower left. Figure reprinted under the CC-BY 4.0 license from Lake et al., 2016.

1.2 Time-resolved dynamics of signalling

The information contained in the dynamics of a protein, comprising the rates of activation and deactivation, or of production and degradation, as well as changes in sub-cellular localisation, is much richer than snapshot measurements made in a cell (Purvis & Lahav, 2013; Behar & Hoffmann, 2010). In a clear demonstration of the information-richness of dynamics, Selimkhanov et al. followed the trajectory of protein activity over time and found that these time-resolved measurements of

activity states can increase the mutual information between the stimulus and the observed protein response (Selimkhanov et al., 2014). With the advent of live-cell imaging and fluorescent reporter technologies, dynamic activity in single cells has been observed in many signalling systems, some of which are described below.

p53, a critical DNA-damage response regulator, regulates transient DNA-repair responses as well as the more terminal responses of apoptosis and senescence. When double-stranded DNA breaks are induced in cells, oscillations of p53 protein levels have been observed, bearing a period of 3-6 h (Geva-Zatorsky et al., 2006; Lahav et al., 2004). These dynamics have been proposed to carry information that regulates cell fate, and the dynamics change based on the degree and type of DNA-damage (Purvis et al., 2012).

Studies on signal transduction of the cytokine TNF-alpha have also demonstrated oscillations of nuclear translocation of the transcription factor NF-kB upon continuous stimulation (Tay et al., 2010). These pulses have a period of approximately 1 hr, and depend on *de novo* protein synthesis through transcriptional feedbacks (Hoffmann et al., 2002). The number of pulses increases with TNF-a concentration, and can differentially regulate gene expression (Tay et al., 2010). In this system, a higher frequency of pulsing has been shown to stimulate 'late' gene products more efficiently than a lower frequency of pulsing (Ashall et al., 2009).

Another signalling system that has shown clear pulsing dynamics in response to stimulation is the Crz-1 calcium-responsive transcription factor in yeast. Higher concentrations of extracellular calcium were shown to increase the frequency of Crz-1 nuclear translocation pulses. One possible benefit of this type of frequency-modulated encoding in a transcription factor is that it could allow an overall increase in expression of multiple genes of a complex regulon, without changing their relative abundances (Cai et al., 2008).

These studies and others have demonstrated that the dynamic behaviour of signalling systems is a generalisable phenomenon, and that the characterisation of these

dynamic behaviours in a novel system can suggest mechanisms for how a signal could be transcriptionally decoded.

1.2.1 Dynamics in ERK activity

RTK signalling through ERK is an area of intense study, and a wide range of ERK activity dynamics have been observed in different contexts. Changes in ERK pulse frequency have been observed in response to EGF concentration (Albeck et al., 2013), cell density (Aoki et al., 2013), or a tissue wound (Mayr et al., 2018; Hiratsuka et al., 2015), demonstrating that ERK dynamics can reflect differences in cell state. Study of these dynamic behaviours has been aided by computational models which explore the underlying network architecture, and are constrained by both the observed dynamics as well the feedback links described in literature.

In mammary epithelial cells, oscillations of ERK nuclear translocation have been reported with a periodicity of approximately 15 mins (Shankaran et al., 2009). These oscillations were initiated upon continuous growth factor stimulation, and showed a reduction in amplitude with increasing cell density and EGF concentration, although the duration of a pulse remained relatively constant (Shankaran et al., 2009). Using computational modelling, Shankaran *et al.* devised a biochemical model for the MAPK cascade with three key features – i.) each phosphorylation and dephosphorylation step was explicitly modelled, ii.) dually phosphorylated ERK exerted negative feedback on the first component of the cascade (the MAPKKK enzyme *Ras*), and iii.) the MEK enzyme was saturated and thus the rate of ERK phosphorylation was independent of total ERK concentration. Under these conditions, their model recapitulated oscillations of total-ERK, and showed that these were likely accompanied by oscillations in dually phosphorylated ERK. This model is part of the family of delayed negative feedback oscillators (see Novák & Tyson, 2008; Tyson et al., 2003) which typically show a narrow frequency-response range (Tsai et al., 2008).

In contrast to these observations, another study described pulses of ERK activity as more stochastic in nature (Aoki et al., 2013). In this study, Aoki *et al.* used a live-cell FRET-based sensor to study ERK activity pulses in rat kidney epithelial cells upon stimulating ERK by increasing cell densities. They found that the frequency of ERK pulses in this system showed a biphasic response to cell density and proliferation, with the highest pulse frequencies at intermediate values. Based on their observations, Aoki *et al.* designed a biochemical model for an oscillator that captures the properties of frequency-modulated response to an input signal, as well as a fixed pulse amplitude that did not show changes with stimulation strength. Their model had the following key characteristics: i.) only two components were considered: the MAPKKK enzyme *Raf* and the MAPK effector *ERK*, ii.) Raf positively upregulates itself, and iii.) active-ERK negatively regulates Raf. This structure is broadly similar to what is termed an 'amplified negative feedback loop' (Novák & Tyson, 2008), or a 'positive-plus-negative-feedback' loop (Tsai et al., 2008). This class of models typically shows a frequency-response that scales with the strength of an input, as well as shows pulses with a fixed amplitude (Tsai et al., 2008).

These studies demonstrate that careful characterisation of ERK dynamics can lay the foundation for biochemical models that help identify the key principles involved in the generation of the dynamic behaviour.

1.3 FGF signalling in development

FGF/ERK signalling coordinates developmental processes across many scales *in vivo*. Individual cells, therefore, need to precisely respond to context-specific FGF cues in order to ensure correct developmental trajectories in the embryo. The mammalian Fgf family consists of 22 related members and shows diverse patterns of expression during development. Canonical Fgfs come from five major families of Fgf genes – the Fgf4-like, Fgf5-like, Fgf8-like, Fgf9-like, and Fgf10-like (**Fig 1.2**). These FGFs are all

secreted into the extracellular space via a conserved signal sequence, and signal through RTK receptors in complex with acidic proteoglycans in the extracellular environment (Reviewed in Itoh & Ornitz, 2008). This requirement for association with proteoglycans is thought to limit their range of diffusion and cause them to act in a paracrine manner (Itoh & Ornitz, 2008). Indeed, recent work has also demonstrated that paracrine FGF4 has a short range of activity in ESCs (Raina et al., 2020b). Canonical Fgfs signal through binding to FGF receptors (FGFRs), and different Fgfs show differing specificity to these receptors (Reviewed in Ornitz & Itoh, 2015). In mammals, four Fgfr genes have been identified, although Fgfrs1-3 each possess two splice variants with differences in their extracellular immunoglobulin-like III domain, resulting in different Fgf binding affinities.

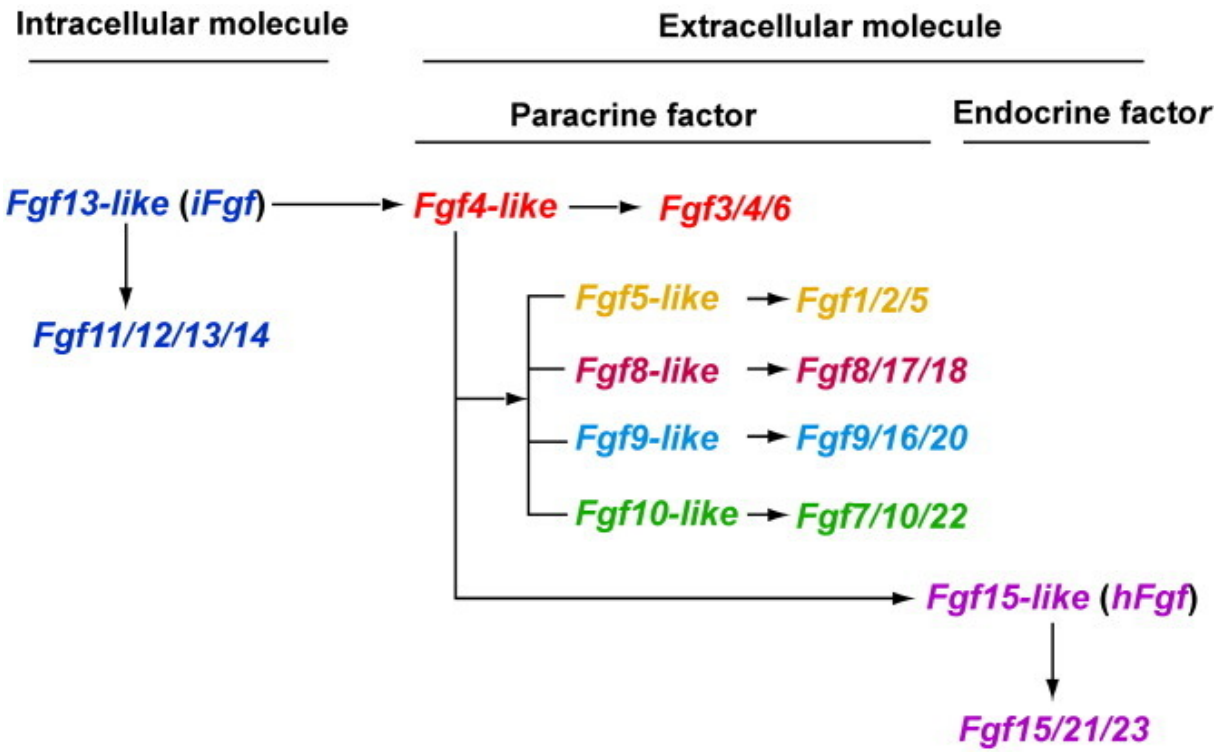

Fig 1.2: Molecular evolution of mammalian Fgf family proteins
Fgf13-like is considered the precursor gene to the family of Fgf molecules. Intracellular Fgfs (iFGFs) are derived from this. The canonical Fgfs comprise the Fgf4-like, the Fgf5-like, Fgf8-like, Fgf9-like, and Fgf 10-like families. The Fgf12-like or hFGF is a an isoform that is present in humans and functions in an endocrine capacity. Figure reproduced from Itoh & Ornitz, 2008, *with permission from the publisher John Wiley and Sons.*

FGF signalling coordinates many developmental processes, and specific FGFs and their receptors are differentially expressed across vertebrate development. Among the earliest instances of FGF-regulated developmental decisions in the mouse is in the pre-implantation embryo. The first major fate commitment event, occurring at the 8-16 cell stage, is the specification of trophectoderm cells which give rise to the foetal placenta, and the cells of the *inner cell mass* (ICM). The maturation of the ICM into cells of the *epiblast* (Epi), which form the organism, or the *primitive endoderm* (PrE), which gives rise to tissues related to the yolk sac, occurs shortly thereafter between the 32 - 100 cell stages. The decision of an ICM cell to form a PrE cell type is based on the sensing of FGF4 signals. Mutational analysis of the *Fgfr1* and *Fgfr2* receptors (Kang et al., 2017; Molotkov et al., 2017) has shown that PrE cells do not develop in the absence of FGF receptors. PrE cells also failed to form upon mutation of the *Fgf4* gene. In these *Fgf4-/-* embryos, PrE differentiation can be rescued by addition of exogenous FGF4 (Kang et al., 2013). Thus, the growth factor FGF4, signalling through receptors FGFR1 and FGFR2 organises fate decisions in the blastocyst.

FGFs can also induce cell migration. Gastrulation, the process of cellular migration and reorganisation through which the three germ layers of the embryo are specified, begins at embryonic day 6.5 of mouse development. Cells from the posterior *epiblast* (Epi) form the primitive streak, and then remaining Epi cells undergo an epithelial-to-mesenchymal transition before ingressing through it. The movement of cells through the primitive streak requires a combination of FGF and Wnt signals (Ciruna & Rossant, 2001). FGF signals have been shown to act as chemokines during chicken gastrulation, and can therefore direct cell migration as well (Yang et al., 2003). In the mouse, cells of the primitive streak and visceral endoderm express *Fgf8* (Sun et al., 1999), and *Fgfr1* (Yamaguchi et al., 1994) is expressed in the embryonic ectoderm. *Fgf8* and *Fgfr1* embryos both show gastrulation defects (Sun et al., 1999; Yamaguchi et al., 1994), suggesting a role for FGFs as chemotactic factors that coordinate morphogenesis.

In neural development, FGFs have been ascribed the role of a morphogen. During gastrulation, a population of epiblast cells called the neuromesodermal progenitor (NMp) cells give rise to the spinal cord and mesodermal tissue. Differentiation of the NMp cells into either mesodermal cell types or neural subtypes depends on a combination of WNT signalling and expression of the *Fgf4* and *Fgf8* ligands in the embryo (Reviewed in Diez del Corral & Morales, 2017). Additionally, in later neural development, FGF8 has been shown to establish the anterior-posterior patterning of the telencephalon (Fukuchi-Shimogori & Grove, 2001), suggesting its ability to act as a morphogen in this context.

These examples demonstrate that precise interpretation of FGF/ERK signals by embryonic cells in essential for coordinating the patterns of multi-cellular and single-cell behaviour across different scales during embryonic development.

1.4 ES cells as a model for developmental decisions

Mouse embryos are highly complex structures, and studying processes within them is extremely challenging for a multitude of technical reasons. In contrast, embryonic stem cells are easy to maintain, and are a powerful *in vitro* tool to model some developmental paradigms. Embryonic stem cells are pluripotent cells derived from the inner cell mass (ICM) of the mouse blastocyst. ES cells can proliferate indefinitely and retain their pluripotency, provided they are correctly maintained in culture. The pluripotency of ES cells means that they have the capacity to differentiate into all the embryonic sub-types of cells given the correct sequence of environmental cues. ES cells can therefore be used to study early lineage decisions with the benefit of accessible *in vitro* experimentation. While the endogenous developmental routes to differentiation of adult tissues cannot be fully mimicked, a wide variety of differentiation protocols have been developed over the years (Reviewed in Keller, 2005).

1.4.1 ERK signalling is critical for the determination of ESC pluripotency

Pluripotency in mouse ES cells is maintained through growth in specialised culture conditions. The most basic medium formulation that supports self-renewal and pluripotency of ES cells contains serum and the cytokine LIF (**Serum + LIF**). LIF is a critical regulator of pluripotency, and signals through the gp130/LIF receptor heterodimer – which are a type of *Janus-associated kinase* (JAK) receptor. Activated JAK receptors enable activation and homodimerization of the transcription factor STAT3, which regulates the core pluripotency network through the action of *Klf4* (Niwa et al., 2009). LIF alone cannot support ES cell pluripotency, and requires additional signals, which are presumably present in serum. One candidate signal is the *bone morphogenetic protein* (BMP) present in the serum and is thought to act in concert with LIF to maintain pluripotency and self-renewal in ES cells (Ying et al., 2003). Thus, in the serum + LIF conditions, which are standard for the maintenance of a heterogeneously pluripotent culture, pluripotency is likely retained through BMP and LIF signals.

In these culture conditions, ES cells also express FGF4 which signals through the FGFR1/FGFR2 receptors to promote differentiation. This paracrine FGF signalling results in a culture that is composed of both undifferentiated and differentiating cells. Indeed, repression of ERK signalling by mutating the *Fgf4* gene results in pluripotent ES cells that are resistant to differentiation, and can be maintained with LIF alone (Kunath et al., 2007). Thus, paracrine FGF4 is the single factor that promotes differentiation in pluripotent ES cell cultures.

Historically, ES cells were derived mostly from the 129 inbred mouse strain as only the ES cells from this line could be propagated in culture (Martello & Smith, 2014). However, with improved understanding of the levers that control pluripotency, ES cell derivation is now possible from a range of organisms (Nichols & Smith, 2009). The primary advance came about with the development of the 2i culture condition and introduction of the concept of 'ground state' pluripotency (Ying et al., 2008). The

2i medium formulation uses a combination of LIF, a GSK3b inhibitor, and an inhibitor of FGF/ERK signalling. LIF has been previously discussed. GSK3b is an effector of Wnt signalling, and the GSK3b inhibitor mimics Wnt stimulation to some extent. However, stimulation with Wnt ligands alone is not as effective as the GSK3b inhibitor, suggesting non-Wnt functions of GSK3b inhibition might be important for the maintenance of pluripotency (Martello & Smith, 2014).

FGF/ERK signalling negatively regulates NANOG expression, thereby pushing cells to differentiate. Inhibition of ERK signalling, which enhances pluripotency, is typically carried out by using either small molecule inhibitors directed against MEK, the kinase that activates ERK, or by using inhibitors of the FGF receptors. Thus, a key defining feature of ES cells is their ability to grow and differentiate in the absence of ERK signalling. ES cells maintained in 2i+LIF transcriptionally resemble epiblast cells of preimplantation embryo, and have low levels of DNA methylation (Boroviak et al., 2014; Leitch et al., 2013), demonstrating their value as a model system to study early developmental decisions.

In conclusion, ES cells present a highly tractable cell culture system that can be used to study various developmental processes *in vitro*. As these cells are independent from the requirement for ERK signalling faced by somatic cell types, they present a study system where ERK signalling can be reduced to very low levels without adverse effects. This low background allows sensitive detection of the FGF-specific changes in ERK activity, without interference from other signalling sources. As most of the ERK activity results from paracrine FGF4, this ES cell system can be an effective proxy for understanding how cells in the embryo accurately sense FGF4 signals and use it to coordinate differentiation.

1.5 Objectives

In this thesis, I have used a translocation-based ERK activity sensor (Regot et al., 2014) to measure rapid ERK activity dynamics in ESCs. The main objectives of this work were to characterise these dynamics, and to understand the extent to which ERK dynamics can encode FGF4 ligand concentration. This thesis develops experimental and data-analysis workflows to characterise these time-series. Using live-cell imaging and tracking, I found that ERK activity was pulsatile and that these pulses occured rapidly, with a modal inter-pulse interval of around 7 minutes. These dynamics were heterogeneous over time, and I was able to determine that ERK pulses frequently occurred in rapid succession or in 'clusters'. Using long-term timelapse imaging revealed that ERK pulsing dynamics changed across the cell cycle. Through use of an *Fgf4* mutant cell line, I was able to determine that ERK pulsing was induced by FGF4 signals. Finally, with a combination of immunostaining and live-imaging, I demonstrated that ERK activity dynamics together with the basal ppERK levels reflects the external ligand concentration.

2 Methods

2.1 Cell culture

mESCs were routinely cultured on 0.1% gelatine (Sigma Aldrich)-coated tissue culture flasks in serum + LIF medium composed of GMEM (ThermoFisher), 10% batch-tested foetal bovine serum (FBS) (Sigma Aldrich), 1x GlutaMAX (ThermoFisher), 1 mM sodium pyruvate (ThermoFisher), 1x non-essential amino acids solution (ThermoFisher), 100 µM 2-mercaptoethanol (ThermoFisher) and 10 ng/ml LIF (MPI protein expression facility). Cells were passaged every two to three days using 0.05% Trypsin (PAN Biotech). Basal medium for serum free culture was N2B27, prepared as a 1:1 mixture of DMEM/F12 (PAN Biotech) and Neuropan basal medium (PAN Biotech) with 0.5% BSA, 1x N2 and 1x B27 supplements (ThermoFisher) and 50 µM 2-mercaptoethanol. For FGF stimulation experiments, overnight serum-free culture was carried out in N2B27 supplemented with 3 µM CHIR99201 (Tocris), 1 µg/ml of Heparin (Sigma) and with or without 10 ng/ml LIF. Recombinant human FGF4 used was obtained from Peprotech. For live imaging and immunostaining studies, cells were seeded on polymer-bottomed ibidi µ-slides (ibidi) coated with 20 µg/ml fibronectin.

2.2 Cell lines

All KTR-expressing cell lines used in this study were derived from E14tg2a (Hooper et al., 1987). Targeting of the ERK-KTR-Clover construct into the Hprt locus to

generate the ERK-KTR cells was described in Simon et al., 2020. Mutagenesis of the Fgf4 gene was performed by M. Protzek according to the procedure described in Morgani et al., 2018. Targeting of the Spry4:H2B-Venus reporter was described in Morgani et al., 2018. For the dual reporter experiments, the ERK-KTR-mCherry construct for transient expression was prepared by H.Vogel by first inserting the coding sequence for ERK-KTR (Regot et al., 2014) into a CMV-driven mCitrine C1 expression vector (TaKaRa), and then replacing the fluorophore for mCherry. The plasmid for transient expression of EKAREV-NLS has been described (Komatsu et al., 2011). 1.5 µg each of plasmid were transiently co-transfected into E14tg2A mouse stem cells using Lipofectamine 2000 (ThermoFisher) in suspension according to manufacturer's instructions. Cells were plated on fibronectin-coated ibidi slides and imaged 24 h after transfection. Cells were maintained in phenol red-free medium.

2.3 Western blotting

Cells were grown to confluency on fibronectin-coated tissue culture dishes and exposed to indicated experimental conditions. Cells were briefly washed twice with ice-cold PBS supplemented with 1 mM activated sodium orthovanadate and then lysed using commercially available lysis buffer (Cell Signaling) supplemented with benzonase (ThermoFisher), phosphatase inhibitor cocktail 2 and 3 (Sigma), and cOmplete EDTA-free protease inhibitor cocktail (Roche). Lysates were snap-frozen in liquid nitrogen. Protein concentration was estimated using a micro-BCA assay (ThermoFisher), and lysates were denatured by adding appropriate amounts of 5x Laemelli buffer and boiling for 5 min. 10 or 20 µg protein was loaded across all wells in any given gel. Bis-Tris SDS gels were run with 1x MOPS buffer (ThermoFisher) with fresh sodium bisulphite, and subsequently transferred onto methanol-activated PVDF membranes (Millipore) at 40 V for 1.5 h with the NuPage transfer system (ThermoFisher). Primary antibodies used were anti-Tubulin 1:5000 (T6074, Sigma),

anti-pERK1/2 1:1000 (4370S, Cell Signaling), and anti-total ERK1/2 1:1000 (ab36991, Abcam) along with appropriate secondary antibodies (LI-COR). Bands were detected using the Odyssey CLx imaging system (LI-COR). Bands were quantified using FIJI/ImageJ (Rueden et al., 2017). For quantification of phospho ERK and total ERK, integrated intensity in both ERK1 and ERK2 bands was added.

2.4 Immunostaining

For phospho-ERK immunostaining, cells were fixed for 15 min at 37°C by diluting fixative stocks directly into cell culture medium to a final concentration of 4% PFA and 0.01% glutaraldehyde (Sigma). After a brief wash with PBS, cells were permeabilized with 100% methanol at -20°C. For all other antibodies, fixation was performed with 4% PFA at room temperature for 20 min. Cells were washed with PBS and then simultaneously blocked and permeabilized with 5% normal goat serum (ThermoFisher) in 0.5% Triton X-100 (Serva) in PBS for 60 min. Antibody staining was carried out overnight at 4°C in PBS + 0.1% Triton X-100 and 1% BSA (Sigma). Primary antibodies used were anti-pERK1/2 1:200 (4370S, Cell Signaling), anti-E-Cad 1:200 (M108, clone ECCD-2, TaKaRa), anti-NANOG 1:200 (eBIO-MLC51), anti-POU5F1 1:200 (C-10, sc-5279, Santa Cruz), along with appropriate secondary antibodies. Hoechst 33342 was used at 1 µg/ml to counter-stain nuclei, and CellMaskRed (ThermoFisher) was used to label membranes according to manufacturer's instructions. After staining, samples were covered with 200 µl of antifade composed of 80% w/v glycerol with 4% w/v N-propyl gallate and stored at 4°C. Images were analysed using custom scripts in MATLAB (The Mathworks) and Fiji/ImageJ for the detection of nuclei as well as an active-contours based identification of membranes.

2.5 Flow cytometry

Cells were grown on fibronectin-coated dishes in N2B27 supplemented with 3 μM CHIR99201, 1 μM PD0325901 and 10 ng/ml LIF (2i + LIF) for 3 days. For stimulation, cells were washed 2x with PBS, and FGF4 was added at indicated concentrations in serum-free N2B27 medium supplemented with 3 μM CHIR99201 and 1 mg/ml Heparin for 24 h. Cells were then trypsinized and fixation was performed in suspension with 4% paraformaldehyde at room temperature for 15 min. After a brief wash in PBS, cells were resuspended in PBS + 1% BSA and analysed on a BD-LSR II (BD Biosciences) flow cytometer. Data were analysed in FlowJo (BD Biosciences).

2.6 Image segmentation

2.6.1 Immunostaining

All immunostaining quantification required the identification of cell boundaries and nuclei. Nuclei needed to first be accurately identified, and then cytoplasmic masks were generated on the basis of the nuclear masks. As nuclei were frequently in close contact with each other, segmentation was performed in two parts – an appropriate mask of the nuclear image was first constructed, and then the masks were split to separate touching nuclei. In brief, the nuclear image was tophat filtered with a disc of radius 50 px in order to correct uneven background. Morphological reconstruction was used to preserve large objects (i.e. the nuclei) and reduce intensity variance within the nuclei. Images were then thresholded and converted to binary masks. Masks were eroded by 1-2 px to ensure nuclear masks did not spill over the borders of the nucleus. Nuclear masks were split using distance-transform watershed, and masks were morphologically opened to smoothen out the boundaries. The resultant nuclear masks were manually curated to ensure they accurately tracked the boundaries of a nucleus as this was an essential requirement for building accurate

cytoplasmic masks. To create cytoplasmic masks, cell boundaries in the cytoplasmic images were first enhanced by running a morphological gradient with a disc structuring element of radius 1 px. Cell boundary masks were generated by using the segmented nuclear images as a 'seed' for an active contours boundary growth algorithm. To generate cytoplasm-only masks, the nuclear masks were dilated by 2 px and then XOR'ed with the cell boundary mask. As the cytoplasmic ROIs (region-of-interest) were saved as a modification of the nuclear ROIs, both cytoplasm and nuclear masks had the same ROI identification numbers, and could be linked in MATLAB to calculate per-cell properties.

2.6.2 Enhancing images for Trackmate

As nuclear images had low intensity, they were first enhanced frame-by-frame in MATLAB before running Trackmate. First, saturated pixels were deleted, and objects of the correct size were enhanced using a combination of a tophat filter, image opening, and morphological reconstruction. A distance-transform watershed was then performed, and masks for individual cells were generated. Masks were multiplied by a distance transform and the original image in order to make the centres of the masked nuclei brighter than the edges. This artificial gradient introduced in the nuclear images facilitated proper centring of the ROIs when using the auto-tracking feature of Trackmate.

2.7 Live-cell imaging and tracking

For all live-imaging experiments, cell were maintained on fibronectin-coated ibidi µ-slides, and imaged on a Leica SP8 confocal microscope equipped with an incubation chamber and CO_2 supply to maintain temperature at 37°C, CO_2 at 5%, and relative humidity at 80%. For experiments with multiple fluorophores, simultaneous excitation

and collection of light was performed, except where indicated. Tracking was performed using the TrackMate plugin (Tinevez et al., 2017) for ImageJ (Rueden et al., 2017).

2.7.1 Dual reporter imaging

Imaging was performed using a 63X 1.4 NA objective and a wide pinhole aperture of 2.4 a.u. Sequential excitation of the FRET donor (CFP) and the KTR sensor (mCherry) was carried out by illumination with 458 nm and 576 nm laser lines. Emission filters of 469-495 nm, 518-545 nm, and 590-675 nm were used to collect light from all three sources and detected with separate HyD detectors.

2.7.2 High-resolution imaging

For short term imaging experiments, 4 h before acquisition, live-cell nuclear dye SiR-Hoechst 652/674 (Spirochrome) was added at 500nM to facilitate tracking of cells. Single frames were acquired once every 20 s, with an XY resolution of 251 nm, a pixel dwell time of 2.6 µs, and a pinhole of 2.4 airy units. Images of the ERK-KTR-mClover (excitation: 500 nm / emission: 511-553 nm) and SiR-Hoechst (excitation: 640 nm / emission 653-695 nm) were simultaneously captured through a 1.2 NA 63X water objective.

2.7.3 Low-resolution, long-term imaging

For long term (~19 h) imaging experiments, live-cell nuclear dye SiR-Hoechst 652/674 (Spirochrome) was added at 250nM overnight to facilitate tracking of cells. To minimize overall light exposure single frames were acquired once every 105 s, with an XY resolution of 401 nm, with a pixel dwell time of 3.1 µs, and a pinhole of 2.6 airy units. Images of the ERK-KTR-mClover (excitation: 500 nm / emission: 511-553 nm) and SiR-Hoechst (excitation: 640 nm / emission 653-695 nm) were simultaneously captured through a 1.4 NA 63X objective. Nuclear images were processed with

custom MATLAB scripts to enhance contrast and highlight nuclei to facilitate automatic tracking.

2.7.4 Transient stimulation experiments

4 h before acquisition, live-cell nuclear dye SiR-Hoechst 652/674 (Spirochrome) was added at 500 nM to facilitate tracking of cells. Single frames were acquired once every 60 s or 70 s as indicated, with an XY resolution of 248 nm and a pinhole of 2.5 airy units. Medium containing FGF was changed on the microscope at the indicated times in the experiment. Images of the ERK-KTR-mClover (excitation: 500 nm / emission: 511-553 nm) and SiR-Hoechst (excitation: 640 nm / emission 653-695 nm) were simultaneously captured through a 1.2 NA 63X water objective.

2.7.5 Tracking

Tracking was performed using the Trackmate plugin for FIJI/ImageJ. Tracking was initially performed automatically for the entire colony using the contrast-enhanced and nuclear segmented images, and tracks were subsequently manually curated frame-by-frame by removing any cells that did not display a typical ESC morphology with a small cytoplasm and round, well-defined nuclei. I also removed cells that left the field of view, and adjusted tracking in individual frames for incorrectly identified nuclei. I inverted fluorescence values to obtain the negative image, and then measured mean fluorescence intensities in a region of interest (ROI) of variable size within each tracked nucleus. In these KTR signal traces, low intensity values correspond to low ERK activity and high intensity values indicate high ERK activity. For the short-term imaging, tracks started at the beginning of the movie and extended until the end of the movie, or until cell division. As the long-term imaging experiments were designed to capture the entire cell cycle, tracks started in the first frame following cell division where a cell could be tracked, and ended at cell division. In these experiments, we kept tracks of cells that left the field of view, but only if they were observed for longer than 4.5 h.

2.8 Data analysis

2.8.1 Analysis of dual-reporter experiments

Ratiometric FRET for the EKAREV reporter was calculated by first masking nuclei and then calculating $\frac{\text{Emission}_{Acceptor}}{\text{Emission}_{Donor}}$ upon Donor excitation on a pixel-by-pixel basis as previously reported (Aoki & Matsuda, 2009). FRET sensor-only controls were performed to rule out interference from the KTR sensor. In the ratiometric images, single cells were manually tracked using the TrackMate plugin for ImageJ, and average ratiometric value within a nuclear ROI was recorded. The same tracks were then overlaid onto the intensity inverted KTR-mCherry channel, and KTR sensor values were read-out from the same ROIs. As both sensors had vastly different signal intensities, amplitudes were scaled by standardization. Briefly, the mean of every track was subtracted from its values, and the result was divided by the standard deviation. This operation centred all tracks around zero and scaled amplitude by the standard deviation. The cross-correlation between both sensor signals was estimated over a changing lag time $\Delta F \in [-10, +10]$, and normalized to the value at $\Delta F = 0$. Time lag was the ΔF at which maximum cross correlation between signals was obtained.

2.8.2 Peak identification and thresholding

All high-resolution imaging data was first smoothened by calculating a moving average over a window of ± 3 frames. This operation reduced high frequency noise from jitters in the Z-plane between successive frames. Peaks were identified using the `findpeaks()` function in MATLAB, with a minimum allowed distance of 2 frames between successive peaks. For every peak, the peak prominence and the local

variance in a window of ± 5 frames was recorded, and thresholding was performed on these two properties. To set thresholds, first the peak prominence and local variance of each peak in the dataset was converted into a z-score as follows:

$$Z = \frac{x - \mu_{neg}}{\sigma_{neg}}$$

Where Z is the Z-score for either peak prominence or local variance, x is the prominence or local variance for a peak, μ_{neg} is the mean of the negative control, and σ_{neg} is the standard deviation of the negative control. Next, a threshold of 1 SD was empirically chosen for both properties. Using this threshold typically resulted in about 2-3% of all peaks in the negative control passing the criteria for acceptance.

For experimental data from section 3.4, three highly correlated peaks were detected in the 0 ng/mL condition in almost all cell tracks at the same experimental times. Visual inspection of movies revealed that these peaks were due to an incorrect Z-position resulting in an out-of-focus image. Thus, peaks occurring within 2 frames of frame number 37, 52, and 81 were removed from the 0 ng/mL condition. As acquisition of different FGF treatments was sequential, no other conditions showed similar microscope errors at the same time.

2.8.3 Feature definitions for time-series analysis

Inter-pulse interval (IPI), the difference between the time points of two successive peaks, was calculated as $T_{i+1} - T_i$, thus the last peak in every track had no associated IPI.

Pulse width was estimated at the closest points of signal crossing at $\frac{1}{2}$(peak prominence) as documented in the `findpeaks()` function.

Pulse frequency was calculated as $\frac{\mathrm{n}_{Peaks}}{\mathrm{hours}}$.

Fraction of 'clustered' pulses was calculated by first finding all peaks in a track that satisfied the condition for 'clustering' defined as:

$$(T_{i+1} - T_i) > T_{thresh}$$

where $T_{thresh} = \mu_{comp2} + \sigma_{comp2}$, from the second component of the GMM fit for the respective dataset, and then dividing by the total number of peaks in that track. As no GMM fit was performed for the S+L+MEKi condition, the value for T_{thresh} used in this instance was derived from the S+L condition in the same experiment. If the location T_n of the last peak in a track satisfied the condition $T_n + T_{thresh} < Track\ length$, then it was counted, otherwise since we cannot know whether there would have been an additional peak within the threshold time, the data point was discarded.

Max windowed pulse rate was calculated as the maximum of pulse frequency calculated over a moving window of 1 hour or 30 minutes as indicated in the text.

2.8.4 Mixture model fits

I used gaussian mixture model (GMM) fits to identify timescales in the distributions of IPIs and the pulse widths. The number of components for a GMM fit can be determined using a scoring criterion. For the IPI and pulse width distributions, I used scores from two separate methods - the Aikake information criteria (AIC) and Bayes' information criteria (BIC) (**Fig 2.8.1**). The optimal number of components chosen corresponded to the lowest AIC/BIC scores. While IPI could be fit by both 3 and 4 components, I conservatively chose 3 since increasing the number of components reduces the number of data points explained by each component. For representation, the AIC/BIC plots for the WT in S+L are shown below (data from **Fig 3.2.2**), but the same optimal number of components was obtained for all experimental conditions.

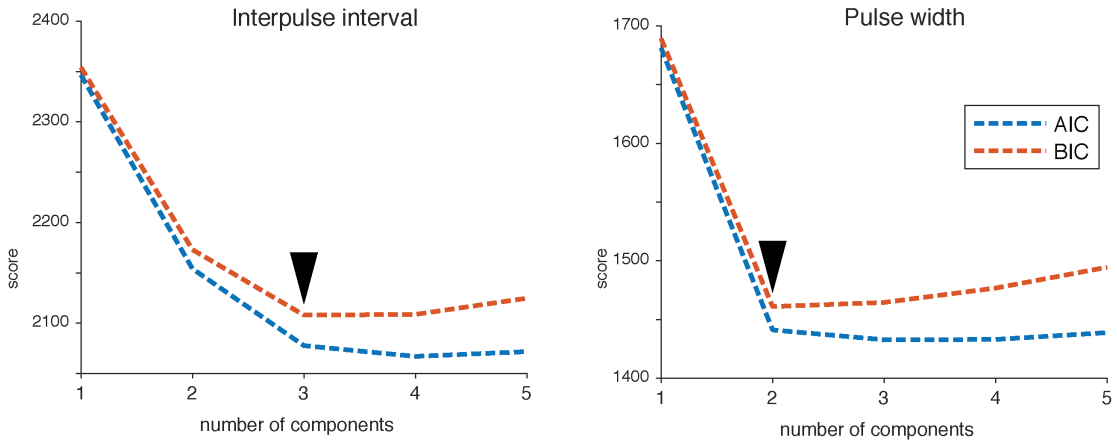

Fig 2.8.1: Optimal number of components for GMM fits

GMM fits were carried out with different numbers of components, and the AIC (blue) and BIC (red) scores for each fit were calculated. Right panel: fit scores for the distribution of interpulse intervals, left panel: fit scores for the distribution of pulse widths.

2.8.5 Hierarchical clustering

Agglomerative hierarchical clustering is a bottom-up approach to clustering. At each step, two clusters that are similar are grouped together until only one cluster remains. I first accumulated all peak shapes by tabulating time series data ± 3 min from a peak. Using Euclidean distance as the similarity metric, and Ward's method to calculate linkage distances, I used the MATLAB function `cluster()` to perform the clustering. Dendrograms were drawn using the MATLAB function `dendrogram()`, where the height corresponds to the cophenetic distance describing the dissimilarity between a pair of clusters. Data can be partitioned by specifying a number of desired clusters or by specifying a height at which to trim branches in the dendrogram. As the purpose of the clustering was to explore the data rather than rigorously determine the number of classes, I empirically set 6 clusters as the partition value. Choosing a larger number of clusters yielded a cluster with only 1-2 peaks in it, indicating a lack of generalizability, and choosing a lower number of clusters did not allow identification of the asymmetric peak classes.

3 Results

3.1 ERK activity is dynamic in mouse embryonic stem cells

FGF/ERK signalling is crucial for differentiation across many stages of mouse development, and has also been shown to have an instructive role in fate determination (Reviewed in Böttcher & Niehrs, 2005). While the components of the signalling network have been described over the years (Kang et al., 2013; Kunath et al., 2007; Chazaud et al., 2006), the role of intracellular signalling dynamics has not been studied extensively. Mouse embryonic stem cells (mESCs), which can be induced to differentiate in response to paracrine FGF, are a tractable model system, amenable to both genetic manipulation and imaging, to study the intracellular dynamics of ERK activity in response to physiologically relevant FGF signals.

3.1.1 ERK phosphorylation is heterogeneous in mESCs

To study FGF/ERK signalling, it was necessary to first establish the apparent level of signalling activity in pluripotent mouse ES cells. Using ERK phosphorylation as a proxy for signalling activity, I used immunostaining to visualize phospho-ERK (**Fig 3.1.1**). Standard culture conditions for the maintenance of ES cell pluripotency consist of growth in medium with the addition of foetal bovine serum and the critical cytokine LIF (Williams et al., 1988), here abbreviated as S+L. Under these conditions, ES cells showed heterogeneous phospho-ERK levels (**Fig 3.1.1a**). Small nuclear structures were observed after phospho-ERK staining. However, as these structures were also present in the negative control - the MEK-inhibited condition – I interpreted them as being non-specific. While sub-cellular localization of phospho-ERK has been reported

in other cell types (Reviewed in Ebisuya et al., 2005), in ES cells both cytoplasm and nuclear compartments show correlated levels of ERK phosphorylation (**Fig 3.1.1b**). Thus, I used whole-cell mean phospho-ERK levels as a metric to quantify ERK phosphorylation. In the presence of a MEK inhibitor, PD0325901 (abbreviated as PD03), ESCs showed a stark reduction in phospho-ERK staining intensity. Additionally, I noted that even the lowest phospho-ERK expressing cells (**Fig 3.1.1c**) still maintained levels of phospho-ERK greater than the MEKi treated cells. This indicates that although cells in S+L have heterogeneous levels of phospho-ERK, these levels never drop to that of the MEKi-treated cells.

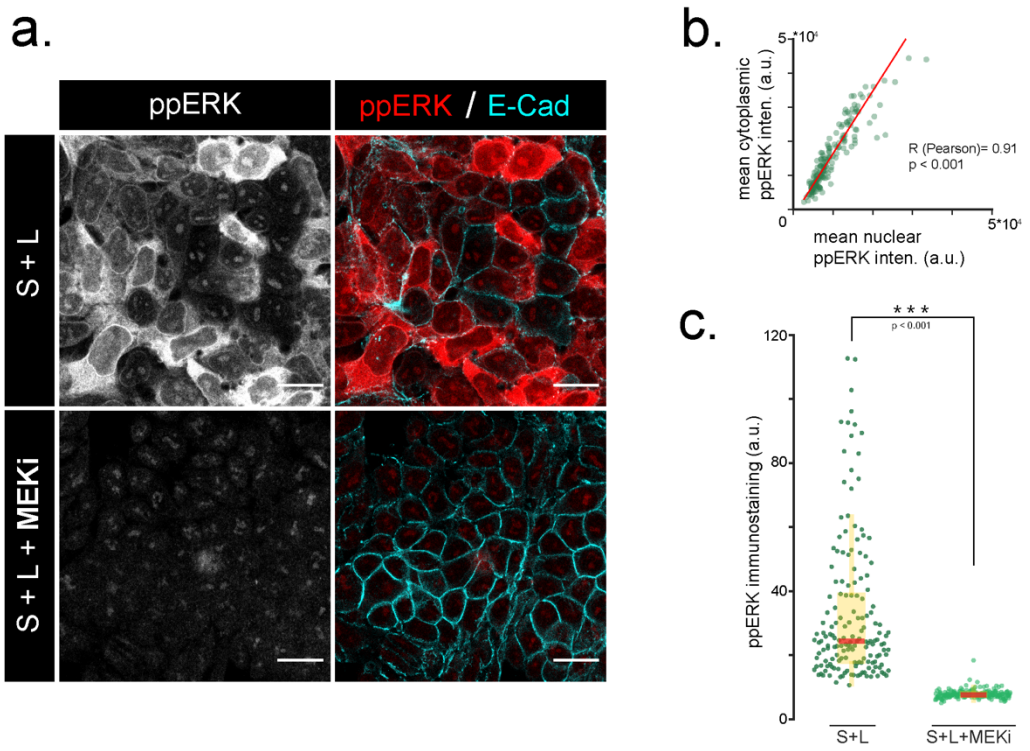

Fig 3.1.1: Heterogeneous ERK phosphorylation in mESCs

a. *Immunostaining for phospho-ERK and cell-membrane marker E-cadherin in S+L and MEKi conditions. Scale bar = 20 um.* ***b.*** *Quantification of phospho-ERK fluorescent staining intensities in the nucleus versus the cytoplasmic compartments of single cells. n = 148 cells. Robust regression line is shown in red.* ***c.*** *Quantification of whole-cell phospho-ERK fluorescent staining intensities in single cells. n>100 cells per condition. Horizontal red bars represent the medians (median S+L=24.39 a.u., median MEKi=7.75 a.u.), box bounds represent the interquartile range (IQR) of the distributions, and the whiskers indicate 1.5 * IQR.*

3.1.2 The ERK-KTR sensor reveals that ERK activity is heterogeneous between cells

The heterogeneity in phospho-ERK could reflect statically-maintained long-term variation in either ERK levels, or in the amount of FGF- or serum-induced signalling activity seen by individual cells. However, these differences could also emerge as a result of taking a snapshot measurement of a dynamic process that is not perfectly synchronous between cells. To differentiate between these two possibilities, I used a translocation-based sensor to measure ERK activity in live cells (Regot et al., 2014). I used a cell line with a stably-integrated single-copy insertion of the ERK-KTR sensor into the Hprt locus to ensure uniformity in expression (Simon et al., 2020). This sensor contains a fluorescent tag, a nuclear export sequence (NES), and an ERK target site that is embedded within a custom-designed nuclear localization sequence (NLS). In the absence of ERK activity, the sensor comes to a dynamic equilibrium between nucleus and cytoplasm through constant nuclear import and export. In the presence of phospho-ERK however, the NLS is phosphorylated, thereby lowering the nuclear import rate and altering the equilibrium point. This results in the sensor remaining strongly excluded from the nucleus (**Fig 3.1.3**).

It has been suggested that expression of ERK substrate sensors could act as a 'sponge' by introducing a large number of binding sites, thereby altering levels of available phospho-ERK and impacting endogenous signalling levels (Kim et al., 2011). Due to the large number of described interactions and feedbacks in the FGF/ERK network, the effect of this disruption is not obvious to predict. However, as ERK signalling controls pluripotency, I next examined expression levels of pluripotency markers NANOG and OCT4 in the ERK-KTR-sensor cell line (hereby referred to as eKTR) to test whether signalling was significantly dysregulated, and found them to be comparable to that of the parental cell line (**Fig 3.1.2**). Additionally, in a different study, these cells also transmitted to the germline of chimeric mice (Simon et al.,

2020). Together, these data indicated that the eKTR line retained expression of pluripotency markers, and a normal developmental potential.

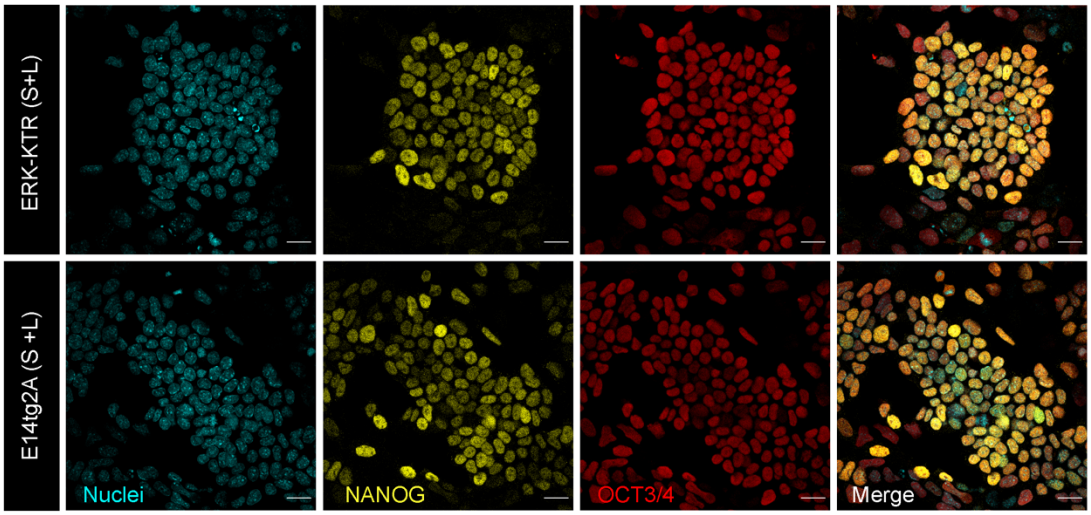

Fig 3.1.2: eKTR cells maintain expression of pluripotency markers

Images showing a single colony of mESCs expressing pluripotency markers NANOG and OCT3/4. Expression levels are comparable with the parental (E14tg2A) cell lines. Scale bar = 20 μm.

Similar to the phospho-ERK immunostaining data, still images of eKTR cells showed heterogeneous levels of ERK sensor localisation, with some cells displaying an equally bright nucleus and cytoplasm, while others showed a dark nucleus and correspondingly brighter cytoplasmic region (**Fig 3.1.3c**). Sensor activity was quantified as previously described (Pokrass et al., 2020) using a ratio of mean cytoplasmic intensity to mean nuclear intensity within a carefully drawn region-of-interest (ROI). Thus, high sensor values correspond to elevated ERK activity. Compared to the 3.1-fold difference in the immunostaining data, the sensor C/N ratios showed only a 1.4-fold increase in median ERK activity between the MEKi control and the S+L ERK active condition, with some overlap between the two distributions (**Fig 3.1.3d**). Additionally, sensor values had a more symmetrical distribution compared to the skewed long-tailed distribution of phospho-ERK staining intensities. These results indicate that while both sensor activity and

phospho-ERK levels decrease upon MEK inhibition and show broad agreement, there is no simple linear relation between the two.

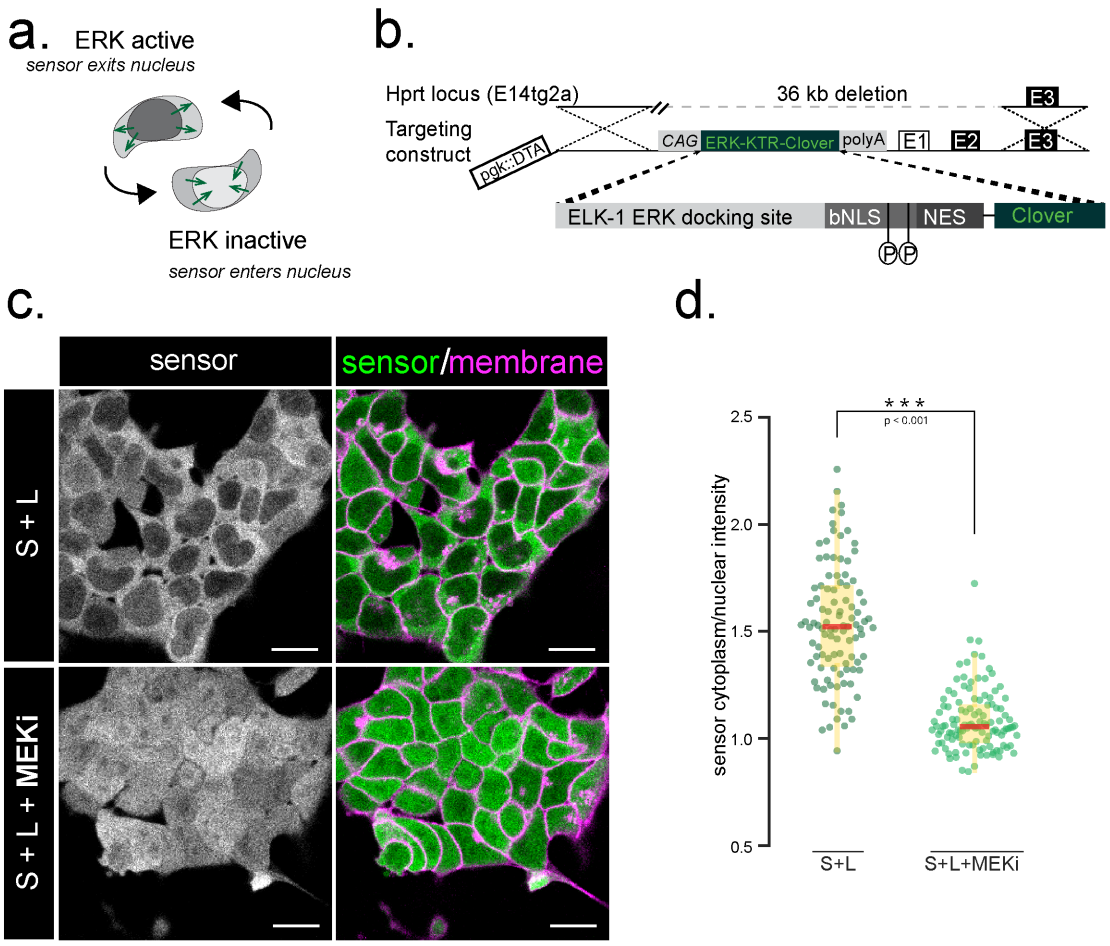

Fig 3.1.3: ERK-KTR sensor reports heterogeneous ERK activity in mESCs

a. *Scheme shows translocation sensor readouts for ERK activation status.* ***b.*** *Targeting strategy for single-copy insertion of the ERK-KTR sensor (*Raina et al., 2020a*).* ***c.*** *Sub-cellular localisation of the ERK-KTR sensor live cells maintained in S+L medium (top), and MEKi-treated (bottom) conditions. Membrane is stained with live-cell membrane marker CellMaskRed. Scale bar = 20 um.* ***d.*** *Quantification of cytoplasmic to nuclear ratio of cells imaged as in a. n>100 cells per condition. Horizontal thick bars indicate medians (median S+L=1.52, median MEKi= 1.05), box bounds represent the interquartile range (IQR) of the distributions, and the whiskers indicate 1.5 * IQR*

3.1.3 Live imaging reveals that ERK activity is dynamic

To study whether ERK activity is dynamic in live cells, I next made 2-hour-long movies of the eKTR cells, imaged with a frame interval of 20 sec. Movies of eKTR cells revealed that ERK activity in S+L pluripotency conditions is highly dynamic (**Fig 3.1.4a**). Sensor activity in single cells was tracked over time by measuring the mean intensity within a nuclear ROI. While quantifying sensor activity in still images depends on relative enrichment of the sensor in the two subcellular compartments, and thus requires measurements of both cytoplasmic and nuclear intensities, by using sequential timeseries measurements I was able to detect changes in ERK activity by measuring just one compartment (**Fig 3.1.4**). Measurement of single cell dynamics revealed a range of dynamic behaviour (**Fig 3.1.4b**). In some cells, fast and regular pulsing was observed (trace #3), others showed pulsing at slower rate (trace#4), and others showed transitions between pulsing and non-pulsing behaviours (trace #6). Out of the 69 cells that were tracked for the S+L condition, not all showed pulsing behaviours – some cells were entirely non-pulsatile, and others only showed low amplitude fluctuations (**Appendix 7.1**). Thus, in standard pluripotency conditions, ERK dynamics are heterogeneous between cells. These dynamics can be effectively suppressed by treatment with the MEK inhibitor, demonstrating that the ERK dynamics reported by the sensor are specific to ERK activation and depend on MEK activity (**Fig 3.1.4b**).

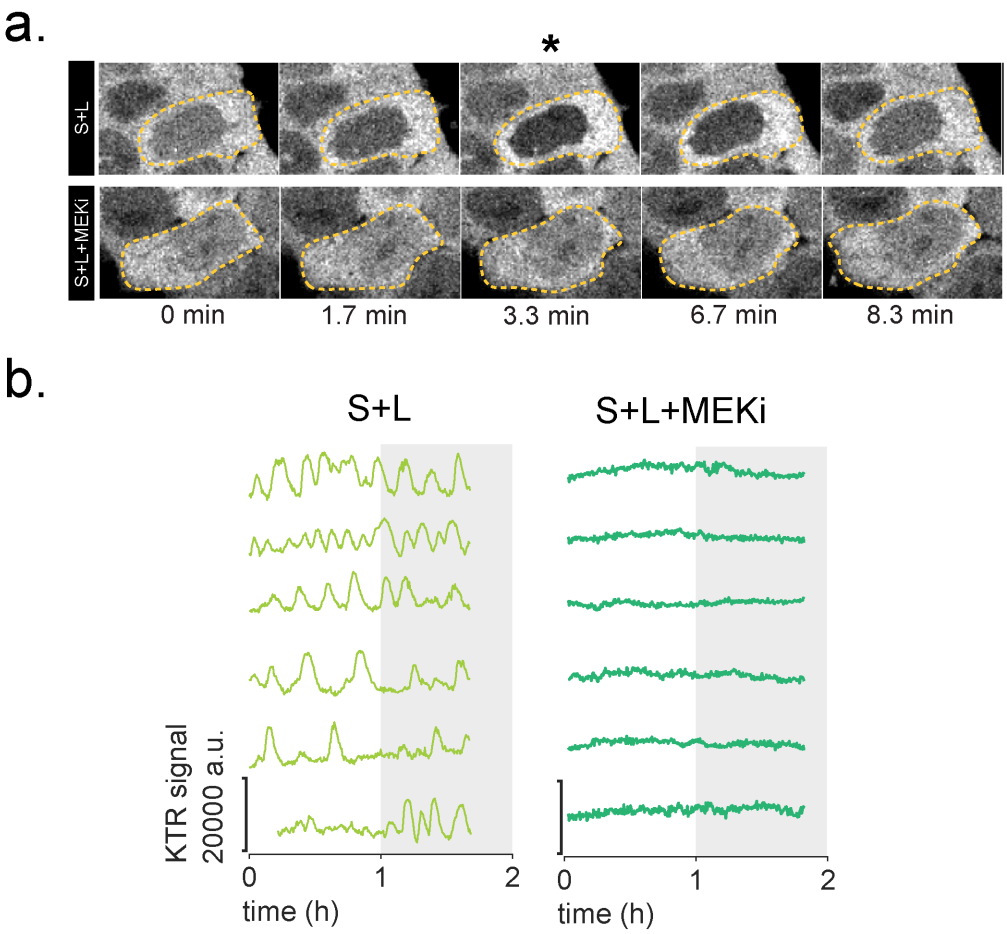

Fig 3.1.4: KTR sensor reveals dynamic ERK activity in mESCs

a. *Live imaging montage of eKTR cells. Dashed yellow line indicates cell outlines. Top row shows a cell in S+L exhibiting a pulse of ERK activity, bottom row shows a cell in MEK-inhibited conditions without any pulsing behaviour.* ***b.*** *Mean nuclear intensity traces for six cells in S+L (left) or MEKi (right) conditions. A range of dynamic behaviours is visible.*

3.1.4 Two orthogonal sensors show highly correlated dynamics

The process of translocation has an intrinsic limiting timescale that likely depends on cell type. Since the KTR sensor uses changes in sub-cellular localization as a readout, it could potentially act as a low-pass filter to prevent observation of fast dynamics. The sensor activity could also be influenced by periodic import/export processes, thus resulting in spurious ERK activation dynamics. Additionally, dynamics of the sensor may be specific to the ERK-substrate sequence used, and may not reflect a general case for all ERK targets. To verify that the ERK activity pulses I observed were

not particular to the choice of sensor, I made recordings of cells co-expressing an alternative ERK activity sensor, the EKAREV (**Fig 3.1.5a**) (Komatsu et al., 2011).

As the EKAREV sensor is a unimolecular FRET sensor that depends on a change in molecular confirmation to generate a FRET signal and does not depend on changing sub-cellular localization, it does not share the same mechanistic constraints of the translocation-based KTR sensor. Additionally, the EKAREV sensor uses the ERK docking site from a different ERK substrate CDC25. To measure concordance between these sensors, I co-transfected spectrally compatible variants of both the KTR and the EKAREV, and made simultaneous measurements of both, in the same cell (middle and bottom rows, **Fig 3.1.5b**). Single-sensor-only controls also demonstrated dynamic behaviours (top row, **Fig 3.1.5b**). As the amplitudes of both sensor readouts were different, I standardized each timeseries by subtracting the mean and dividing by the standard deviation for each cell. While this stretches amplitudes, it makes correlations easier to visualize. Inspection of these data reveal that both sensors closely track each other in S+L conditions (**Fig 3.1.5c**, upper panel). As the negative control, the MEKi-treated condition shows any spurious correlations between the two signals that could arise from shared technical errors such as changes in the focal plane (**Fig 3.1.5c**, lower panel). The normalised cross-correlation was calculated over a frame lag of ± 10 frame, where the interval between each frame was 40 s (**Fig 3.1.5d**). The maximum cross-correlation over the lag period was recorded per cell, showing a median normalised-cross-correlation value of 0.81 for cells in S+L compared to -0.26 for cells in MEKi (**Fig 3.1.5e**). As there is poor agreement between the sensor dynamics in the MEKi condition, this demonstrates that the correlation we see in the S+L treated cells comes from true dynamics of ERK activity, rather than from systematic errors.

I next wanted to determine whether there was any lag between the sensors. In contrast to a previous report (Sparta et al., 2015), I found minimal time lag between the sensors, with half the cells (n=5) showing maximum cross correlation at zero frame lag, and the other half (n=5) showing max cross correlation with a frame lag of 1 (**Fig**

3.1.5f,). Thus, the sensors track one another within the 40 s time resolution of this experiment, although the KTR sensor can sometimes show a small delay.

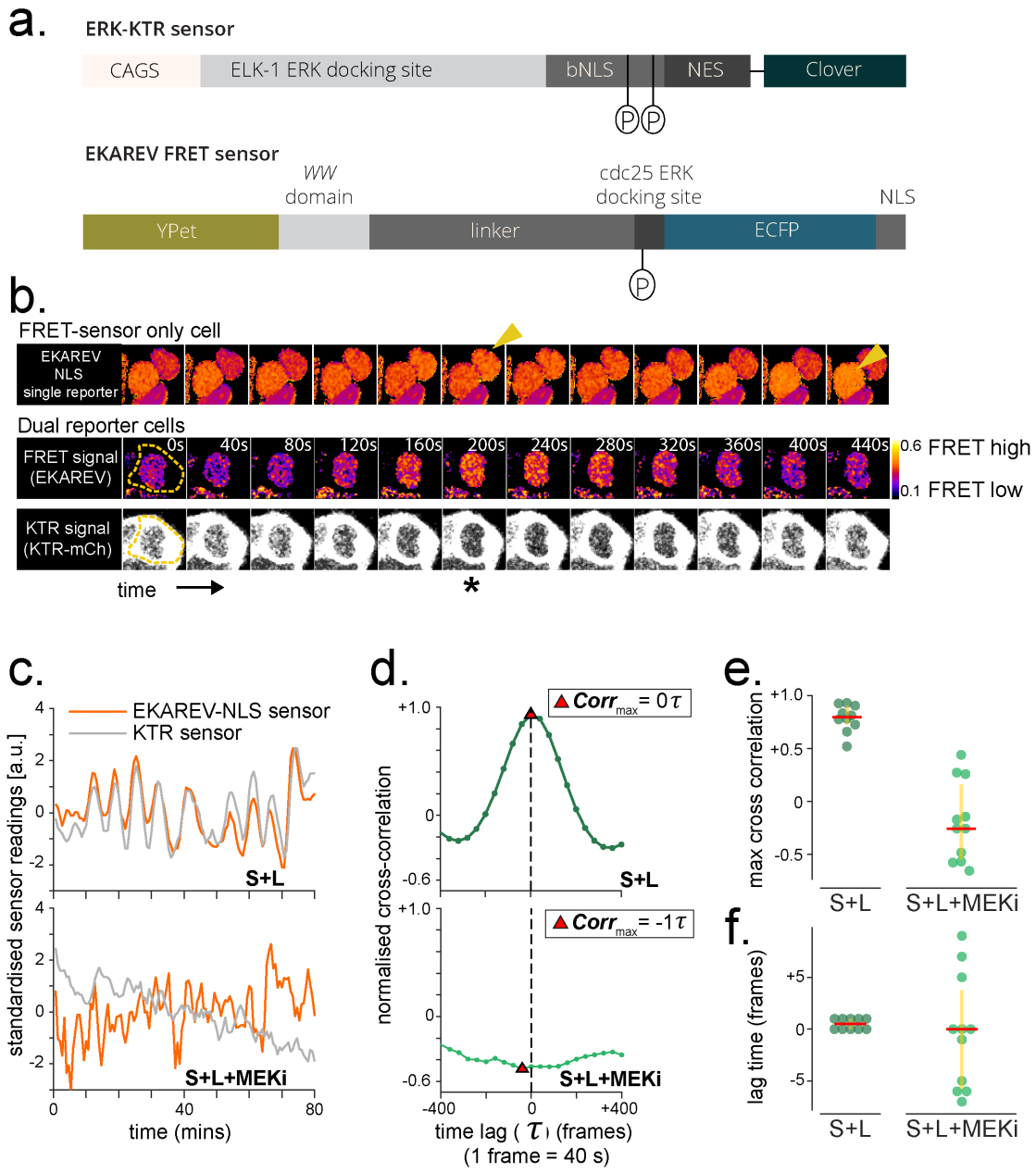

Fig 3.1.5: Orthogonal sensors show correlated dynamics

a. *Schematic of the ERK-KTR sensor compared with the EKAREV-FRET sensor. EKAREV is a unimolecular FRET sensor that uses an alternative ERK binding site, and alternative ERK target sequence.* ***b.*** *Live imaging montage. Top row: nuclei of cells expressing only the EKAREV-FRET sensor. An ERK 'peak' is annotated with a yellow arrowhead. Middle and bottom rows: a single cell expressing both the ERK-KTR-mCherry and the EKAREV-CFP-YFP FRET reporter. Middle row shows ratiometric images of the nuclear-localized EKAREV sensor, bottom row shows images of the same cell expressing the KTR-mCherry sensor. High ERK activity detected by the FRET reporter coincides with strong nuclear exclusion of the KTR reporter (asterisk). Gamma values for the KTR montage have been adjusted to*

0.86, and the image has been smoothened for the purpose of visualization only. The acquisition rate was 40 s/frame. ***c.*** *Single cell trace of mean nuclear intensity (KTR reporter, grey) and mean FRET ratio (EKAREV reporter, orange) in the same nuclear ROI over time in the absence (top) and the presence of MEKi (bottom). FRET ratio was calculated as the ratio between donor emission and acceptor emission upon donor excitation.* ***d.*** *Normalized cross correlation for data shown in b. between traces of the different sensors as a function of time lag τ.* ***e.*** *Summary statistics of maximum cross correlation over a lag of ± 400 s between both reporters in pluripotency (S+L) and MEKi conditions.* ***f.*** *Lag times at max cross correlation between both sensors. e,f - Yellow vertical line represents the inter-quartile range (IQR), and the horizontal red line indicates the median. Number of cells n=10 cells (S+L) and n=11 cells (S+L+MEKi).*

In conclusion, this evidence indicates that ERK activity is dynamic in pluripotent mESCs, and is heterogeneous between cells as well as within a single cell over time (Appendix 7.1). Further, we've shown that the KTR sensor is fast enough to provide adequate temporal resolution of these dynamics.

3.2 ERK oscillations have a characteristic timescale and are driven by paracrine FGF4

As the cells in S+L showed heterogeneous ERK pulsing dynamics, I next needed a method to quantify the timeseries and characterise both the heterogeneity as well as the timescales present in the data. Since the pulses of ERK activity were a prominent feature of the dynamics (**Fig 3.1.4**), I developed a method to annotate the local maxima of single pulses as 'peaks', and then calculate properties of the timeseries dependent on this peak identification.

3.2.1 Establishing a method to quantify ERK dynamics

Previous approaches to annotate similar timeseries data typically start by annotating peaks, and then dependent features such as the peak height or 'prominence', the peak width, and the inter-pulse interval (IPI) can be measured (Goglia et al., 2020; Simon et al., 2020; Hiratsuka et al., 2015). To study the distributions and changes in the timescales of ERK pulsing dynamics, I sought to first identify ERK pulses.

As the signal of the ERK sensor was noisy, identification of ERK pulses was split into two steps. In the first step, I wanted to eliminate the high frequency noise component that was generated by slight differences in the focal plane between successive frames, clearly visible in traces of the MEKi-treated cells (**Fig 3.1.4b**). This minor jitter in intensity was suppressed by smoothing the timeseries with a sliding window of 3 frames, creating a low-pass filter that preserved dynamics slower than 1 minute. In the previously shown timeseries (**Fig 3.1.4**), most pulses appeared to be about 5-15 minutes long, thus this lower limit to the rate of the ERK dynamics was well below the observed pulsing rate and was unlikely to introduce any clipping of the signal.

In the second step, I needed to correctly detect peaks of ERK activity in the S+L traces. All local maxima in all traces were first annotated as 'peaks' (**methods 2.8.2**). Next, I used properties of the local maxima in the MEKi-treated timeseries to set a threshold such that I retained only peaks that corresponded to pulses of ERK activity in the S+L condition (**methods 2.8.2**). A threshold that was not hard-coded, but was instead based on the distribution of the peak properties in the MEKi condition should be less sensitive to day-to-day experimental variations. To build these distributions, for every local maximum I recorded two properties: the prominence, and the local variance in the signal across a window of 5 frames (**Fig 3.2.1a**). The prominence relates to the height of a peak above the local baseline, whereas the local variance relates to both the height and the width of the pulse. Using these properties, I was able to identify different types of peaks (**Fig 3.2.1b**). To compare peaks in the MEKi-treated negative control with the S+L condition, I converted peak properties to a z-score based on the mean and standard deviation of the MEKi-treated negative control. I used an empirically determined threshold of 1σ (**Fig 3.2.1c,d**) to identify meaningful peaks. This threshold allowed identification of a population of well-defined and high amplitude local maxima in the S+L cells that were absent in the MEKi-treated cells (**Fig 3.2.1b,c,d** upper right quadrant).

Since this threshold value was based on the distributions of peak properties rather than being a fixed number, the same threshold value proved reliable for all the timeseries data acquired with comparable sampling intervals in this thesis. This threshold criteria allows approximately 3 percent of all local maxima in the ERK inhibited condition to qualify as peaks (**Fig 3.2.1d**). Visual inspection of the movies indicated that a majority of these peaks were due to the tracking ROI passing over the darker nucleolar structures visible in the nucleus (for example, see **Fig 3.1.4a,** bottom row) rather than actual nuclear exclusion of the sensor, thus the peak detection algorithm has a false positive rate of about 3 percent. A more stringent thresholding procedure that eliminated all false positives was possible, however this

failed to call many visually clear pulses of ERK activity in the S+L condition. The ERK inhibited condition is meant to provide a baseline of noise emerging from a combination of several sources of error: cell movement, cell shape changes, tracking noise, and intensity fluctuations caused by the instrumentation. As meaningful ERK pulses (confirmed by visual inspection of movies of the single cells) can be observed in the ERK active condition below the threshold values determined by the ERK inhibited condition (for example see **Fig 3.2.1e**, trace#6 hollow grey inverted triangles), it is likely that the contributions of these different sources of noise are not uniform between the two treatments. Thus, the estimated false positive rate determined for the ERK-inhibited condition may be an overestimate of the false positive rate in the ERK-active condition.

Six examples timeseries are shown in **Fig 3.2.1e,f** demonstrating the identification of peaks (red inverted triangles) in both the ERK-active (S+L), and the ERK-inhibited (S+L+MEKi) conditions. I observed a range of dynamic behaviours in the ERK active condition (**Fig 3.2.1e**). These behaviours included sequences with different characteristic timescales (for example, compare trace 3 and trace 4), sequences of high regularity (trace 2), as well as transitions between two types of dynamics (trace 6). Additionally, as noted previously, less pulsatile behaviours were also observed (**Appendix 7.1, 7.2**)

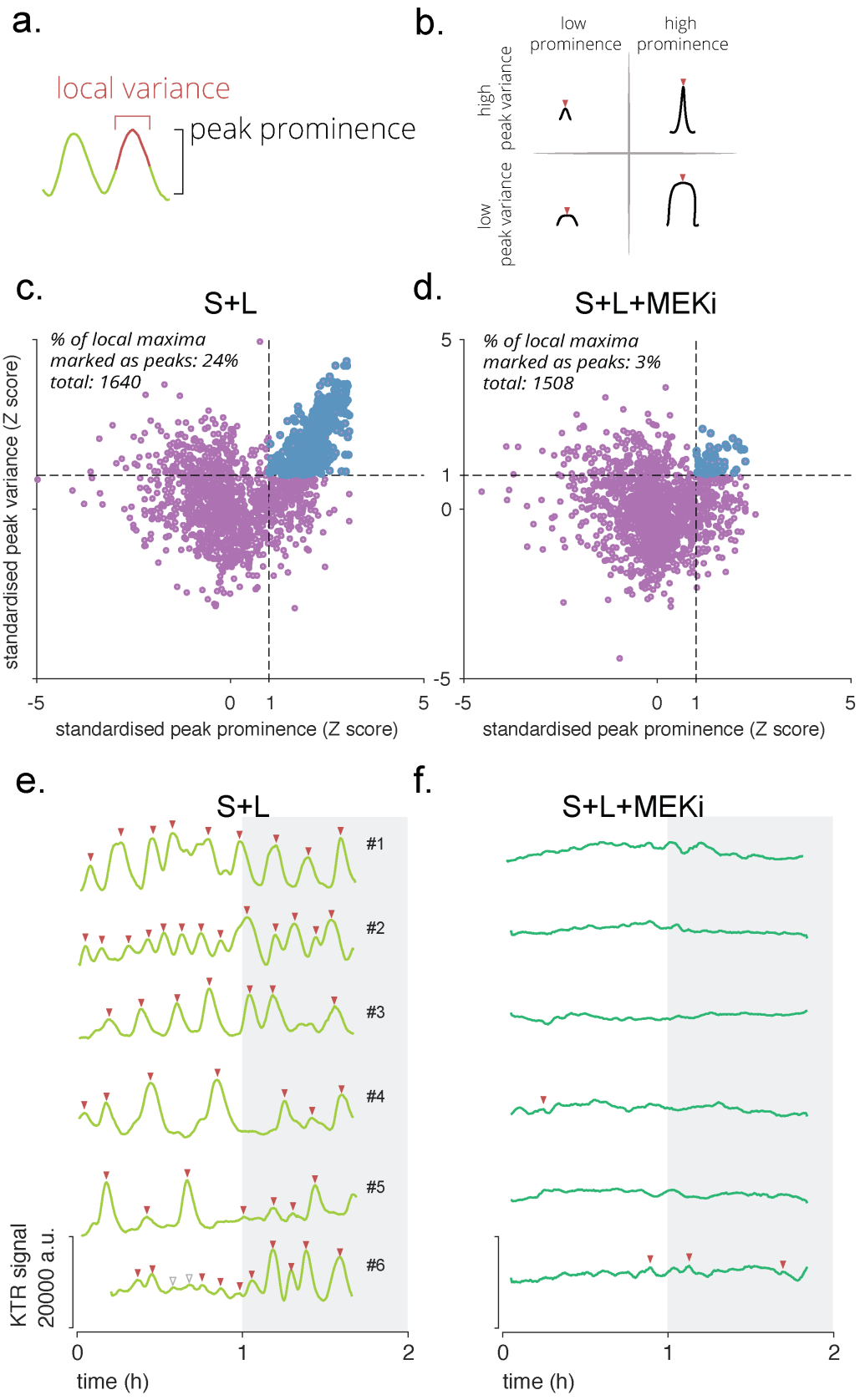

Fig 3.2.1: Pulse detection for cells in serum-containing medium

a. *Quantified properties of peaks. The local variance is calculated over a window of 5 frames from a peak. The peak prominence is the estimated height of the peak from the local baseline).* ***b.*** *Cartoon showing the different types of peaks called based on peak prominence and local variance values.* ***c, d.***

Threshold criteria for local maxima to be considered 'peaks', for cells maintained in serum-containing conditions. Black dashed lines indicate the Z-score values of 1 on both peak prominence and local variance axes. Blue dots are local maxima that were annotated as peaks, while purple dots are local maxima that cannot be distinguished from the negative control, and are rejected as peaks. ***c.*** *S+L and* ***d.*** *S+L+MEKi.* ***e, f.*** *Peak finding on the six example timeseries shown in Fig 3.1.4, for cells maintained in* ***e.*** *S+L and* ***f.*** *S+L+MEKi. Inverted red triangles represent peaks that pass the thresholding criterion. Inverted grey hollow triangles in trace#6 are selected peaks that do not pass the thresholding criterion but can be visually identified as peaks in the movies.*

3.2.2 In S+L conditions, ERK pulses have a characteristic duration and inter-pulse interval

To characterise the ERK activity pulses, I first accumulated data from all single cell timeseries to study population-level properties in the dynamics.

Inter-pulse interval (IPI) was calculated per track (**methods, 2.8.2**), and the resultant data was binned with fixed-width bins to the nearest integer minute. Distribution of IPIs in the S+L condition showed a prominent single mode at 7 min (**Fig 3.2.2a**, black inverted triangle), along with a long tail of IPIs with increased frequencies of occurrence at approximately 12 min (**Fig 3.2.2a**, hollow inverted triangle) and 17 min, suggesting that this histogram was composed of a mixture of multiple overlapping distributions (**Fig 3.2.2a**). To describe these multiple timescales, I used a Gaussian mixture model (GMM) fit (**methods 2.8.4**). The optimal number of components that described the data was determined by using the adjusted information criteria (AIC) and Bayes' information criteria (BIC) scores. Based on these values, either 3 or 4 components could be used. Increasing the number of components in a GMM fit will improve the fit, but the fraction of data explained by each component will reduce, so I conservatively chose 3 (**methods 2.8.4**). This minimal number of components explained the fast timescale adequately, identified intermediate timescales by the second component, and with the third component identified outliers resulting from tracks with very few peaks. Thus, I was able to identify at least two rhythms of pulsing behaviour – fast and intermediate - although as can be seen in the figure, additional

rhythms may be present in the data. A majority of the IPIs (43.5%) were represented by the component with a mean of 6.73 min (**Fig 3.2.2a**, red), very close to the mode of the overall histogram (**Fig 3.2.2a**, black inverted triangle). A slightly smaller proportion of pulses (42.8%) were accounted for by the second component of the fit, representing a range of other timescales with a mean at approximately twice this value at 12.86 min (**Fig 3.2.2a**, yellow), suggestive of either 'skipped' pulses or pulses of a slower rhythm (**Fig 3.2.2c**, trace 4 and trace 5).

Similar to the IPIs, pulse durations were calculated for all pulses and the resultant data was binned into fixed-width bins to the nearest integer minute. However, unlike the distribution of the IPIs, the distribution of the pulse durations had a clear well-defined mode and a more symmetric distribution. I interpreted the long tail with very low frequencies to represent outliers caused by occasional failures of the pulse width estimation algorithm. Therefore, I used a 2-component GMM fit to separate these outliers and determine the mean pulse width (**methods 2.8.4**). The mean pulse width estimated from this fit was 3.51 min (**Fig 3.2.2b**, red). The second component of the fit primarily detected outliers and accounted for 11.9% of the data (**Fig 3.2.2b**, grey) (table), and hence was not shown in the figure. As the pulse duration is determined at 0.5 * (peak prominence), the values calculated here underestimate the true pulse duration, although they are useful for relative comparison between experimental conditions. Using an alternate pulse identification strategy on this same data (Raina et al., 2020a) showed a pulse width of 6.33 mins. In this alternate pulse identification strategy, pulse width is measured at the base of a pulse, in contrast to the 'pulse width' estimated here, which is measured at half the pulse height. Comparing the two values demonstrates that the estimate of pulse duration in this study is about 55% smaller than the values measured at the base of a pulse.

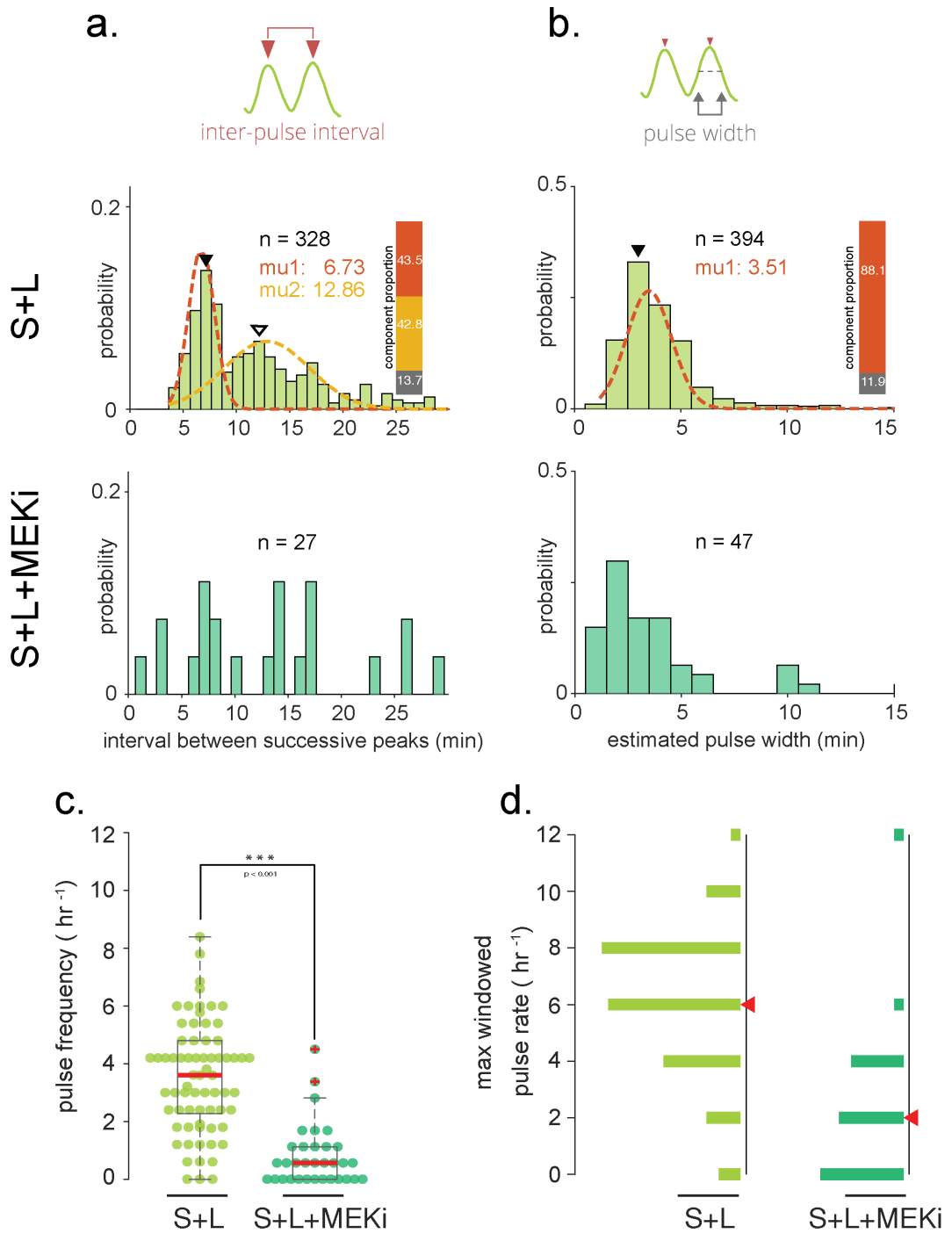

Fig 3.2.2: Properties of ERK pulse dynamics in serum-containing medium

a. *Distribution of interpulse intervals for cells maintained in S+L (top row) and S+L+MEKi (bottom row). Solid inverted triangle corresponds to the value of 7 min, and hollow inverted triangle corresponds to the value of 12 min referenced in the text.* ***b.*** *Distribution of the estimated pulse width for cells maintained in S+L (top row), and in S+L+MEKi (bottom row).* ***a,b****: The first two components of a GMM fit are shown as red and yellow dashed lines, and their means (mu1 and mu2) are inset in their respective colours and provided in* ***Table T1****. Proportion of data explained by each fit is inset as a stacked bar where colours red, yellow, and gray correspond to fit components 1, 2, and 3. Fits were not carried out for the S+L+MEKi condition due to the paucity of data points. Histograms are binned so each bar*

covers 3 frames and is centred on an integer. 'n' in each panel refers to the number of IPI or pulse duration data points considered. ***c.*** *Frequency of ERK pulses for cells maintained in S+L and S+L+MEKi conditions. Individual data points represent the pulse frequency for a single cell. Horizontal red bars represent the medians (median S+L=3.6 pulses hr^{-1}, median S+L+MEKi=0.57 pulses hr^{-1}), box bounds are the IQR, and the whiskers indicate 1.5*IQR. Red crosses mark outliers* ***d.*** *Maximum windowed pulse frequency per track, calculated over a window of 30 minutes. The horizontal spread of each bar is proportional to the number of data points. Red triangle indicates the median.*

I next estimated the frequency of pulsing of an individual cell by dividing the number of pulses over duration of the track. While the median frequency of pulsing was 3.6 pulses hour^{-1}, there was substantial heterogeneity between cells, with some pulsing up to 8 times per hour (**Fig 3.2.2c**). However, as there was also heterogeneity in pulse dynamics over time, calculating the frequency across an entire cell track underestimates the true rate of ERK pulsing since it assumes a homogenous distribution of pulses. To account for this, I also calculated the frequency of ERK pulses over a sliding window of 30 minutes across each track, and from this then determined the maximum pulse frequency (**methods 2.8.3)**. This quantity, termed the 'Max windowed pulse rate', demonstrated that while only one cell had an overall frequency of 8 pulses hour^{-1}, 21/69 cells showed a maximum windowed pulse frequency of 8 pulses hour^{-1}. Altogether 47/69 cells showed a max windowed pulse rate ≥ 6 pulses hour^{-1}, while only 9/69 cells had an overall pulse rate < 6 pulses hour^{-1}. Thus, individual cells can pulse at high rates, but these pulses tend to be clustered together. Taken together, these results show that ERK pulses have at least two timescales of IPIs, have a characteristic width, and are often distributed as clusters of pulses.

3.2.3 FGF4 is the molecular driver of ERK dynamics

While the S+L condition demonstrates ERK dynamics are present in pluripotency conditions, the presence of serum occludes the chemical source of ERK activation. I next wanted to map the dynamic ERK response to a specific ligand. Previous studies

have shown that paracrine FGF4 is the primary driver of ERK phosphorylation in mESCs (Kunath et al., 2007). To test if paracrine FGF4 is the ligand which is inducing dynamic ERK responses, I used a targeted *Fgf4* loss-of-function mutant to remove the confounding effect of paracrine signalling. When these *Fgf4* mutant cells were maintained in S+L medium, I observed levels of phospho-ERK comparable to the wild type (**Fig 3.2.3**, left). This indicates that some component of the medium, possibly the serum, is able to induce ERK signalling even in the absence of paracrine FGF4. However, in the chemically defined minimal medium N2B27 + CHIRON (N2Ch) (Nett et al., 2018), there is almost no detectable phospho-ERK activity in the *Fgf4* mutant cells (**Fig 3.2.3**, centre), while phospho-ERK remains elevated in the wild type. This demonstrates that paracrine FGF4 is able to maintain ERK signalling even in the absence of serum in the medium. Since FGF4 is the single ligand that drives most of the ERK activity in mouse ESCs under these conditions, I next aimed to characterise FGF-specific ERK activity. Further, as the source of the FGF4 is paracrine, using *Fgf4* wild type cells maintained in N2Ch allowed me study ERK dynamics in response to physiological levels of signalling.

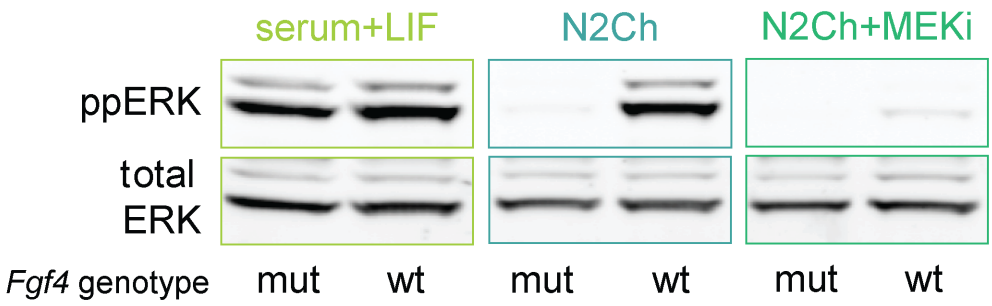

Fig 3.2.3: Paracrine FGF4 is the main driver of ERK activity in mESCs

Western blot for phospho-ERK in eKTR Fgf4 wildtype and eKTR Fgf4 loss-of-function mutant cells maintained in serum-containing (right), and serum-free (centre and left) conditions. All bands are taken from the same blot, although the order of the groups of lanes (S+L, N2Ch, N2Ch+MEKi) has been changed. Contrast settings are preserved across all phospho-ERK staining bands in all conditions, and contrast settings are preserved across all total-ERK staining bands in all conditions.

To study ERK dynamics under conditions of paracrine FGF4 signalling, I acquired time-lapse images of the eKTR cells maintained in N2Ch along with the N2Ch+MEKi condition as an ERK-inhibited control. Due to the heterogeneity I observed in the previous experiment, and to enable a more robust measurement of the max windowed pulse rate, I set up a more extended imaging experiment where I captured multiple fields at a 20 s frame interval for 5 hours. Data were smoothened and local maxima were detected as previously described. Running the same thresholding criteria (**methods 2.8.2**) on the local maxima detected in the N2Ch and N2Ch+MEKi conditions resulted in a similar false positive rate of ~3% in the negative control (**Fig 3.2.4a,b**), demonstrating the robustness of this approach.

Six example traces along with peak annotations for cells maintained in paracrine-competent N2Ch medium and ERK inhibited N2Ch+MEKi medium are shown in **Fig 3.2.4c,d**. These traces were picked to highlight the heterogeneity of dynamics, and so focus mainly on those cells with multiple pulses. A range of dynamic behaviours can be noted, ranging from rapid and regular pulsing (**Fig 3.2.4c**, trace 1), to switches in dynamic behaviour (**Fig 3.2.4c**, trace 3,4,6), and regular pulsing with a slower frequency (**Fig 3.2.4c**, trace 5). The full collection of tracks, including the less pulsatile cells, is provided in **Appendix 7.3** (N2Ch medium, 50 cells) and **Appendix 7.4** (N2Ch + MEKi, 38 cells).

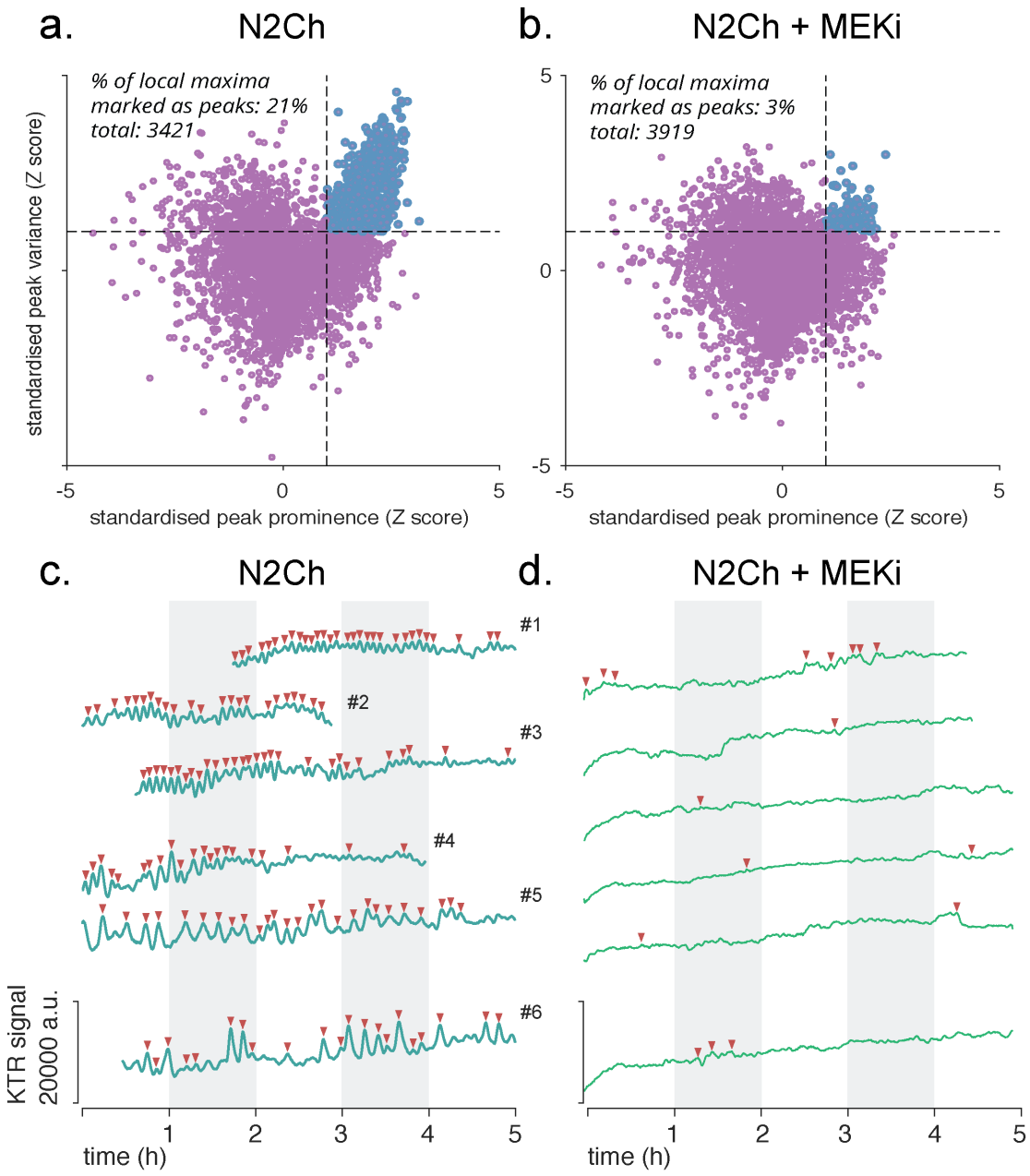

Fig 3.2.4: Pulse detection for cells in paracrine signalling conditions

a.,b. *Threshold criteria for local maxima to be considered 'peaks'. Black dashed lines indicate the Z-score values of 1 on both peak prominence and local variance axes. Blue dots are local maxima that were annotated as peaks, while purple dots are local maxima that cannot be distinguished from the negative control, and are rejected as peaks. a. N2Ch-conditions and b. N2Ch+MEKi conditions.*

c.,d. *Peak finding on six example timeseries for cells maintained in a. N2Ch and b. N2Ch+MEKi. Inverted red triangles represent peaks that pass the thresholding criteria.*

The distribution of the IPIs under paracrine FGF4 signalling conditions was similar to the IPI distribution in serum-containing conditions, demonstrating a prominent modal value at 5 min (**Fig 3.2.5a**, solid inverted black triangle), along with a long tail of IPIs with increased frequencies at 12 min (**Fig 3.2.5a**, hollow inverted black triangle), and 17 min. Since this suggests a mixture of multiple distributions, I followed the same procedure as previously described, and used a 3-component GMM fit to determine the mean values of the different timescales of the IPIs. A majority of the IPIs (57%) were represented by the fast component with a mean IPI of 5.59 min, 17% faster than that measured in the S+L condition. A second component describing the intermediate timescales represented most of the remaining IPIs (32%) with a mean of 12.86 min, consistent with slower rhythms observed in some single cell traces (**Fig 3.2.5c**, trace 5). The third component identified outliers resulting from tracks with very few peaks (11%).

The distribution of pulse durations showed a strong peak between 2-3 mins along with a long tail with low frequencies. I interpreted these values in the tail as representing outliers caused by failure of the algorithm for estimating the pulse duration. This can also be substantiated by observing all single cell traces, which don't show any visually identifiable pulses with a width of 10 min or greater (**Appendix 7.3**) As described previously, I used a 2-component GMM fit to separate the outliers (12.4% **Fig 3.2.5.b**, grey), and determine the mean pulse duration (**methods 2.8.3**) (**Fig 3.2.5**, red). The mean pulse duration estimated from this fit was 2.77 min, 33% shorter than the estimated pulse duration for the S+L condition. Bearing in mind that the pulse duration in this study is measured at ½ the peak prominence instead of the base of the peak, this value of pulse duration is an underestimate of the true duration. In the previous section, I showed that the values for pulse width measured at ½ height were approximately 55% of the pulse width values measured at the base of a peak. Assuming the shapes of the pulses do not vary substantially between experiments, the true pulse width can be thought of as approximately 2.77/0.55 =~ 5 mins. These

values are summarised in **Table T 1** and **Table T 2** for comparison between different experiments described in this thesis.

Despite the faster IPIs and pulse durations, upon calculating the overall pulse frequency I obtained a median value of 3.6 pulses hour^{-1}, identical to the S+L condition (**Fig 3.2.5c)**. Here too, only a few cells showed pulse frequencies of ≥ 8 pulses hour^{-1} (5/50). However, calculations of the max windowed pulse rate showed 23/50 cells with frequencies ≥ 8 pulses hour^{-1} (**Fig 3.2.5d**). Upon calculating the max windowed pulse rate, cells were mainly concentrated into two timescales: the first with rapid frequencies between 7-10 pulses hour^{-1} (20/50), and the second with slow frequencies of between 0-4 pulses hour^{-1} (19/50).

Thus, these results demonstrate that FGF-driven ERK dynamics show broad consistency with the dynamics I observe in S+L. ERK pulses have at least two timescales of IPIs, have a characteristic duration, and show clustering in time. However, in serum-free conditions paracrine FGF4-driven ERK dynamics are faster than in S+L across all measured metrics. These differences could result from some additional signalling ligand(s) from the serum present in the S+L condition that could modulate ERK signalling. Alternatively, since *Fgf4* wild type cells maintain phospho-ERK levels even in the absence of serum (**Fig 3.2.3**), these different dynamics could result from a compensatory upregulation of FGF4 production in the absence of serum.

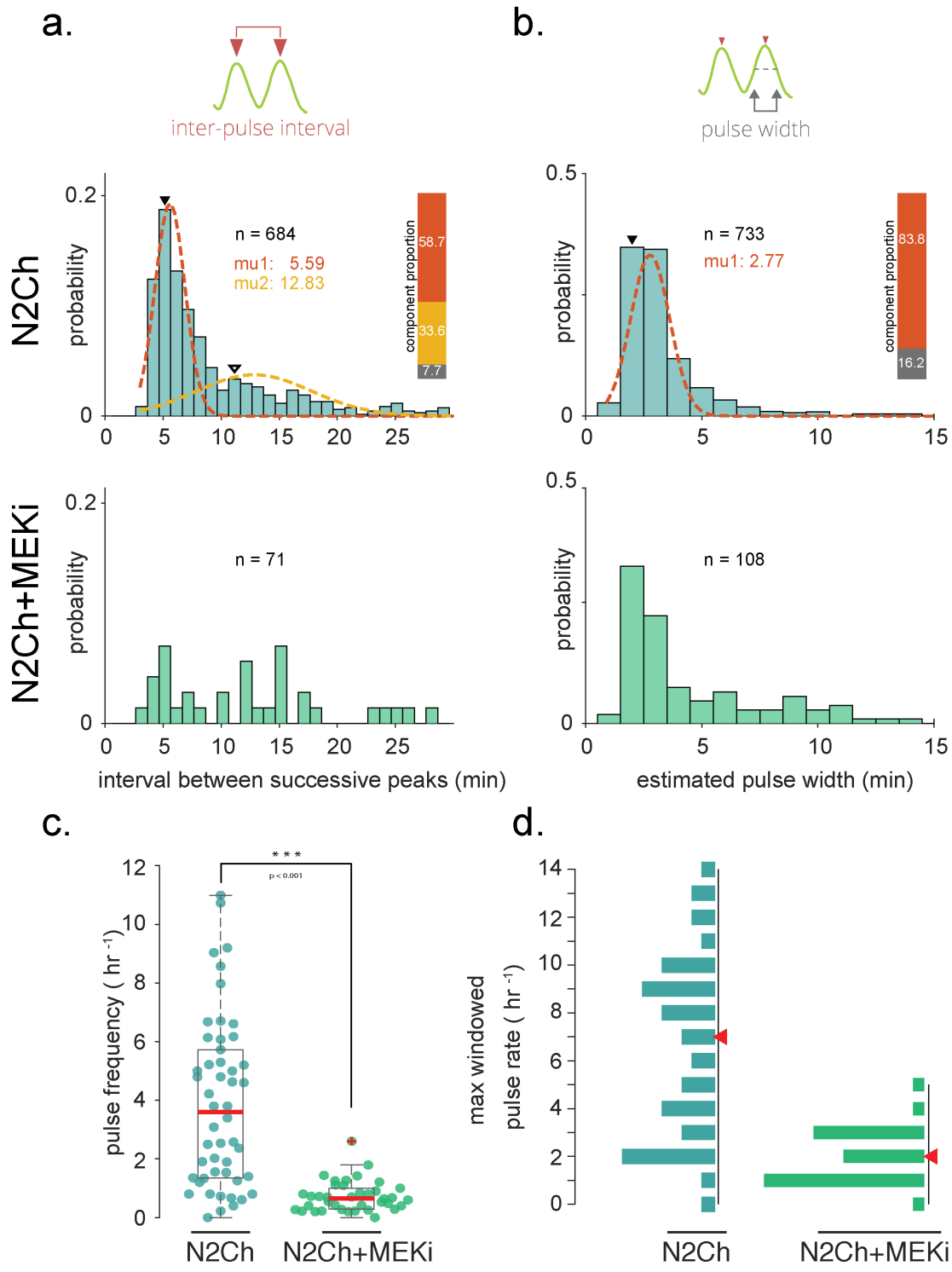

Fig 3.2.5: Properties of ERK pulse dynamics in paracrine signalling conditions

a. *Distribution of interpulse intervals for cells maintained in N2Ch (top row), and N2Ch+MEKi (bottom row). The first two components of the GMM fit are shown as red and yellow dashed lines, and their means are inset in their respective colours. Proportion of data accounted for by each component shown as a vertical stacked bar and also provided in* ***Table T1***. *Solid black inverted triangle represents the mode of the distribution.* ***b***. *Distribution of the estimated pulse width for cells maintained in N2Ch (top row), and in N2Ch+MEKi (bottom row). The first component of the GMM fit is shown as a red*

dashed line, and the mean of the fit is inset in red. Proportion of data accounted for by each component shown as a vertical stacked bar. Fits were not carried out for the N2Ch+MEKi condition due to the paucity of data points. Histograms are binned so each bar covers 3 frames and is centred on an integer. 'n' in each panel refers to the number of IPI or pulse duration data points considered. ***c.*** *Frequency of ERK pulses for cells maintained in N2Ch and N2Ch+MEKi conditions. Individual data points represent the pulse frequency for a single cell. Horizontal red bars represent the medians (median N2Ch=3.6., median N2Ch+MEKi=0.66.), box bounds are the IQR, and the whiskers indicate 1.5*IQR. Red crosses mark outliers* ***d.*** *Maximum windowed pulse frequency per track, calculated over a window of 60 minutes. The horizontal spread of each bar is proportional to the number of data points. Red triangle indicates the median. See Table T 1 for all values.*

Since the max windowed pulse rate and the raw data indicated that pulses did not occur with a constant frequency, I next wanted to identify the cells that had consistent pulsing rhythms from those that showed transitions in their pulsing behaviour. To do this, I calculated the standard deviation of the windowed pulse rate for every cell. Cells with a constant rhythm (**Fig 3.2.6a**, trace1, trace2, trace3) had a low standard deviation of the windowed pulse rate, regardless of the actual cadence of the rhythm. Cells that showed abrupt changes in their pulsing rhythms could be easily identified with a high standard deviation of pulse rate (**Fig 3.2.6c**, compare **Fig 3.2.6a**, trace1, trace2, and trace3 with traces 4 and 5). Using an empirically determined threshold of 2.03 (methods)($\mu+1\sigma$), I identified 10/50 cells which showed abrupt switches in their dynamic behaviour. We can thus see a range of dynamic behaviours between cells – while some show very similar characteristics to non-pulsing cells of the N2Ch+MEKi condition (**Fig 3.2.6b**), others show dynamics ranging from sustained pulsing at different frequencies, to transitions between fast and slow pulsing.

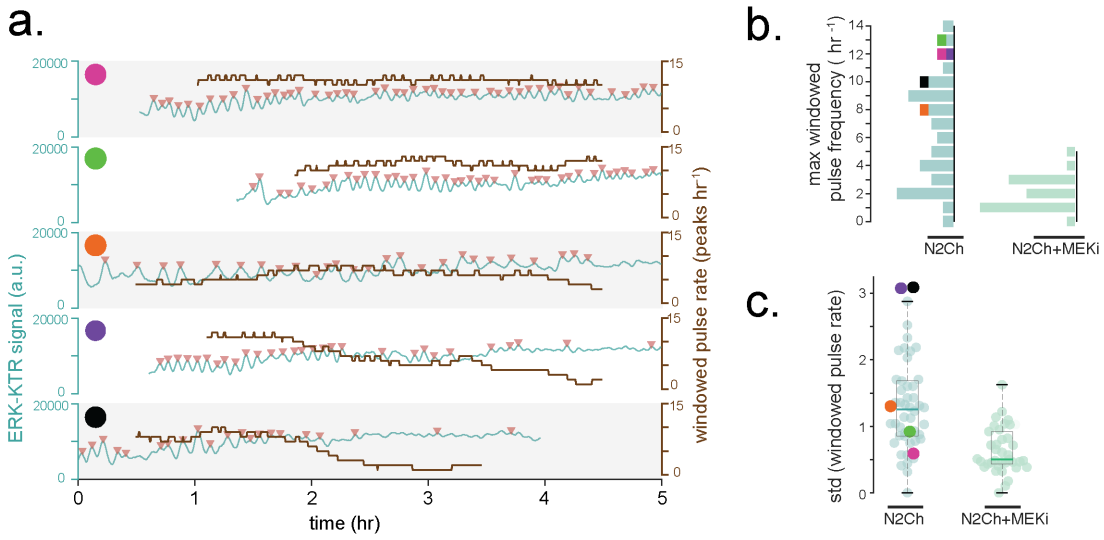

Fig 3.2.6: Transitions between regimes of ERK pulsing dynamics

a. *Six example timeseries traces for ES cells maintained in N2Ch conditions. Cyan trace (left axis) represents KTR signal and inverted red triangles are identified peaks. Brown trace (right axis) is the pulse rate calculated over a moving window of 180 frames (1 hr).* ***b.*** *Maximum pulse rate per cell in the specified conditions. Same data as in* ***Fig 3.2.5d****, except the plot is annotated with colours that corresponding to traces shown in a.* ***c.*** *Standard deviation of pulse rate identifies cells which show transitions between pulsing regimes. Colours correspond to traces shown in a., and points in b.*

3.2.4 ERK dynamics are intermittent

In both experimental conditions, I observed that the fast interpulse intervals and the true pulse durations (calculated at the base of a pulse) had very similar values. If IPIs were longer than pulse durations, this would imply the presence of a short non-pulsatile period between the end of one pulse, and the initiation of the next (**Fig 3.2.7a,** first panel). As pulse durations and IPIs had similar values however, this suggested that pulses tended to occur in immediate succession without much of a non-pulsatile region between them (**Fig 3.2.7a**, second or third panel). Since the distribution of IPIs also contained other slower timescales, I next wanted to test whether the longer IPIs, corresponding to slower pulsing rhythms, were associated with longer pulse durations (**Fig 3.2.7a**, third panel). I started by first plotting the duration of each pulse against its following IPI (**Fig 3.2.7b,c**). If IPIs and pulse

durations scaled proportionally, consecutive sequences of pulses with longer durations would also have longer interpulse intervals (**Fig 3.2.7a**, third panel). On the other hand, if IPIs and pulse widths were not correlated, then longer interpulse intervals could either indicate transitions between pulsing regimes or the presence of a non-pulsing region.

In general, the interpulse interval and the pulse width were correlated at short values (IPI < 8 min)(**Fig 3.2.7b,c**, inset). This indicated that the low values of interpulse interval, mostly described by the 'fast' component of the GMM fit for each treatment, typically identified pulses that were consecutive and occurred immediately one after another (**Fig 3.2.7a**, middle panel). At longer values of IPI (≥ 8 min), pulse duration was independent of IPI choice, demonstrating that pulse duration has an upper limiting timescale (**Fig 3.2.7b,c**).

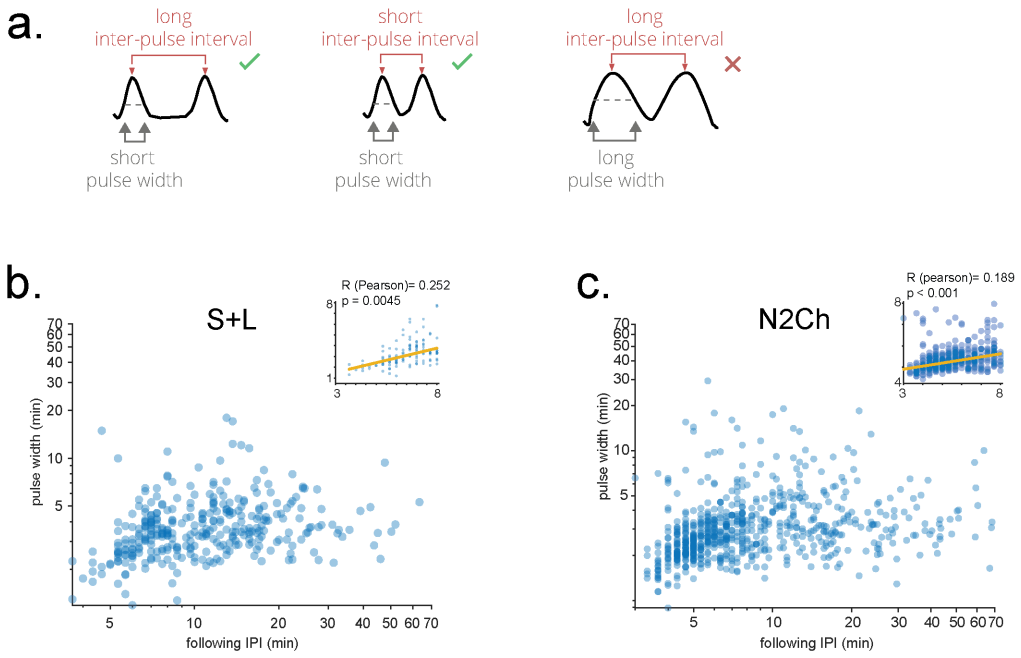

Fig 3.2.7: Pulse durations have a characteristic upper limit

a. Cartoon showing different possible scenarios of pulse width and interpulse interval scaling. ***b.,c.*** *Width of a pulse plotted against the duration of its following interpulse interval for cells in* ***b.*** *serum containing medium and* ***c.*** *serum-free medium. Each data point represents a detected pulse and the IPI following it. The last pulse in every cell track was excluded as no IPI is defined for it.* ***Inset****: A weak positive correlation between IPI and pulse duration can be seen for pulses with low IPIs (<8 min).*

Orange line indicates robust linear regression. Some data points for longer pulse width are off-scale in the inset figure, but the fit (orange line) takes these into account.

Results from the previous section also showed that the max windowed pulse rate has a higher value than the overall pulse frequency in both experimental conditions. Together, both these data indicated that pulses might occur in clusters rather than being spread out homogenously across a track. Pulses within these clusters will typically have a low value of IPI (**Fig 3.2.7a**, second panel). Thus, to examine the fraction of pulses that are part of a cluster, I first needed to set a threshold for the value of IPI that would enable identification of clustered pulses. As I had previously identified at least two timescales of IPIs, I set an interpulse interval threshold as the mean + SD of the second component of the IPI distribution. This separated clusters of pulses that have long interpulse intervals between them, while allowing for both the fast and highly regular pulses, as well as the slower or less regular pulses to qualify as being part of a cluster (**methods 2.8.3**). These clusters can be thought of as sections of rhythmic pulsing where each pulse is quickly followed by a subsequent pulse. The relaxed threshold I used allowed different timescales of pulsing to qualify as being rhythmic. For most cells in ERK-active conditions, greater than 50% of their pulses lay in a cluster, and thus were immediately followed by a subsequent pulse (**Fig 3.2.8**). I observed the median fraction of pulses that are immediately followed by a successive pulse across all cells to be 0.71 in N2Ch and 0.67 in S+L conditions.

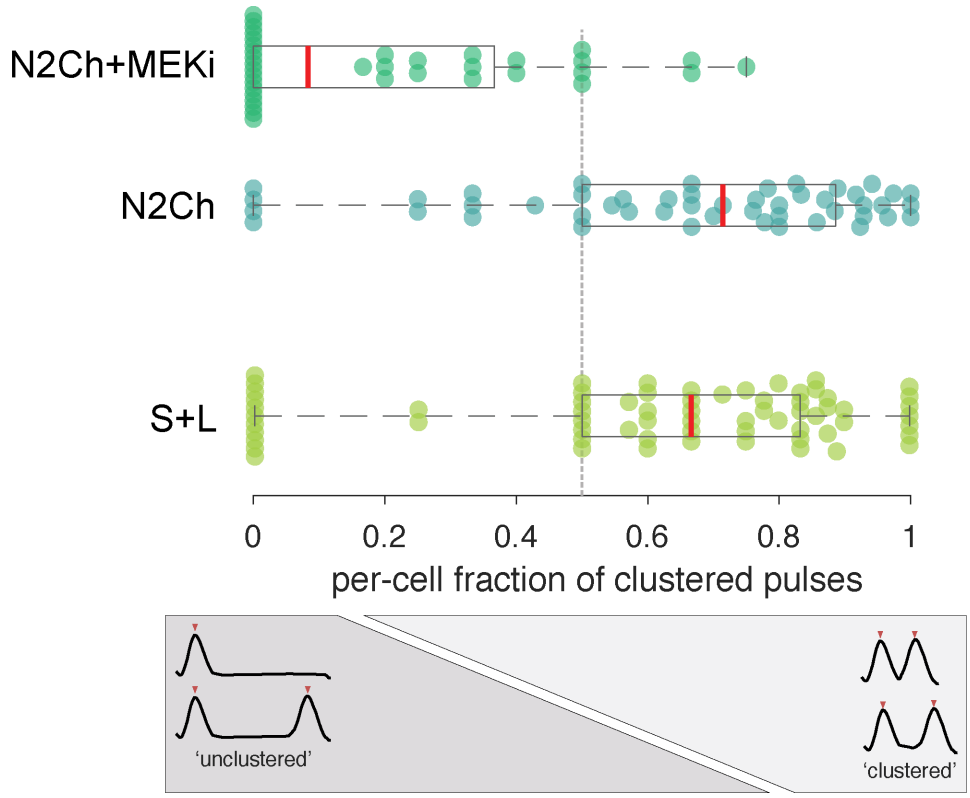

Fig 3.2.8: ERK pulses are clustered in time

*Per-cell fraction of clustered pulses. Each track has to have at least one pulse to be recorded. n=50 cells for N2Ch, n=37 cells for N2Ch+MEKi, and n=66 cells for S+L conditions were recorded. S+L is separated from the other two conditions as it was measured in a different experiment. Red line is the median, box bounds are the inter-quartile range (IQR), and the whiskers indicate 1.5*IQR.*

Thus, I find that rapid ERK pulses are a general feature of ERK signalling in mouse embryonic stem cells as they can be induced to occur in different experimental conditions. These ERK pulses can be induced by physiological levels of FGF4 signalling. Due to their highly conserved pulse durations and their rhythmic nature, ERK dynamics in mESCs can be considered as oscillatory. However, the observations that individual cells can switch pulsing regimes, and that ERK pulses tend to cluster in time, indicate that these oscillations are intermittent.

3.3 Cell cycle differences contribute to heterogeneity in ERK dynamics

In the previous chapter, I showed that some cells transitioned between regimes of ERK pulsing dynamics. What are the sources of this temporal heterogeneity? While cell-intrinsic differences in the protein complement and the initial conditions of the signalling network that give rise to oscillations of ERK activity is one factor, another important difference between the cells is that they are not cell-cycle synchronized. Previous studies have suggested that differences in cell cycle state could affect a cell's perception of growth factor signals (Chaigne et al., 2020; Pauklin & Vallier, 2013).

3.3.1 ERK pulses decay across the cell cycle

To study whether cell-cycle differences contribute to the heterogeneity in ERK dynamics over time, I designed an alternate experimental paradigm to follow cells from birth to division (**Fig 3.3.1**). I used FGF4 wt cells in N2Ch conditions to study paracrine FGF-specific ERK dynamics. As ES cells have a typical cell cycle length of 12-14 h, I imaged a dish of cells for 19 h continuously in order to capture a full cycle from birth to division. To minimize phototoxicity in these extended time-lapse experiments, I reduced the frame rate to 1/105 s. Using the Nyquist rule, this sampling interval allows sufficient resolution to identify dynamics that have a timescale of at least 3.5 min. Visual inspection of the movies also confirmed that pulses were visible by eye. Cells continued to divide even at the end of the movie, although more cell debris was apparent at hour 19 compared to hour 1. Additionally, a reduction in fluorescence intensity was observed over the course of this experiment. This slow reduction in intensity could be due to bleaching, changes in cell culture

medium pH, or fluctuations in lamp intensity and was unavoidable in these extended movies (**Fig 3.3.1b**, compare first panel with last panel).

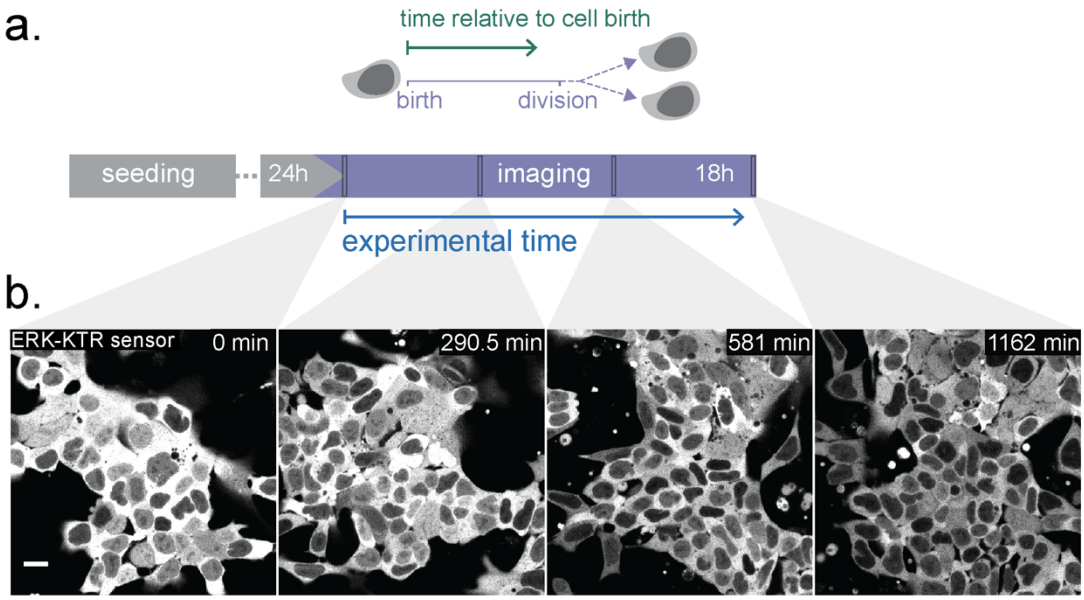

Fig 3.3.1 Extended imaging of eKTR cells

a. *Experimental scheme for long-term time-lapse imaging of ES cells.* ***b.*** *Representative fields of view from four time-points spread out over the time-lapse experiment showing eKTR cells expressing the KTR sensor (white). Scale bar = 20 μm.*

To study the occurrence of ERK pulses in these data, pulses needed to first be identified in cell tracks. As these long-term timeseries have a lower temporal resolution, and require additional detrending to remove the long-term fluctuations in intensity, peak-calling and analysis was performed using an alternate methodology as described in (Raina et al., 2020a). Five example traces, after detrending and peak identification, are shown in **Fig 3.3.2a**. I next used raster plots of the local variance in a sliding window (**Fig 3.3.2b**) to provide an unbiased coarse-grained estimate of ERK pulsatile activity in these timeseries. This plot suggested that there was higher local variance at the start of a cell track, shortly after birth, indicative of higher pulsing activity. Consistent with the plots of local variance, peak calling suggested more pulsing at the beginning of a cell track, and fewer pulses shortly before division (**Fig 3.3.2a,c**).

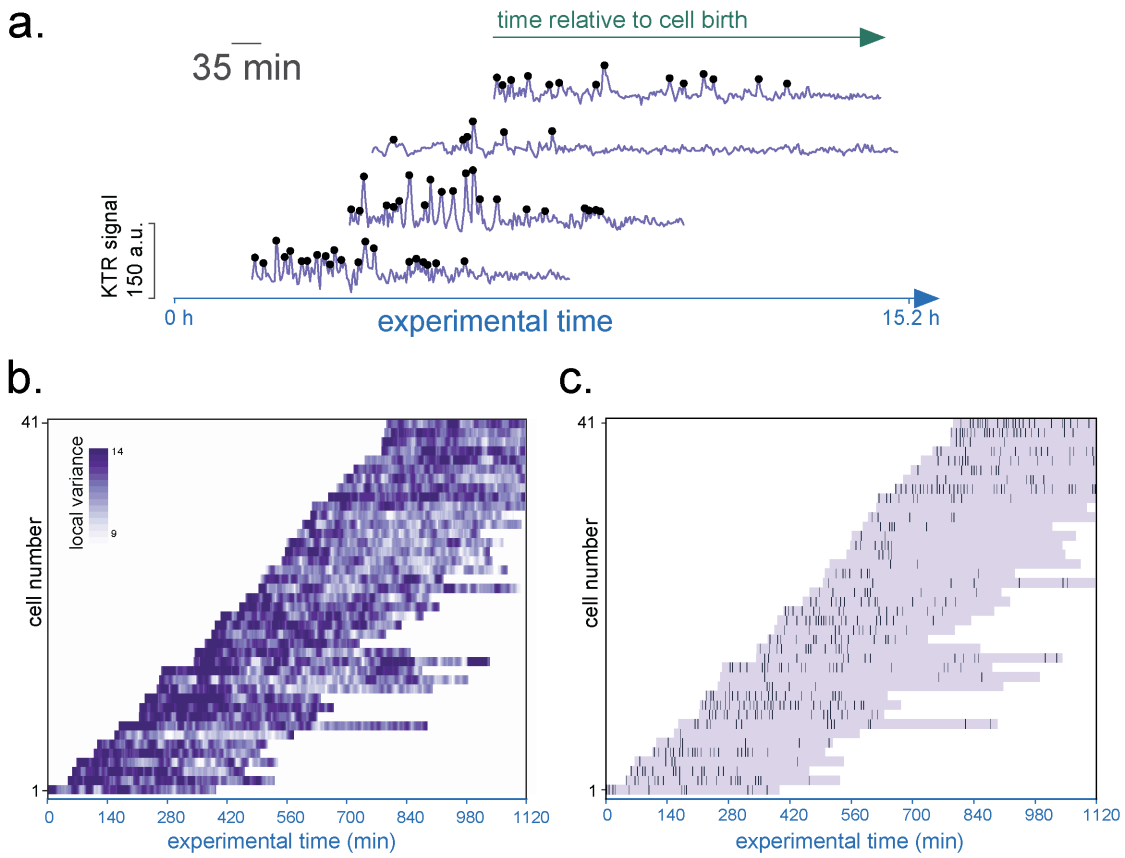

Fig 3.3.2: Aligned traces show higher ERK activity at the start of a cell cycle

a. *Single cell tracks for four FGF4 wt cells in N2Ch medium. Black dots represent peaks. Tracks start at the first frame following division when the cell can be identified, and end upon cell division or the end of the movie. Two time axes are defined: 'time relative to cell birth' and 'experimental time'.* ***b.*** *Local variance within a sliding window of 8.75 min over each timeseries is color-coded (scale inset).* ***c.*** *Identified peaks within the timeseries, marked as vertical black bars. Each horizontal line in b. and c. represents one cell trace, measured from birth to division, except for traces that are bounded by the duration of the experiment.*

Due to the gradual loss of fluorescence intensity described previously, we next needed to determine whether the reduction in pulses over time was due to a cell cycle effect, or was the result of improper peak identification due to non-stationary experimental conditions. To visualize whether the pulse rate changed more over the course of the experiment, or more over the course of a cell's lifetime, the data in **Fig 3.3.2** was binned along two time axes – time relative to the start of the experiment, and the time relative to cell birth. In these 2-dimensional time plots, a decay of pulse

rate from left to right along the 'time relative to cell birth' axis (**Fig 3.3.3a**, top panel) would indicate that pulse rate decays primarily over the course of a cell-cycle. A decay from bottom to top along the 'experimental time' axis however, would demonstrate the contribution of changing experimental conditions on pulse rate (**Fig 3.3.3a**, bottom panel). Timeseries were discretized into 70-min bins along both dimensions for the calculation of pulse rate, and in this plot a general gradient along the 'time relative to cell birth' axis was observed (**Fig 3.3.3b**). To quantify this, pulse rate was calculated over even larger bins of 420 mins (7 h), allowing us to calculate a coarse-grained pulse density map (**Fig 3.3.3c**). This plot revealed that while changing experimental conditions do cause a small reduction in pulse rate, a major contribution to the reduction in pulses comes from a cell-cycle linked effect (**Fig 3.3.3c**, compare gradient along 'experimental time' axis with gradient along 'cell cycle time' axis). The same analysis was also extended to cells maintained in S+L conditions. In this condition, ERK pulsing was stimulated both by paracrine signals and continuous exposure to exogenous growth factors present in the serum. These data further confirmed our results that ERK pulsing is more frequent shortly after cell division (**Fig 3.3.3d,e**).

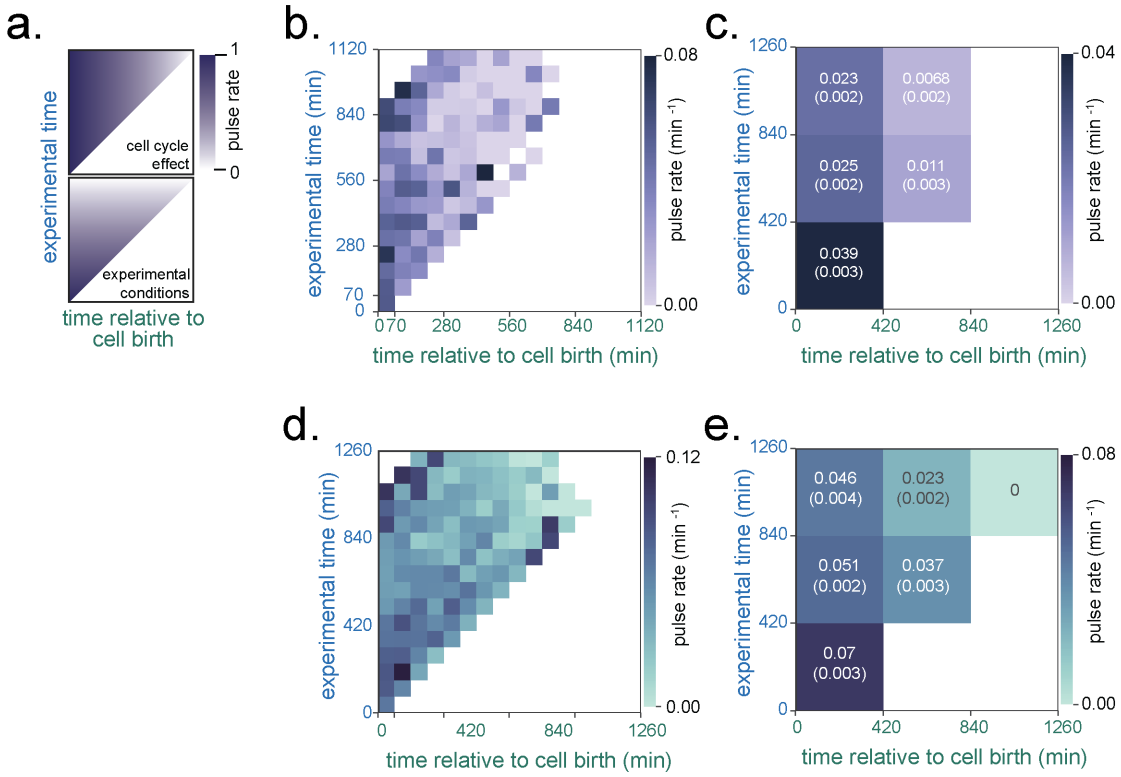

Fig 3.3.3: ERK pulses decay across the cell cycle

a. *Schematic of the expected gradients of binned pulse rate in case the decay of pulses was caused by a cell-cycle effect (upper panel), or by technical limitations that caused changing experimental conditions (lower panel).* ***b.*** *Binned pulse rate along experimental time and time relative to cell birth for cells in N2Ch. Bins are 70 min wide along both axes.* ***c.*** *Further coarse-graining of data in b. into bins of 420 mins along both time axes. Inset numbers are the mean pulse rate in each bin, and number in parenthesis are the standard deviations.* ***d.***, ***e.*** *Same as b,c except for cells maintained in S+L.*

3.4 FGF4 dose controls the extent of oscillatory ERK pulses

In several epithelial cell types, growth factor concentration can change the frequency of ERK pulsing without appearing to alter the duration of a pulse (Albeck et al., 2013; Aoki et al., 2013; Shankaran et al., 2009). However, these cell types depend on growth in serum, which can confound observations of growth-factor-specific ERK activity dynamics. Various sources of paracrine signalling have also been shown to induce ERK dynamics in different tissue contexts such as confluency (Antebi et al., 2017; Aoki et al., 2013), wound-response (Hiratsuka et al., 2015), and development (Pokrass et al., 2020; Simon et al., 2020; Mayr et al., 2018; de la Cova et al., 2017).
In contrast to these studies, previous results (Section 3.2) have shown that FGF4 is the main driver of dynamic ERK activity in mESCs. Additionally, FGF4 both induces differentiation in pluripotent cells (Kunath et al., 2007) as well as quantitatively modulates it (Raina et al., 2020b). Thus, ERK activity in these mouse ES cells is closely linked to a physiological response, and is mainly controlled by a single paracrine ligand, FGF4. To test the dependence of ERK pulsing on FGF4 concentration, I next needed to control FGF4 concentration externally. I used the Fgf4 loss-of-function mutant described previously (3.2.3) where paracrine FGF/ERK signalling is abrogated, and which can be successfully maintained in serum-free medium conditions for limited periods of time. With this cell line, I was next able to ask how titration of a single ligand, FGF4, can modulate ERK pulsing dynamics.

3.4.1 Establishing the dynamic range of FGF4 response

As the Fgf4 loss-of-function mutant cells have very minimal levels of background ERK activity, I first established the dynamic range of cellular response to FGF4 stimulus. Prior to the experiment, these cells are maintained in the serum-free medium N2Ch,

where they experience a chronic deprivation of FGF/ERK signalling. Addition of exogenous FGF4 to these cultures can induce a transient phospho-ERK response, similar to what has been described for a MEKi release (Deathridge et al., 2019). To move beyond this acute response and study steady-state signalling, I first exposed the cells medium containing FGF4 along with the cytokine LIF, added to maintain pluripotency, for 24 h. This enabled cells to adapt to the new signalling regime. As LIF has been previously reported to impinge on ERK signalling (Kunath et al., 2007), I next removed the LIF and replenished the FGF4. Cells were given 4 h to acclimatise to the medium change, before studying cellular response (**Fig 3.4.1a**). A broad range of FGF4 concentrations were titrated into the cell culture medium, and cells were probed for both signalling and transcriptional responses. Signalling was read-out by quantifying the amount of phospho-ERK / total ERK by western blot, and showed a steady increase from 0 – 50 ng/mL, approaching saturation at the higher concentrations (**Fig 3.4.1b,c**). Transcriptional activity was read-out by using an Fgf4 loss-of-function mutant cell line that contained a fluorescent reporter knocked-in to the endogenous locus of one allele of the FGF4 target gene Spry4 (**Fig 3.4.1d,e**) (Morgani et al., 2018). As the transcriptional reporter integrated Venus fluorescence intensity over longer periods of time, the experimental protocol was modified slightly. Briefly, cells were exposed to the indicated concentrations of FGF4 for 24 h and the 'replenish medium' step described in **Fig 3.4.1a** was omitted (**methods 2.5**). Mean fluorescence intensity of the Venus reporter signal, representing integrated FGF signalling over the 24 h of ligand exposure, was detected and quantified. In agreement with western blotting results, I noted that transcriptional response also had a dynamic range between 2.5 ng/mL and 20 ng/mL (**Fig 3.4.1d,e**). Based on these data, I chose a concentration range from 2.5 ng/mL to 20 ng/mL for further experiments. This range lay within the dynamic range of ERK phosphorylation, target gene expression, and differentiation along the primitive endoderm lineage (Raina & Bahadori et al. 2020).

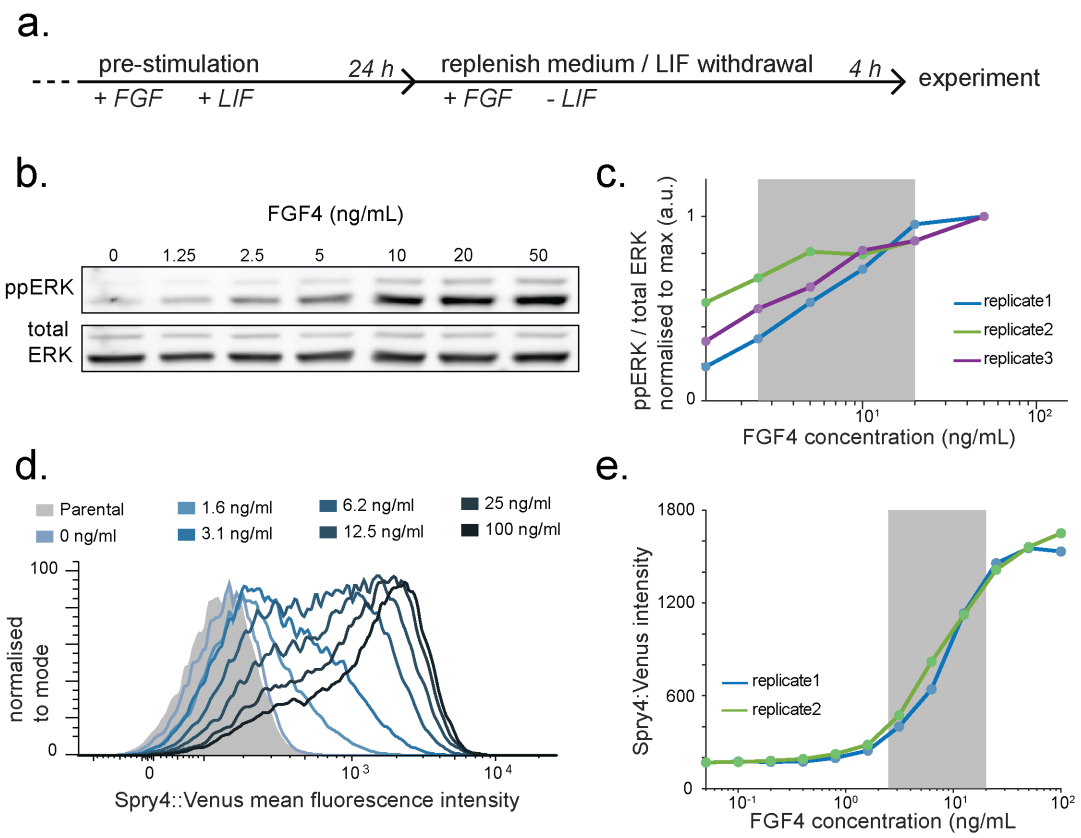

Fig 3.4.1: The dynamic range of FGF4 response

a. *Experimental protocol to study steady-state signalling responses in mESCs.* ***b.*** *Representative western blot for ppERK and total ERK in Fgf4 mutant cells treated with a range of FGF4 concentrations.* ***c.*** *Quantification of western blot data for N=3 experiments.* ***d.*** *Representative flow cytometry of Fgf4 mutant Spry4:H2B-Venus cells stimulated with a range of FGF4 concentrations. Grey-filled curve represents non-fluorescent cells.* ***e.*** *Quantification of Spry4:H2B-Venus mean intensity from FACS, N=2 experiments. Grey box in c. and e. indicates the concentration range [2.5 to 20 ng/mL] used later in this study.*

3.4.2 ERK dynamics have a narrow frequency-response range

To study ERK dynamics upon exogenous FGF4 treatment, I exposed Fgf4 mutant cells to three concentrations of FGF4 according to the experimental scheme shown in **Fig 3.4.1a**, and acquired time-lapse movies with a 20 s frame interval for each condition sequentially. Single cells were tracked as described previously, and I generated traces of ERK reporter activity. Pulse detection and thresholding was carried out as previously described in 3.2.1 and methods. In the absence of FGF4, I observed almost no pulsing, so this condition was used as a suitable negative control

for determining peak acceptance threshold criteria, and set thresholds for peak prominence and peak local variance at 1σ (**Fig 3.4.2a**). As previously, this approach allowed a false positive detection rate of about 3% in the negative control. In the presence of constant external FGF4, widespread pulsing activity was observed across all tested concentrations (**Fig 3.4.2b**). Additionally, I observed substantial variability in ERK dynamics, both within a cell over time, as well as between cells (**Fig 3.4.2b**). This variability in ERK dynamics, even in the presence of constant exogenous FGF, could arise from differences in cell cycle position, as described in Section 3.3.

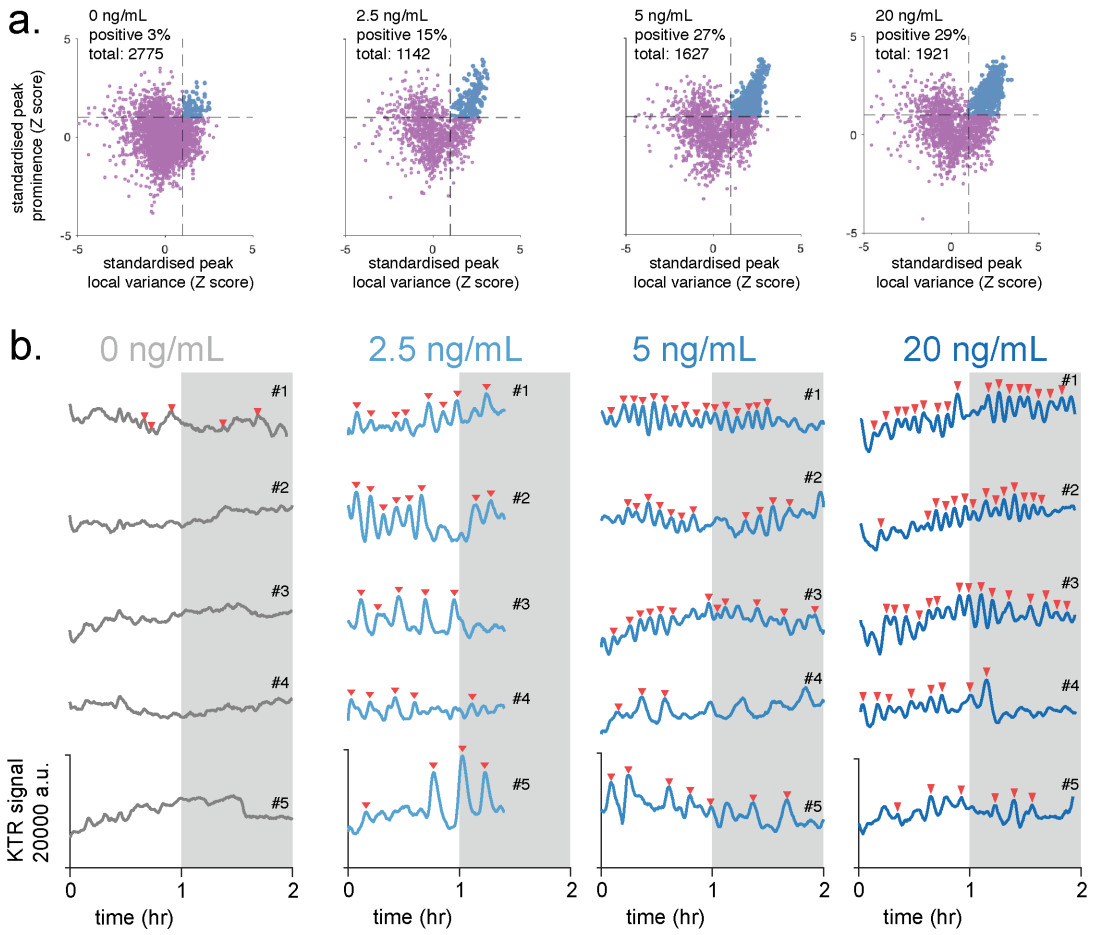

Fig 3.4.2: ERK dynamics are heterogeneous even in the presence of constant exogenous FGF4

a. *Threshold criteria for local maxima to be considered 'peaks'. Black dashed lines indicate the Z-score values of 1 on both peak prominence and local variance axes. Blue dots are local maxima that were annotated as peaks, while purple dots are local maxima that cannot be distinguished from the negative control, and are rejected as peaks.* ***b.*** *Five representative traces for Fgf4 mutant cells treated with the labelled concentrations of FGF4 as described in the methods. Thresholded 'peaks' corresponding to valid pulses are annotated with an inverted red triangle.*

Next, I accumulated data from all single cell timeseries to study population-level characteristics in the dynamics. Inter-pulse interval (IPI) was calculated per track as previously described, and histograms were similarly binned. The distribution of IPIs here too consisted of a single prominent mode followed by a long tail with increased frequencies of IPIs at approximate multiples of the modal value. I used a GMM fit approach to identify 3 components in the data where the first two represented the different timescales of rhythmic pulsing behaviour (**Fig 3.4.3a**, inset bar, red and yellow), and the third represented very long IPIs that came from tracks with very few peaks (**Fig 3.4.3a**, inset bar, grey). The 'fast' timescale corresponding to the component with a mean of between 6.2 – 6.5 min represented continuous rapid pulses (for example: **Fig 3.4.2b** 2.5 ng/mL trace 2; 5.0 ng/mL trace 1), and the 'slower' timescale, corresponding to the component with a mean of between 11.7 – 14.2 min, likely represented 'skipped' pulses, or cells with a range of slower pulsing rhythms (for example: **Fig 3.4.2b** 2.5 ng/mL trace 3, trace 5; 5.0 ng/mL trace 5). While the estimated mean value of the two timescales of IPIs did not systematically change across FGF4 concentrations, at 2.5 ng/mL a smaller proportion of the data points (37.8%) was represented by the faster component with a mean IPI of 6.44 min (**Fig 3.4.3a**, second row). At higher concentrations of FGF4, the fraction of IPIs represented by the fast component increased to 53.1% for 5 ng/mL and 55.3% for 20 ng/mL. Thus, most IPIs are faster at the two higher concentrations of FGF4.

The binned distribution of pulse durations was more symmetric than that of the IPIs, but contained a long tail with very low frequencies. I interpreted these as outliers caused by occasional failures of the pulse width estimation algorithm. Therefore, I used a 2-component GMM fit to separate the outliers (**Fig 3.4.3b**, inset bar, grey) and determine the mean pulse width (**methods 2.8.4**). With increasing concentrations of FGF, the mean pulse duration showed a decreasing trend, going from 3.55 min at 2.5 ng/mL, to 3.16 min at 5 ng/mL, to 3.0 min at 20 ng/mL (**Fig**

3.4.3b). These values are summarised in **Table T 1** and **Table T 2** for comparison between different experiments.

Thus, I find that characteristics of the ERK pulse dynamics are stable across a physiologically relevant concentration range. While I find slower IPIs and longer pulse durations at 2.5 ng/mL, these properties show no significant differences between 5 ng/mL and 20 ng/mL.

Consistent with these findings, overall peak frequency for each cell revealed that median frequency of the oscillations was significantly greater between 2.5 ng/mL and 5 ng/mL, and between 2.5 ng/mL and 20 ng/mL (**Fig 3.4.3c**). However, I observed no significant differences between 5 ng/mL FGF4 and 20 ng/mL FGF4 (**Fig 3.4.3c**). As ERK dynamics are not homogeneous across time, calculating an overall peak frequency is an underestimate of the actual possible pulse rate. To examine whether the maximum possible rate of pulsing changes with FGF concentration, I next calculated the pulse frequency over a moving window of 30 minutes (90 frames) to estimate the maximum windowed pulse rate (**Fig 3.4.3d**), as previously described. The maximum pulse rate was expressed as pulses-per-hour to maintain consistency with previous representations, but due to the shorter window for calculation used here, could only be estimated as an even number (2 x pulse $rate_{30min\ window}$). Consistent with the overall pulse frequency, the maximum pulse rate showed an increase between 2.5 ng/mL and 5 ng/mL, but then saturated with no further increase between 5 ng/mL and 20 ng/mL. The range of frequencies that individual cells possessed was also very similar between these last two conditions.

Together, these data show that while the frequency of ERK oscillations does increase with FGF dose, it has a very narrow dynamic range. This is especially evident when compared to the previous ERK phosphorylation western blots or the target gene transcriptional response. Thus, ERK pulsing frequency on its own cannot explain the dynamic range of FGF responses.

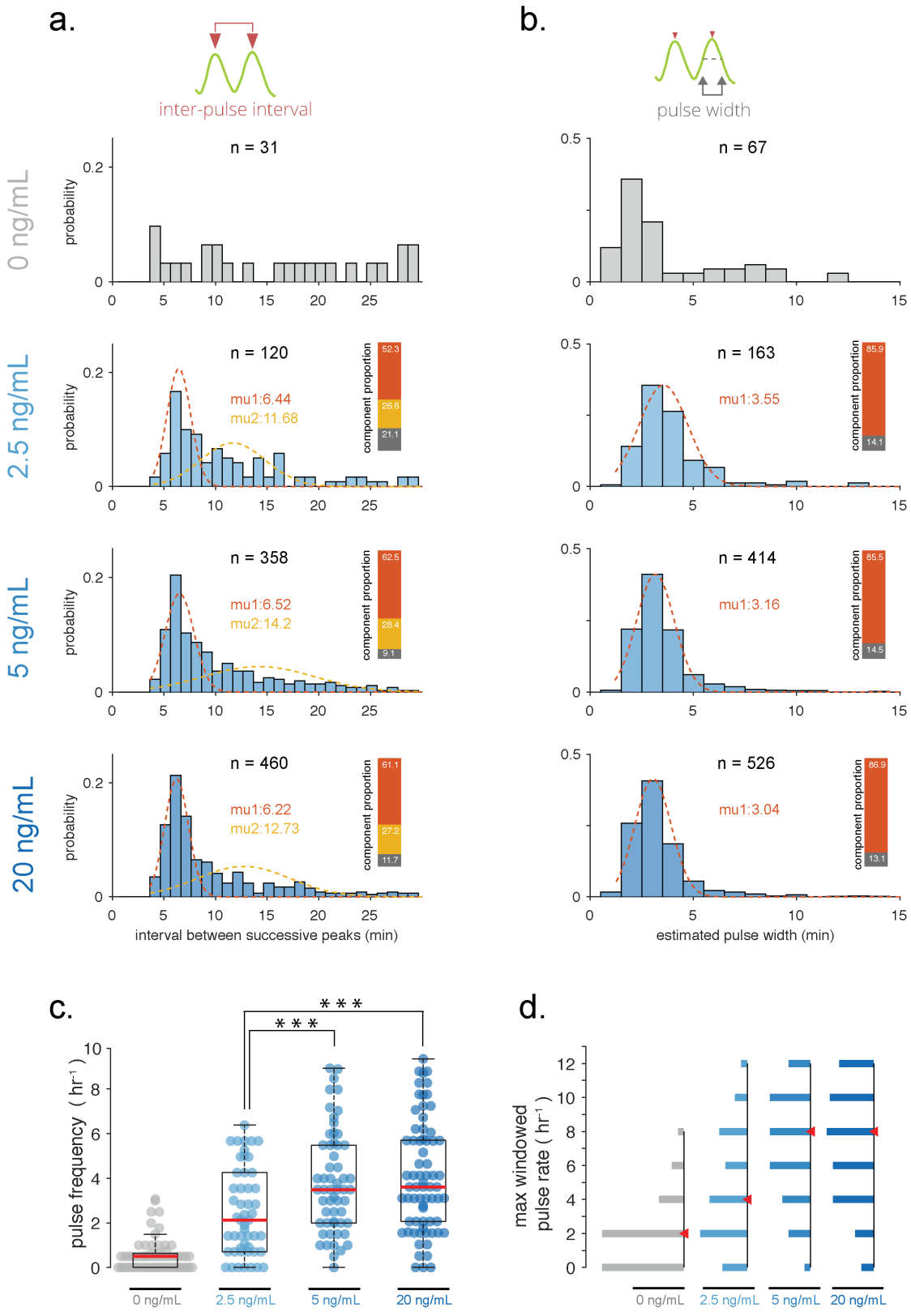

Fig 3.4.3: Properties of ERK pulse dynamics in response to FGF4 stimulus

***a**. Distribution of interpulse intervals for cells maintained in N2Ch + a range of FGF4 concentrations as mentioned on the left. The first two components of the GMM fit are shown as red and yellow dashed lines, and their means are inset in their respective colours. Proportion of data accounted for by each component shown as a vertical stacked bar and also provided in **Table T1**. **b**. Distribution of the*

*estimated pulse width for cells maintained in N2Ch + a range of FGF4 concentrations as mentioned on the left. The first component of the GMM fit is shown as a red dashed line, and the mean of the fit is inset in red. Proportion of data accounted for by each component shown as a vertical stacked bar. Fits were not carried out for the 0 ng/mL condition. Histograms are binned so each bar covers 3 frames and is centred on an integer. 'n' in each panel refers to the number of IPI or pulse duration data points considered. b. Overall pulse frequency per cell across a range of FGF concentrations. All treatments are significantly different from the negative control (p<0.01) (not indicated in the figure). Red line is the median, box bounds are the inter-quartile range (IQR), and the whiskers indicate 1.5*IQR. c. Maximum windowed pulse frequency for each cell, calculated within a sliding window of 30 minutes. Red triangle indicates the median. See Table T 1 for all values.*

3.4.3 Pulse shapes are robust and are not altered by FGF4 dose

While the timescale of ERK pulse dynamics were broadly similar across all FGF doses, individual traces showed some cells with distinctively shaped pulses (for example: **Fig 3.4.2b** compare 2.5 ng/mL trace 3 or trace 5 with 5 ng/mL trace 1). I next wanted to examine whether there was a systematic bias towards specific shapes at different concentrations of FGF4. I first defined the shape of a pulse as the timeseries data in a window of ± 3 mins from the peak of a pulse (**methods 2.8.5**). A difference in shapes could manifest as a difference in the symmetry of a pulse, implying a difference in the relative rates of the forward and backward reactions. Different pulse shapes could also result from different pulse widths or different amplitudes. However, as the transfer function between the amplitude of the sensor and phospho-ERK remains unknown, I chose to normalize each peak shape by dividing with the height of its peak. This operation would scale two pulses that have a similar baseline sensor signal but different amplitudes so that they appear similar (**methods 2.8.5**).

I started studying peak shape differences by first plotting the averaged pulse shape across all pulses recorded for a given treatment (**Fig 3.4.4a**). The 0 ng/mL negative control had very small amplitude pulses along with a higher basal sensor signal, while the three FGF-stimulated conditions showed larger amplitude pulses with a lower basal sensor signal in all conditions, and I noted no strong differences between the different concentrations (**Fig 3.4.4a**). Although the average shape of a pulse was

similar across all three FGF doses, calculation of an average can mask underlying systematic heterogeneities.

To study the distribution of individual pulse shapes as a function of changing FGF, I first needed to create defined categories of pulse shapes. To build categories, I used agglomerative hierarchical clustering to create a dendrogram of all pulse shapes detected across all four conditions. Similarity in shape was estimated using Euclidean distance as a distance metric, and Ward's method was used to specify linkages between clusters. Based on visual inspection of the linkage tree, I set a threshold linkage height of 31.6 resulting in 6 clusters (**Fig 3.4.4b**). The average pulse shape within each cluster is shown below the dendrogram in **Fig 3.4.4b**. These clusters represented both asymmetry in pulses shape (**Fig 3.4.4b** compare #1-Low with #2-Low or #1-Mid with #2-Mid), as well as differences in normalised pulse height. For ease of interpretation, I grouped clusters into Low (blue), Medium (green), and High (orange) groups based on pulse height. As can be seen from the dendrogram, this grouping also follows from the similarity between the groups (**Fig 3.4.4b**).

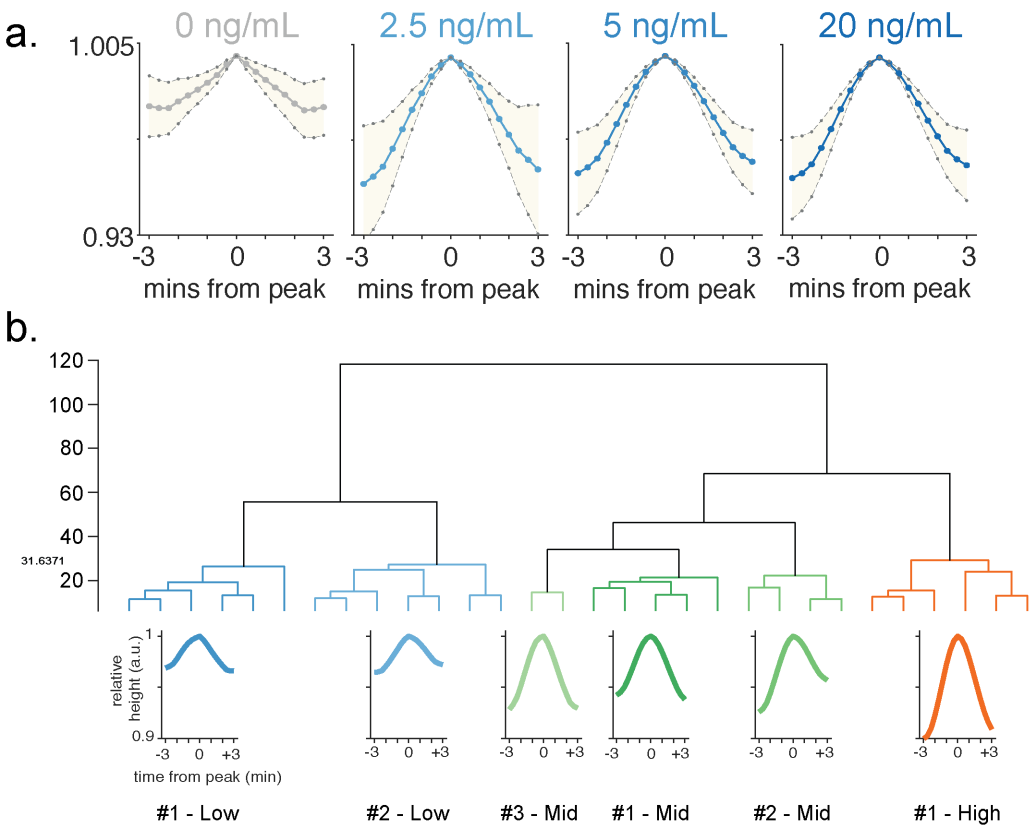

Fig 3.4.4: Hierarchical clustering of individual pulse shapes

a. *Average pulse shape for different FGF doses after aligning each pulse to its peak (solid line). Grey dotted line and shaded region indicates the standard deviation of all pulse shapes at the indicated FGF4 dose.* ***b.*** *Dendrogram of pulse shape categories, created using agglomerative hierarchical clustering. A cut-off linkage height of 31.6 was used to identify 6 distinct clusters. Branches are coloured according to the group that each shape category was assigned to, based on pulse height – Low (blue), Medium (green), or High (orange).*

After annotating all peaks according to the shape category they belonged to, I examined the distributions of shapes across the different FGF4 concentrations to study whether any systematic differences in cluster composition could be observed. Absolute counts of each pulse shape category are shown in **Fig 3.4.5b**. Consistent with the primary data shown in **Fig 3.4.2b**, the few pulses detected in the 0 ng/mL condition showed a higher sensor baseline signal and low amplitudes (**Fig 3.4.5b,c**), and almost all peaks were classified as 'Low' category peaks. Compared to this, the other three FGF-treated conditions contained pulse shapes from a mixture of categories, although there were no obvious differences between the conditions.

Thus, different concentrations of input stimulus did not induce any systematic bias in pulse shape.

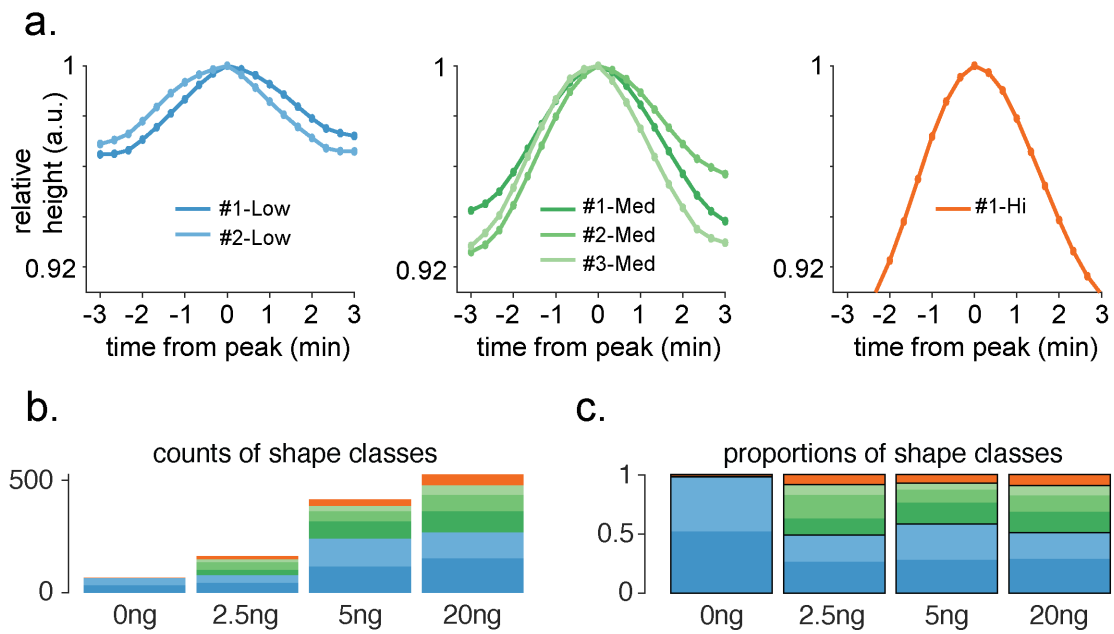

Fig 3.4.5: FGF dose does not bias pulse shape

a. *Three groups of the 6 pulse shape clusters, showing the average pulse shape in each cluster. In the Low and Medium groups, cluster IDs of #1 and #2 refer to the two clusters with opposing asymmetry.* ***b.*** *Counts of different pulse shapes for each FGF4 dose.* ***c.*** *Proportion of all pulses for each condition that are represented by the different clusters.*

I next asked whether individual cells have their own characteristic pulse shapes, as the shapes of the ERK pulses could be determined by the concentrations or activities of the proteins that comprise the biochemical network that results in dynamic ERK activation. This would test the idea that cell-intrinsic differences in the state of the signalling network is majorly responsible for the different pulse shapes, rather than external signals. The composition of single cell traces revealed that a great majority of cells expressed multiple pulse shapes (**Fig 3.4.6a**). The median number of different classes per cell at 5 ng/mL and 20 ng/mL was 3, with many cells showing up to all 6 different classes (**Fig 3.4.6b**) even within the short duration of this experiment. To see whether cells with more pulses had a greater variability in pulse shape, I plotted

the number of classes observed against the number of peaks detected per cell. While most cells showed greater variability in pulse shape with increase in number of pulses, a few cells (**Fig 3.4.6c**, light grey dots on the right) showed consistent pulsing with pulses of similar shape. Thus, single cells show great variability in pulse shapes, and most individual cells do not possess a 'signature' shape. Taken together, these results indicate that there are no systemic biases in pulse shape, either as a consequence of FGF4 stimulus levels, or as a result of cell-intrinsic differences.

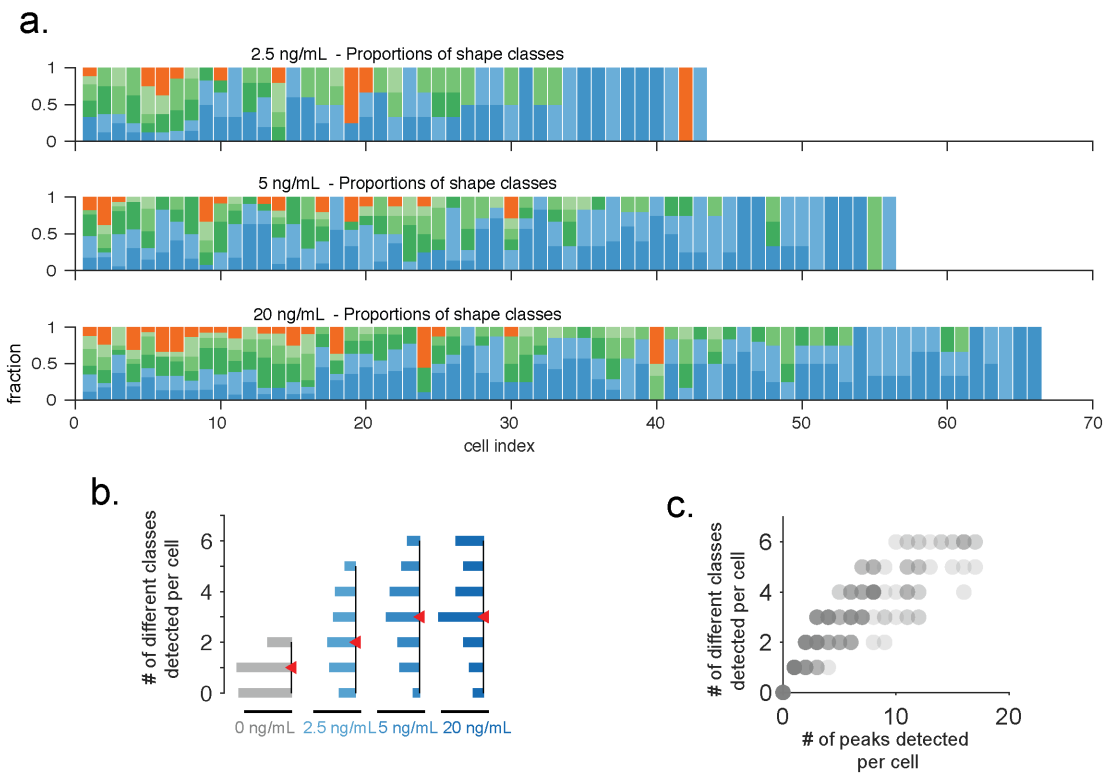

Fig 3.4.6: Most cells do not show 'signature' pulse shapes

a. *Single cells with their relative proportions of each pulse shape cluster color-coded as in* ***Fig 3.4.5****. Cells are sorted from (L->R) highest pulse count to lowest pulse count. Each row is a different concentration of FGF4 as labelled .* ***b.*** *Number of different classes of pulses detected per cell.* ***c.*** *Number of different classes plotted against the total number of peaks detected per cell. Each dot is one cell.*

3.4.4 FGF increases the regularity of ERK pulses

As shape features of individual pulses stayed relatively constant across FGF concentrations, I next wanted to examine whether the regularity of multiple pulses

was affected by FGF dose. We used two alternate analysis methodologies to validate our results. The first method, described in Raina et al., 2020a, identifies pairs of pulses that are located close to one another as being 'consecutive', a term that indicates regularity. Consecutive pairs of pulses were those with a short 'silence' interval between them (**Fig 3.4.7a)**. The threshold for identification of 'consecutive' pulses was those pairs of pulses where:

$$\text{'}silence\text{'} < \frac{\text{'}joint\ duration\text{'}}{2} \qquad \text{(dotted line, } \textbf{Fig 3.4.7b}\text{)}$$

This analysis showed an increase in the fraction of consecutive pairs, from 49.2% at 2.5 ng/mL, to 57.6% and then 63.9%, at 5 ng/mL and 20 ng/mL respectively. This demonstrated that pairs of pulses show increased regularity.

The second analysis methodology for measuring regularity was previously described in this thesis. This method is based on the distributions of IPIs. Pulses that are very regular occur in 'clusters' rather than being homogenously spread out throughout the track. This is substantiated by the two-fold increase in the windowed pulse rate compared to the overall pulse frequency as described in **Fig 3.4.3d.** Thus, to examine the fraction of pulses that are part of a cluster, I first needed to set a threshold for the value of IPI that would enable identification of clustered pulses. As I had previously identified at least two timescales of IPIs, I set an interpulse interval threshold as the mean + SD of the second component of the IPI distribution. This separated clusters of pulses that have long interpulse intervals between them, while allowing for both the fast and highly regular pulses, as well as the slower or less regular pulses to qualify as being part of a cluster. Here too, I observed a trend towards increasing pulse likelihoods at higher FGF concentrations, suggesting that ERK oscillations are more extensive at higher FGF4 concentrations.

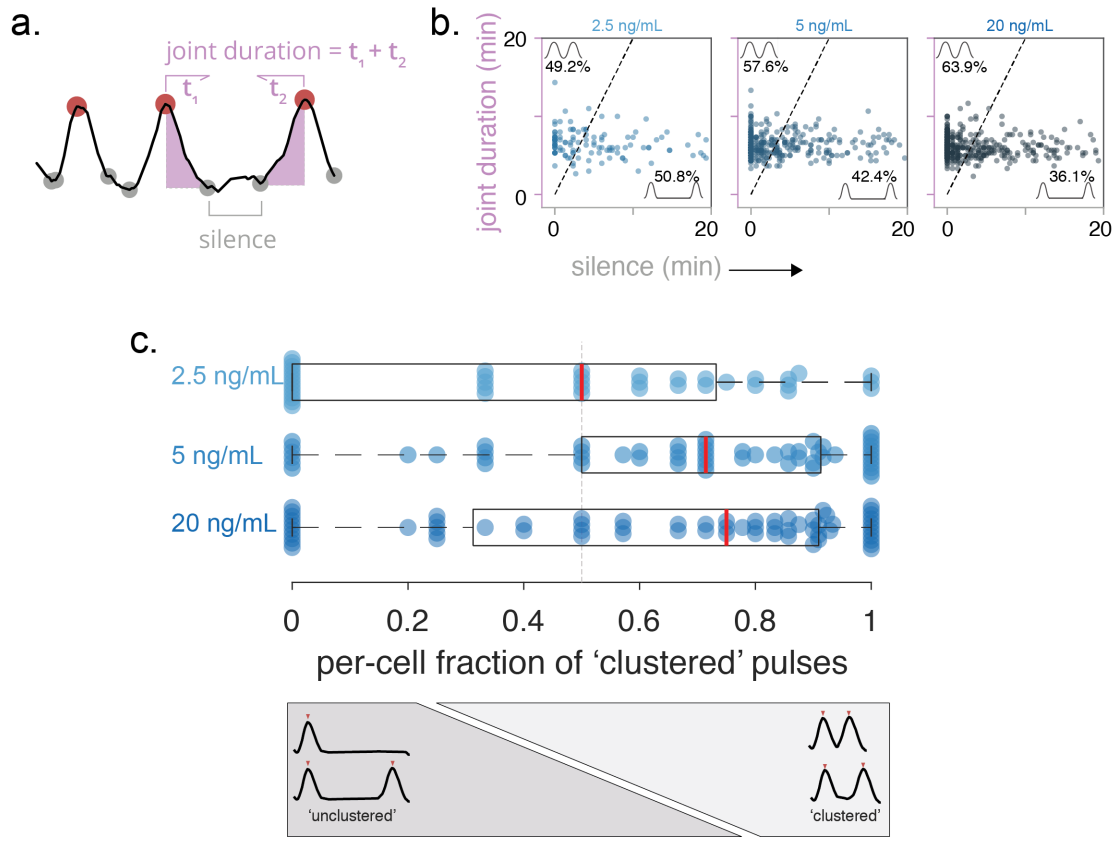

Fig 3.4.7: FGF dose increases the fraction of clustered pulses

a. *Definition of 'Joint Duration' and 'Silence' interval features from* Raina et al., 2020a ***b.*** *Pairs of consecutive pulses identified by plotting their joint duration against the silence interval. Dotted line indicates the threshold line with a slope of 2. Points above the threshold line identify pairs of pulses that qualify as being 'consecutive'. Concentration of FGF4 as labelled.* ***c.*** *Fraction of pulses per cell that are 'clustered'. Red line indicates median, box bounds represent inter-quartile range, and whiskers indicate 1.5* IQR.*

In summary, these results reveal that ERK pulses have a characteristic duration that is independent of FGF4 concentration. With increasing FGF concentrations, the increase of both pulse rate and pulse regularity, together with the narrowing of the distributions of pulse duration, suggests that FGF controls the extent of ERK oscillations within a small dynamic range.

3.5 ERK pulses occur over a changing baseline of ERK activity

3.5.1 phospho-ERK staining shows a changing baseline of ERK activity

Previous results showed that the signalling response of mESCs, measured by the relative amount of phospho-ERK (**Fig 3.4.1b,c**), approaching saturation between 20-50 ng /mL (**Fig 3.4.3c,d**). Consistent with this result, mESCs showed a quantitative upregulation of transcriptional response with FGF4 dose, only starting to show saturation above 50 – 100 ng /mL (**Fig 3.4.1d,e**). In contrast to these observations, the frequency of ERK pulses showed a very narrow dynamic range of response, only changing between 0 - 5 ng/mL, and saturating thereafter (**Fig 3.4.3c,d**).

How can a population-averaged measurement of ERK activity (i.e. western blot) show an increase from 5 – 20 ng/mL FGF4 without a corresponding increase in single-cell frequency of ERK pulsing? Two scenarios could reconcile these findings: either the amplitude of the oscillations could increase and thereby increase average ERK activity, or the oscillations of ERK activity could occur over an increasing baseline. Since the ERK-KTR sensor only reports changes in ERK activity rather than absolute levels of phospho-ERK I couldn't use the sensor for this measurement. Instead, I needed to directly probe phospho-ERK by immunostaining in order to distinguish between these scenarios.

I started by treating cells with FGF according to the scheme in **Fig 3.4.1a** to replicate the conditions under which the steady-state FGF4 stimulation was carried out. I then fixed and stained the cells for phospho-ERK, and quantified single-cell phospho-ERK levels. As both nuclear and cytoplasmic phospho-ERK increase in a correlated manner (**Fig 3.1.1b**), I used E-cadherin staining to mark the boundaries of cells and measure the whole cell mean fluorescence intensity of the phospho-ERK stain **(Fig 3.5.1a**). Quantification of these data reveals a distribution of phospho-ERK levels with

increasing median values **(Fig 3.5.1b,c**). If this increase in phospho-ERK was solely due to an increase in the amplitude of ERK oscillations, one would expect all five distributions to have similar lower limits, but increasing upper limits and medians. However, in **(Fig 3.5.1b,c**) it can be seen that not only is there an increase in the median level, but also both upper and lower limits of the distributions shift to higher values (***Table T 3***). This data suggests that basal phospho-ERK levels increase with FGF treatment, and that oscillations of ERK activity occur on top of this changing baseline.

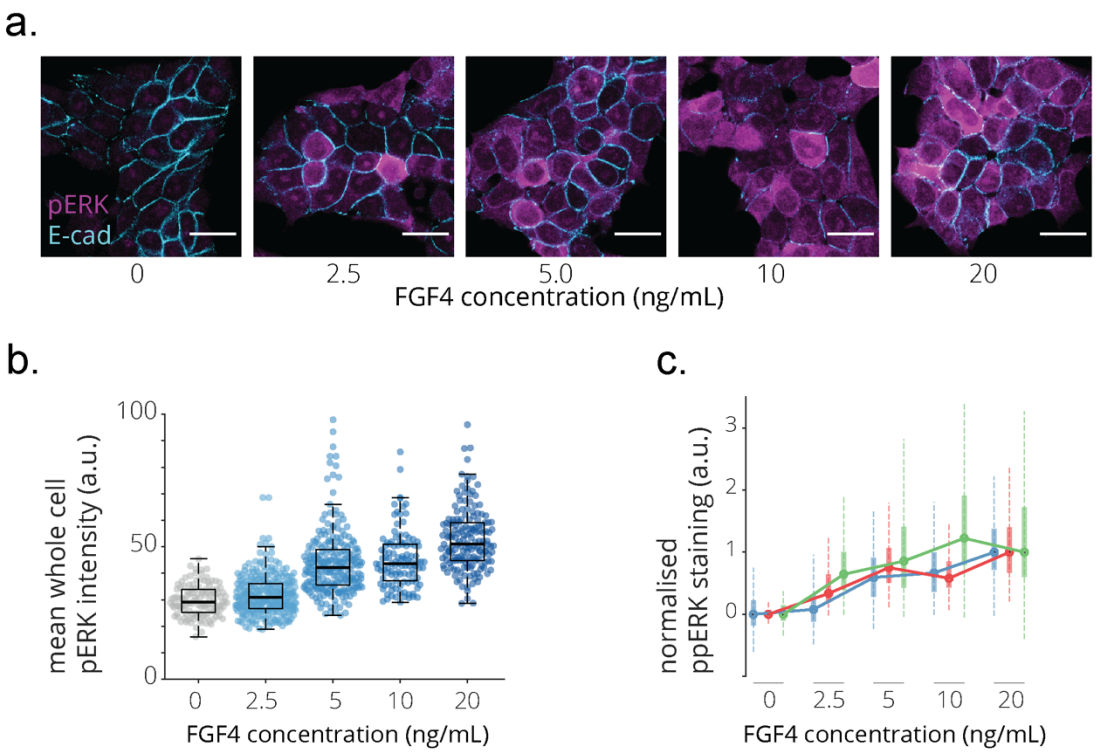

Fig 3.5.1: Basal phospho-ERK levels increase with FGF dose

a. *Immunostaining for phospho-ERK (purple) and E-Cadherin (cyan) to mark cell boundaries. Cells were treated with FGF as in the scheme in* ***Fig 3.4.1****. Scale bar = 20 μm.* ***b.*** *Quantification of phospho-ERK intensity in one immunostaining experiment as shown in a. Dots indicate single cells.* ***c.*** *Normalized distributions of single cells for N=3 experiments. Solid vertical boxes represent the inter-quartile range (IQR), and dotted line (whiskers) indicate 1.5*IQR.*

3.5.2 Acute stimulation with FGF induces a high transient of ERK phosphorylation

Previous descriptions of a simple negative feedback oscillator have suggested that an increase in stimulus strength can increase the baseline of the response variable, while still maintaining limit cycle oscillations of the response variable (Tyson et al., 2003). To experimentally test whether the oscillations of ERK activity we observe are qualitatively consistent with this model, I needed to observe ERK pulses upon inducing a large increase in the basal phospho-ERK. Although data in the previous section suggested that basal phospho-ERK levels are higher at higher FGF4 doses, the differences are small. This is partially due to the experimental design, as the protocol allows cells 24 h to acclimatise and adapt to FGF4 in the medium before the assays are carried out. I next designed an alternate experimental approach to further increase phospho-ERK response. In mESCs, previous studies have reported that moving cells from the ERK inhibited '2i' medium to the serum-containing S+L medium can induce a transient overshoot of phospho-ERK levels (Deathridge et al., 2019; Nett et al., 2018). Analogous to this protocol, I maintained the *Fgf4* mutant cells in serum-free N2B27 medium to simulate chronic deprivation of phospho-ERK, before transitioning them to medium containing FGF4 (**Fig 3.5.2a**). With this protocol, I was able to induce a transient ERK overshoot for varying concentrations of FGF4, as measured by western blots (**Fig 3.5.2b,c**). Blots were quantified by normalizing all phospho-ERK/total ERK band intensities in each blot to a reference sample (**Fig 3.5.2b,** starred lanes). The exact same amount of this reference sample was loaded in each gel, thereby allowing phospho-ERK/total ERK values to be compared between all 4 gels, relative to the reference sample. As expected, this quantification demonstrated that the peak phospho-ERK/total ERK was greater at high concentrations of FGF. Additionally, it revealed a transient phospho-ERK response, which dropped to about half of the peak value within 4 h of FGF stimulation (**Fig 3.5.2c**), and subsequently changed little between 4 h and 7 h. This result

demonstrated that by performing an acute stimulus of FGF4, following chronic FGF/ERK signalling deprivation, I can experimentally induce a transient peak in ERK activity.

Using this approach to increase basal ERK activity, I next examined ERK-KTR cells stimulated on the microscope (**Fig 3.5.2d**). Due to technical limitations, the frame interval was limited to 1/60 s in order to image all conditions simultaneously. While FGF-containing medium was added to the cells in the indicated conditions, for the negative control I performed a medium change to rule out the possibility that ERK activity could be induced by simply replenishing the serum-free basal medium. Montages of single cells are shown in **Fig 3.5.2e**, demonstrating a sharp increase in KTR sensor signal immediately after stimulus. This observation was reflected in the average of all single cell traces for a given stimulation, showing that while the 0 ng/mL negative control did not change signal intensity after medium replenishment, the FGF-treated cells all show a sustained increase in KTR sensor signal (**Fig 3.5.2f**, left). These traces further supported the notion that the KTR sensor does not directly report levels of phospho-ERK, as no differences in the cell-averaged signal could be observed between the different FGF concentrations, although this could also be due to limitations in the dynamic range of the sensor (**Fig 3.5.2f**, left). Despite this increase in KTR signal however, some fluctuations in sensor activity could still be observed in single cells (**Fig 3.5.2e**).

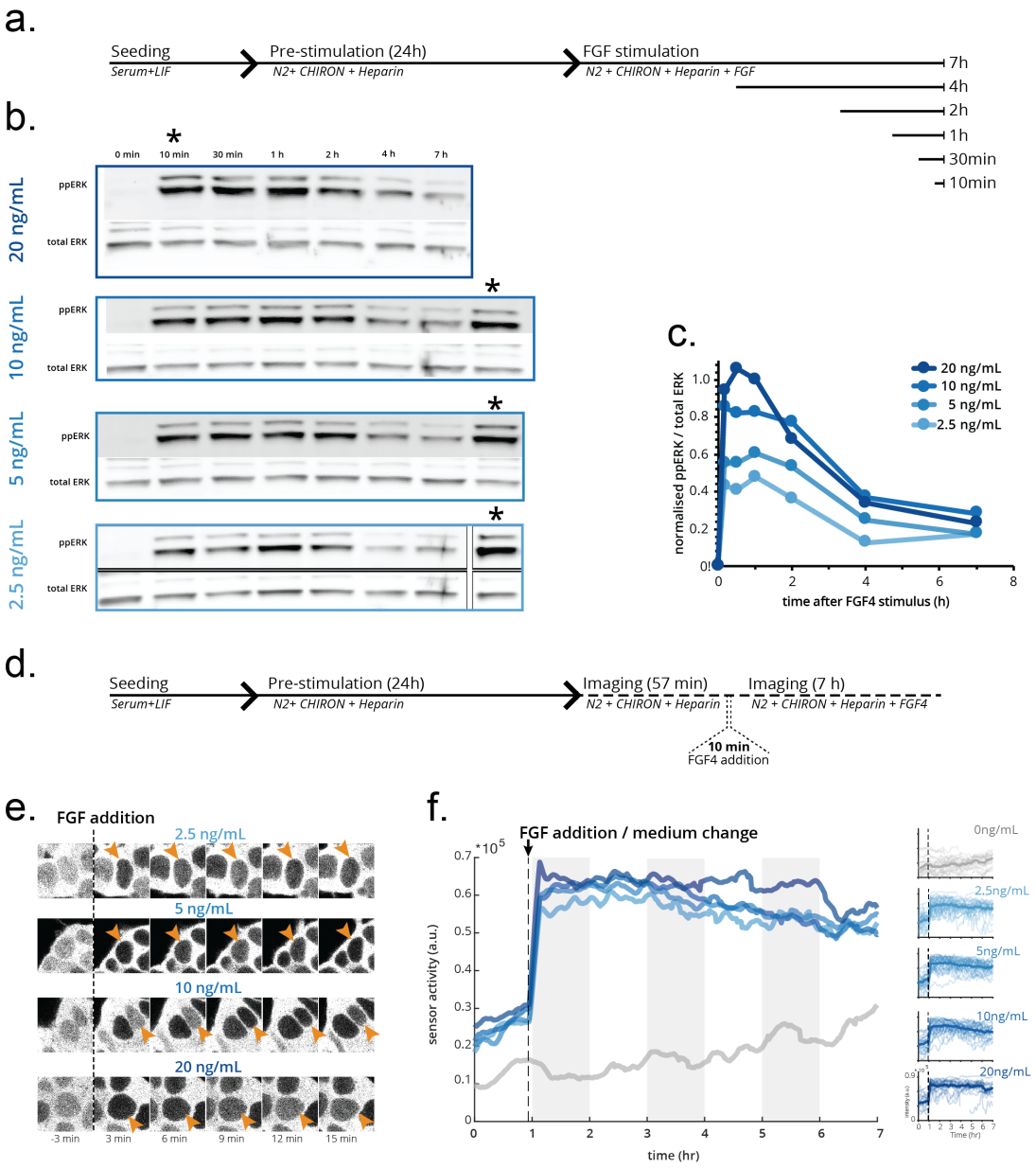

Fig 3.5.2: Acute stimulation induces a transient increase in phospho-ERK levels

a. *Experimental protocol to induce a transient increase in phospho-ERK.* ***b.*** *Western blots for ppERK and total ERK treated with 2.5 – 20 ng/mL FGF4 as indicated, according to the scheme in a. Bands marked with the * are loaded with the same amount of the same sample as a reference band.* ***c.*** *Quantification of data in b, relative to the reference band in each blot. N = 1.* ***d.*** *Experimental protocol to induce a transient increase in phospho-ERK in the live-imaging experiment.* ***e.*** *Montages from the live-imaging experiment of ES cells expressing the KTR sensor, showing strong nuclear localization upon acute stimulus.* ***f.*** *Left: Averaged KTR signal for cells treated with 0 ng/mL (n = 28), 2.5 ng/mL (n=31), 5 ng/mL (n=33), 10ng/mL (n=28), and 20 ng/mL (n=21) of FGF4. Right: Thin lines represent single-cell KTR traces, and the thick lines represent the averaged signal for the respective condition.*

3.5.3 Pulses of ERK activity can be detected at high phospho-ERK levels

To demonstrate whether pulsatile ERK activity and the basal ppERK overshoot were co-incident, I next wanted to examine the timing of ERK pulses after stimulation. I first used the previously described peak thresholding approach (**methods**) to identify pulses of ERK activity in single-cell traces (**Fig 3.5.3a**). Pulses were identified for the post-stimulation portion of each cell track, starting 15 min after stimulation to avoid detecting the increase in basal signal activity as a 'peak'. I observed considerable heterogeneity in pulsatile behaviour between cells. Many cells, especially at the higher concentrations of FGF (5 ng/mL and above), showed a sustained elevation of ERK activity without the appearance of detectable pulses (**Fig 3.5.3a**; 5, 10, 20 ng/mL FGF; bottom trace). However, a few cells showed sections of regular patterns of pulsing (**Fig 3.5.3a**; 2.5 ng/mL top trace, 5 ng/mL middle trace). Due to the reduced dynamic range of the sensor, pulses had a reduced amplitude, and in many cells were not even detectable (**Appendix 7.9 - 7.13**).

To examine the timing of the detected pulses, I plotted the time of detection of the first pulse after stimulation (**Fig 3.5.3b**). In most cells, the first detectable pulse was observed within 1 h of FGF stimulation (**Fig 3.5.3b**). The long tail of cells which are apparently slow to start pulsing are mostly composed of those that show 'sustained' ERK activity without any clear pulses. This timing is co-incident with the phospho-ERK overshoot demonstrated in **Fig 3.5.2b,c**. Thus, pulsatile ERK activity can be observed in some cells even in conditions where phospho-ERK levels are elevated.

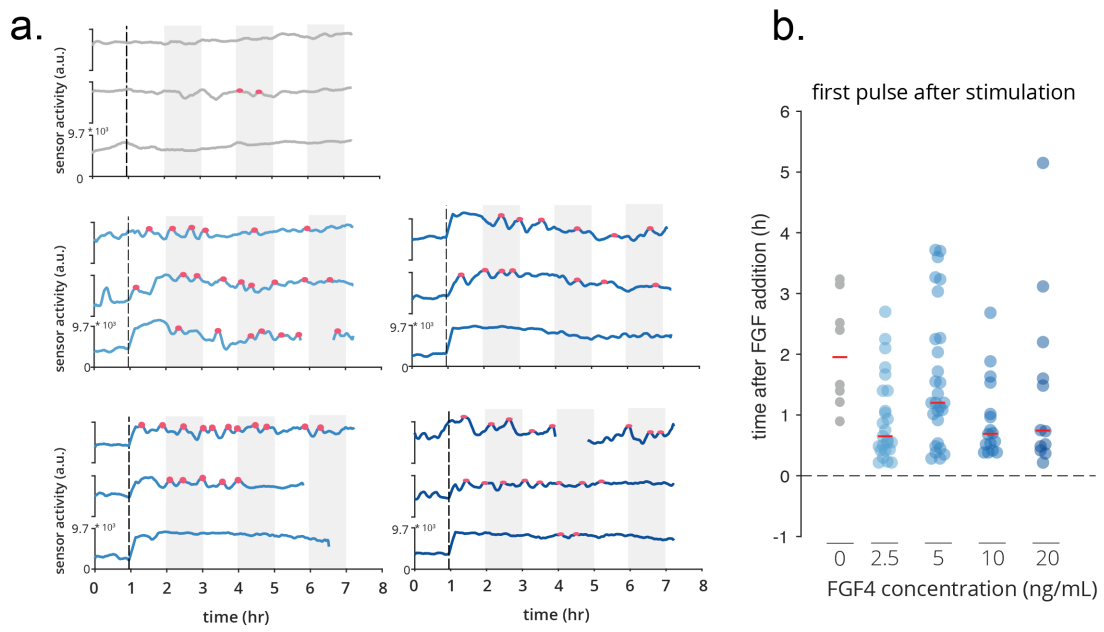

Fig 3.5.3: ERK pulses can be detected even after transient stimulation

a. *3 single-cell traces shown for each condition. Red dots indicate detected pulses. Pulse detection was only carried out 15 min after the stimulation to prevent spurious peaks from being called. Vertical dashed line represents the time of stimulation* ***b.*** *Time of detection of the first pulse after stimulation. Dots represent single cells, and the red horizontal lines indicate the median. Horizontal dashed line represents the time of stimulation.*

3.5.4 Pulse width and frequency is lower following stimulation

I next characterised the timescales of the pulses that occurred at elevated phospho-ERK levels. Due to the small number of observations and observed temporal heterogeneity in pulsing, here I used only the estimated pulse width and the maximum windowed pulse rate to characterise the dynamics. The median estimated pulse widths were much larger than the previously determined values, ranging from 14 min for 2.5 ng/mL to 15.7 min for 20 ng/mL (**Fig 3.5.4a**). While this indicated that pulse widths are higher at high basal phospho-ERK levels, there is no systematic concentration dependence across the range of FGF doses tested. Thus, although the western blot results suggest a concentration-dependent increase in basal phospho-ERK levels, this does not translate into a corresponding change in pulse widths.

I next calculated a maximum windowed pulse rate to estimate the frequency of pulsing (**Fig 3.5.4b**). As can be seen from both single cell traces (**Fig 3.5.3a**) and the quantification (**Fig 3.5.4a**), pulse rate is much slower than the previously determined values (**Table T 1**). One caveat of these results on the characteristics of ERK dynamics is that they could be affected by the poor dynamic range of the sensor in this experimental regime.

In conclusion, at highly elevated levels of phospho-ERK, pulses have a longer duration and a corresponding reduction in pulse frequency was observed. Together, these data showed that the pulsatile ERK activity detected by the sensor can occur on top of different baseline levels of phospho-ERK, albeit with altered dynamics.

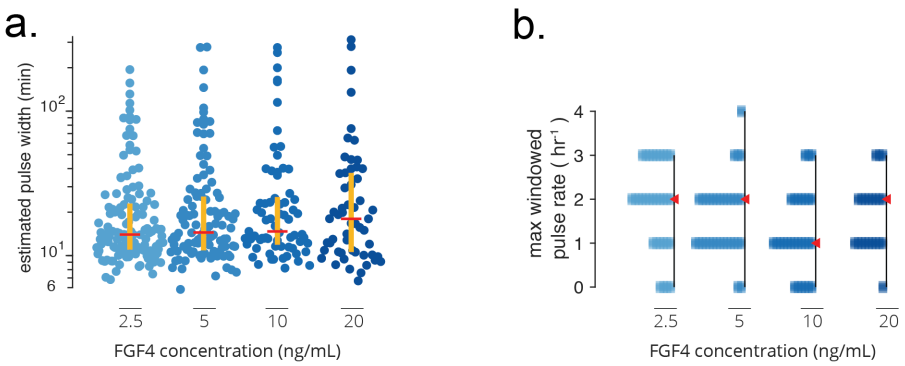

Fig 3.5.4: ERK pulses are broader and slower at elevated phospho-ERK

a. *Estimated pulse width for individual pulses for different concentrations of FGF4. Vertical orange line represents the inter-quartile range. Red horizontal line represents the median.* ***b.*** *Maximum windowed pulse frequency per cell, calculated over a sliding window of 1 h on each cell track. Horizontal length of each bar corresponds to the number of observations. Red triangle indicates the median.*

4 Discussion

Work presented in this thesis demonstrated that ERK activity in pluripotent cells is pulsatile, and that these dynamics are triggered by a single ligand, FGF4. As pluripotent cells crucially depend on FGF/ERK signalling to differentiate both *in vivo* as well as *in vitro*, FGF4 has broad physiological relevance. Here, I have reported FGF4-triggered pulses of ERK activity under a range of different stimulation conditions. These dynamics were generated cell-intrinsically and were largely independent of the mode of ligand presentation. The regularity of ERK dynamics observed here indicates that ERK pulses could be oscillatory, with individual cells showing transitions between oscillatory and non-oscillatory states.

4.1.1 ERK activity is intermittent and oscillatory in mouse ESCs

In this thesis, I used a translocation sensor to demonstrate that ERK activity in mouse embryonic stem cells is dynamic and can be very regular under multiple signalling regimes. Regular pulsing of ERK was interpreted as oscillations, and this conclusion was based on the measurements of inter-pulse intervals and the pulse widths. For individual pulses, inter-pulse intervals and pulse widths were correlated at low values of IPIs: thus pulses are shorter when the frequency is faster. For these pulses, pulse durations and IPIs had similar values, suggesting that pulses tended to occur in immediate succession without a significant non-pulsatile time between them (Fig 3.2.7**a**, second or third panel). Thus, these pulses with higher frequencies were considered to be 'clustered' or occurring with a high degree of regularity, and I interpreted these as indicative of oscillations. A smaller number of pulses had long

inter-pulse intervals between them. Together, these data suggested that 'clusters' of regular pulses were separated by non-pulsing periods. Thus, ERK pulsing was observed to be intermittent.

This proposal of intermittency in pulsing was further substantiated by the results on pulse frequency and max windowed pulse rate. The maximum windowed pulse rate, calculated over a moving window of 0.5 – 1 hr based on the experiment, was approximately twice that of the overall frequency calculated for an experimental condition (**Table T 1**). As the windowed pulse rate is calculated over a smaller duration than overall length of a track, this increase in windowed pulse rate implied that pulse dynamics were heterogeneous over time, and that cell tracks consisted of sections of rapid pulsing alternating with less frequent pulsing.

In other signalling contexts and cell types, ERK pulses have been shown to be stochastic (Aoki et al., 2013) or oscillatory (Shankaran et al., 2009). Despite differences in the description of the dynamics, pulse widths were shown to be relatively insensitive to stimulation strength. Similar to these reported findings, I showed that pulse widths remain fairly conserved in steady-state paracrine signalling and across a range of exogenous signalling (**Table T 1**), and were unimodally distributed across a narrow range of values ranging from 2.8 min to 3.5 min. This hints that the dynamical system which gives rise to ERK pulses is organised such that pulse widths are generally independent of stimulus strength, and therefore this property might be crucial for the correct functioning of ERK signalling.

Previous studies have observed more irregular stochastic pulsing of ERK activity (Goglia et al., 2020; Aoki et al., 2013), and have used the long-tail in the distributions of IPIs in their data to substantiate the interpretation that pulses are stochastically distributed across a cell track. Measures of regularity defined in this thesis contradict the idea that pulses are randomly distributed across a cell track. Additionally, the distributions of interpulse intervals in different stimulation conditions shown here all have a prominent mode at similar values ranging from 5.6 – 6.7 min, along with a

small shoulder between 11.6 – 13.9 min. As this shoulder has consistently shown up in many experiments, I have interpreted it to indicate that the distribution of IPIs consists of a mixture of at least two different distributions corresponding to different timescales of pulsing. Certainly, pulses with regularly occurring but slower pulsing cadences can be observed (Fig 3.2.4, Fig 3.2.1, indicated in the text), although in some instances these slower rhythms could also come from cells 'skipping' a pulse while keeping track of the rhythm, or by the peak detection missing one peak in an otherwise regular series of peaks.

Thus, while stochastic occurrence of the peaks cannot be firmly ruled out, the primary data often shows cells that display regular oscillatory behaviour. It is therefore likely that a mixture of regular oscillations along with some stochastic pulsing is observed in mouse ES cells, bearing some qualitative resemblance to p53 pulses in MCF-7 cells (Mönke et al., 2017).

4.1.2 Properties of ERK oscillations show limited changes with FGF stimulus strength

To determine whether the frequency or other dynamic properties of ERK oscillations change with stimulus strength, I titrated FGF4 onto *Fgf4* mutant cells. Since the *Fgf4* mutants had very minimal background phospho-ERK levels, I was able to map exogenously added FGF4 concentrations to ERK response without interference from other signalling inputs. In the FGF addback experiments, a systematic but non-significant reduction in pulse width was observed with increasing concentrations of FGF4. At 2.5 ng/mL a pulse width of 3.5±1.2 min was observed, reducing to 3.2±0.9 min at 5 ng/mL. At 20 ng/mL, a pulse width of 3 min was observed, closest to the value of 2.8±1.0 min recovered for the paracrine signalling condition.

The distributions of IPIs were similar across all steady-state signalling conditions, with the shortest IPIs coming from the paracrine-signalling N2Ch condition. Across the

range of FGF concentrations tested, 20 ng/mL FGF4 (with an estimated mean of 6.2±1.2 min) most closely resembled the paracrine condition, although the IPIs estimated for the paracrine signalling condition were shorter at 5.6±1.3 min.

Using the pulse frequency and maximum windowed pulse rate, this thesis showed that ERK pulsing frequency only changes over a narrow range of FGF concentrations compared to the transcriptional response. Although the maximum windowed pulse rate was always higher, it showed a similar trend to the overall pulse frequency values. The lowest windowed pulse rate of 4 pulses hour^{-1} was observed at 2.5 ng/mL of FGF4, and this increased up to 8 pulses hour^{-1} for both 5 ng/mL and 20 ng/mL of FGF4 (**Table T 1**). Thus, even though the pulses were not uniformly distributed across a cell track, both the local frequency of ERK pulses, as well as the frequency across the entire cell track appear to saturate at 5 ng/mL of FGF4. The frequencies of ERK pulses in paracrine signalling conditions closely resemble both the 5 ng/mL and the 20 ng/mL conditions, demonstrating that the titration experiments described here are within physiological signalling regimes.

On the basis of these observations, cells in the paracrine signalling regime appear to have more than 2.5 ng/mL of FGF4 in their environment, and share similarities with the 5 ng/mL and 20 ng/mL FGF4 conditions.

A previous study has shown that different types of oscillators can be distinguished based on the changes in oscillatory dynamics with input stimulus strength (Tsai et al., 2008). Delayed negative feedback oscillators can show a narrower frequency response range than 'negative-and-positive feedback' oscillators (Tsai et al., 2008). Based on this, one could speculate that the data presented in this thesis implies a delayed negative feedback circuit within the MAPK cascade could be driving the oscillations. While this observation of a limited dynamic range of frequency response is not concrete evidence for the underlying organization of the signalling network, it could lay the foundation for future testing of biochemical models that help characterise the dynamic behaviour reported here.

4.1.3 ERK pulses occur on top of a changing baseline

In comparison to the ERK phosphorylation data (Fig 3.4.1**b,c**) or the transcriptional response (Fig 3.4.1**d,e**), the frequency of ERK pulses saturates at much lower concentrations of FGF stimulus and therefore has a lower dynamic range. As a consequence, simply measuring ERK pulse frequency will be a poor predictor of the concentration of FGF stimulus. Although frequency-encoding of information has been proposed in other systems (Albeck et al., 2013; Young et al., 2013; Cai et al., 2008), ERK pulse frequency in ESCs is unlikely to be the only carrier of information on the concentration of external growth factor. Overall ERK activity can be thought of as a ratio between phospho-ERK and the phosphatases that dephosphorylate ERK targets. As the ERK KTR sensor only reports on ERK activity rather than the absolute amount of phospho-ERK in a cell, it is likely that the oscillations we observed occur on top of a changing baseline level of phospho-ERK. This hypothesis is substantiated by the acute stimulation experiments that show ERK pulses are possible to observe even at highly elevated phospho-ERK levels (**Section 3.5**). Thus, growth factor concentration could be encoded in a mixture of ERK activity dynamics and basal phospho-ERK levels.

4.1.4 Limitations of the sensor

The ERK-KTR sensor that we use throughout this study critically depends on nuclear import and export as a readout for ERK activity, and has to therefore undergo a series of sequential reactions before we detect it. Compared to a more direct sensor, such as the unimolecular FRET sensor EKAREV (Komatsu et al., 2011), it is more possible that the timescales reported by the sensor could be modified by rate-limiting steps in the export and import process that are unrelated to ERK activation. However, the dual sensor experiments (**Fig 3.1.5**) demonstrate that both sensors track each other

closely with a time-resolution of 40 s. Thus, even at the fast timescales of ERK activity that we observe, our results are unlikely to be significantly altered by our choice of sensor.

Previous work has suggested that ERK substrate sensors could act as a 'sponge' by introducing an abundance of ERK binding sites, thereby altering the system (Kim et al., 2011). As ERK-KTR cells were shown to contribute to the germline in mouse embryos (Simon et al., 2020) this indicated that they retained the capacity for normal development. Additionally, in the dual sensor experiments (**Fig 3.1.5**), where two sensors were simultaneously overexpressed, even the very high amounts of sensor expression did not affect the dynamics we observe, and many pulses in the trace shown were within 10 minutes of each other (see trace in **Fig 3.1.5**).

While a relation between the amplitude of an alternative ERK activity sensor and phospho-ERK levels has been proposed (Aoki et al., 2013), a poor correlation was observed in that study. In the FGF4 acute stimulation experiments, no systematic relation between amplitude of sensor and FGF4 concentration could be determined (see traces, **Fig 3.5.2**), thus it is unlikely that the amplitude of the sensor linearly reports on the amount of phospho-ERK. Given the absence of a model to describe the transfer function between sensor amplitude and phospho-ERK, I have chosen not to emphasize interpretation of amplitude information in this study.

4.1.5 Sources of heterogeneity

In some tissues and culture systems, spatially organised pulses of ERK activity have been observed (Aoki et al., 2017; Hiratsuka et al., 2015), prompting the question of whether we expect spatial organisation in the heterogeneity of ERK pulse dynamics within a colony. While colony-level spatial organisation of receptors has been

observed for BMP signalling under specific conditions (Etoc et al., 2016), single cell RNA sequencing has shown that nearly all ES cells express FGF receptors (Max Fernkorn, personal communication). Additionally, recent work has demonstrated that the range of paracrine FGF signalling in ESCs is approximately 2 cell diameters (Raina et al., 2020b). Given the spatial reach of paracrine FGF and the small colony sizes, there is unlikely to be much difference in local FGF within a colony. Further, since the dynamic range of the ERK pulse frequencies is very limited, it is unlikely that we would observe differences between cells on the edge of a colony versus cells in the centre. However, I cannot completely rule out that the spatial address might also contribute to differences in pulse dynamics. As location data for individual cells was not taken into account while pooling them, it is possible that the heterogeniety we observed could be influenced by location within a colony.

Additional sources of heterogeneous ERK dynamics could either be the pulsatile production of the FGF ligand in the signal-sending cells, or differences in protein expression within the signal-sensing network. To control for the former, I used the *Fgf4* mutant cells – thereby eliminating the possibility of pulsatile ligand production - and designed experiments that used an excess of exogenous FGF4 in the extracellular medium. Colony sizes were kept small in these experiments to ensure all cells have access to the FGF in solution. However, even after trying to ensure uniformity in FGF stimulus, the heterogeneity in individual pulse durations and shapes persisted. Examining pulse shapes revealed that there was no systematic relation between pulse shapes and FGF stimulus concentration, indicating that the heterogeneity is unlikely to come from differences in local FGF concentration. As individual cells will have a slightly different protein complement, each cell could have a slightly different characteristic ‘signature’ of ERK pulse shape. However, when I looked at the number of different pulse shapes in a single cell track over time, considerable variability was found. In general, the number of different pulse shapes increased with an increase in the number of pulses detected, although some cells did

show a conserved pulsing behaviour (**Fig 3.4.6**). Thus, much of the heterogeneity we observe in the shapes of individual pulses is a result of cell-intrinsic differences in protein complement, and could also be influenced by differences in cell cycle position and various unidentified sources of noise, both technical and biochemical in nature.

4.1.6 ERK pulses decay across the cell cycle

ES cells have a shortened cell cycle, and undergo division approximately once every 12 - 14 h. To study the effects of cell cycle state on ERK pulse dynamics, I designed long-term experiments stretching over 19 h during which I continuously imaged the cells. These results demonstrated that ERK pulses were more frequent in the 7 h immediately after cell birth than in later times closer to the next cell division. This difference in ERK pulsing indicates one of two possibilities. First, differences in pulse dynamics could indicate that the system of feedbacks which give rise to ERK pulses moves to a slightly different regime without resulting in any meaningful changes in the way cells perceive an FGF stimulus. Alternatively, the reduction in pulsing across the cell cycle could indicate a difference in signal sensing by cells, either due to a reduction in the ability of FGF to activate MAPK signalling, or due to a qualitative change in the types of FGF/ERK targets that are activated. Although I did not use any cell-cycle staging system, since the length of the G1 phase in ESCs has been estimated to be around 1.5 h (ter Huurne et al., 2017), I can broadly separate early from late cell cycle as the cells were followed from birth to division. What could be the significance of cell-cycle associated differences in signal sensing? Recent work in mESCs has shown that cells in G1 respond to differentiation cues more readily (Chaigne et al., 2020). Previous work in human pluripotent stem cells (PSCs) has also demonstrated that G1 PSCs respond to differentiation signals (Pauklin & Vallier, 2013; Singh et al., 2013). Thus, pluripotent cells in general show a higher sensitivity to differentiation cues in G1 compared to other cell cycle phases. As cell cycle

proteins also regulate self-renewal genes (Yang et al., 2011), this temporal segregation of signalling cues might reflect different underlying mechanistic requirements for differentiation and self-renewal (Reviewed in Julian et al., 2016), or alternatively provide a means for temporal compartmentalization of signalling cues (Levine et al., 2013).

The combination of a limited window of signal sensitivity, coupled with natural variations in cell cycle length and the resultant distribution of cell cycle start times, results in cell type proportioning in some systems (Gruenheit et al., 2018). Proportioning of the inner cell mass (from which ES cells are derived) into primitive endoderm and epiblast cell types is a critical process during preimplantation development in mouse embryos that is controlled by FGF4. This process of fate allocation is thought to occur incrementally over a period of ~24 h (Saiz et al., 2016; Morris et al., 2010), and thus a proportioning mechanism based on temporal differences in signal sensitivity might be at play for establishing the initial heterogeneity in epiblast and primitive endoderm cells *in vivo*.

4.1.7 Conclusions and future directions

It is notable that most studies that have shown pulsatile ERK activity have been carried out in epithelial cells of various origins (Table T 4). This suggests that there may be something unique about epithelial cell types that parameterizes the RTK/ERK signalling network to generate dynamic ERK responses (Table T 4). Different dynamics might be tuned for optimal expression of cell-type specific genes (Wilson et al., 2017). Thus, cell-type specific dynamics (Goglia et al., 2020; Behar & Hoffmann, 2010) could allow the same effector, ERK, to elicit distinct context-dependent responses. As the distinctly faster dynamics we observe in this study occur in pluripotent stem cells (PSCs), they might be a further extension of this idea, allowing efficient transcription of genes related to differentiation or self-renewal.

Differentiating these PSCs to other fates where ERK signalling drives distinct gene expression patterns will be required to address this question.

Previous work in yeast has shown that cells can encode information in the 'phasing' differences between the dynamics of two transcription factors Msn2 and Mig1 (Lin et al., 2015). As the work in this thesis extensively characterises a single reporter for ERK, a limitation is that we do not collect information about other possibly dynamic kinases that can be stimulated by FGFR activity such as Akt (Reviewed in Mossahebi-Mohammadi et al., 2020). A future extension where multiple reporters are simultaneously observed in order to study whether 'phasing' relationships could enable more reliable information about growth factor concentration could be a fruitful direction of study.

What could be the molecular circuit that drives this dynamic behaviour? While in some cases a requirement for *de novo* protein synthesis has been demonstrated (Reviewed in Purvis & Lahav, 2013), the short timescales reported here precludes this. Indeed as Sparta et al., 2015 show, feedbacks could be mediated at the receptor level. However, extensive literature on feedbacks in MAPK signalling suggests that feedbacks from ERK to Raf are crucial for determining the dynamic response of ERK (Reviewed in Lake et al., 2016; Lavoie & Therrien, 2015). B-Raf inhibitors have also been shown to modulate ERK dynamics (Goglia et al., 2020; Aoki et al., 2013), and therefore this feedback link could be one additional candidate mechanism to test in the future.

5 References

Albeck JG, Mills GB, Brugge JS. 2013. Frequency-modulated pulses of ERK activity transmit quantitative proliferation signals. *Mol Cell* **49**:249–261.

Alberts B, Johnson A, Lewis J, Raff M, Roberts K, Walter P. 2002. Cell CommunicationMolecular Biology of the Cell. Garland Science. pp. 72–79.

Antebi YE, Nandagopal N, Elowitz MB. 2017. An operational view of intercellular signaling pathways. *Curr Opin Syst Biol*.

Aoki K, Kondo Y, Naoki H, Hiratsuka T, Itoh RE, Matsuda M. 2017. Propagating Wave of ERK Activation Orients Collective Cell Migration. *Dev Cell* **43**:305-317.e5.

Aoki K, Kumagai Y, Sakurai A, Komatsu N, Fujita Y, Shionyu C, Matsuda M. 2013. Stochastic ERK Activation Induced by Noise and Cell-to-Cell Propagation Regulates Cell Density-Dependent Proliferation. *Mol Cell* **52**:529–540.

Aoki K, Matsuda M. 2009. Visualization of small GTPase activity with fluorescence resonance energy transfer-based biosensors. *Nat Protoc* **4**:1623.

Ashall L, Horton C a, Nelson DE, Paszek P, Harper C V, Sillitoe K, Ryan S, Spiller DG, Unitt JF, Broomhead DS, Kell DB, Rand D a, Sée V, White MRH. 2009. Timing and Specificity of NF-kB – Dependent Transcription. *Science (80-)* **324**:242–246.

Behar M, Hoffmann A. 2010. Understanding the temporal codes of intra-cellular signals. *Curr Opin Genet Dev* **20**:684–693.

Belov AA, Mohammadi M. 2012. Grb2, a double-edged sword of receptor tyrosine kinase signaling. *Sci Signal* **5**:pe49.

Boroviak T, Loos R, Bertone P, Smith A, Nichols J. 2014. The ability of inner-cell-mass cells to self-renew as embryonic stem cells is acquired following epiblast specification. *Nat Cell Biol* **16**:513–525.

Böttcher RT, Niehrs C. 2005. Fibroblast growth factor signaling during early vertebrate development. *Endocr Rev* **26**:63–77.

Buscà R, Pouysségur J, Lenormand P. 2016. ERK1 and ERK2 Map Kinases: Specific Roles or Functional Redundancy? *Front cell Dev Biol* **4**:53.

Cai L, Dalal CK, Elowitz MB. 2008. Frequency-modulated nuclear localization bursts coordinate gene regulation. *Nature* **455**:485–90.

Chaigne A, Labouesse C, White IJ, Agnew M, Hannezo E, Chalut KJ, Paluch EK. 2020. Abscission Couples Cell Division to Embryonic Stem Cell Fate. *Dev Cell* **55**:195-208.e5.

Chazaud C, Yamanaka Y, Pawson T, Rossant J. 2006. Early Lineage Segregation between Epiblast and Primitive Endoderm in Mouse Blastocysts through the Grb2-MAPK Pathway. *Dev Cell* **10**:615–624.

Ciruna B, Rossant J. 2001. FGF Signaling Regulates Mesoderm Cell Fate Specification and Morphogenetic Movement at the Primitive Streak. *Dev Cell* **1**:37–49.

Corbalan-Garcia S, Yang SS, Degenhardt KR, Bar-Sagi D. 1996. Identification of the mitogen-activated protein kinase phosphorylation sites on human Sos1 that regulate interaction with Grb2. *Mol Cell Biol* **16**:5674–5682.

Cutrale F, Trivedi V, Trinh LA, Chiu C-L, Choi JM, Artiga MS, Fraser SE. 2017. Hyperspectral phasor analysis enables multiplexed 5D in vivo imaging. *Nat Methods* **14**:149–152.

de la Cova C, Townley R, Regot S, Greenwald I. 2017. A Real-Time Biosensor for ERK Activity Reveals Signaling Dynamics during C. elegans Cell Fate Specification. *Dev Cell* **42**:542-553.e4.

Deathridge J, Antolović V, Parsons M, Chubb JR. 2019. Live imaging of ERK signalling dynamics in differentiating mouse embryonic stem cells. *Development* **146**:dev172940.

Diez del Corral R, Morales A V. 2017. The multiple roles of FGF signaling in the developing spinal cord. *Front cell Dev Biol* **5**:58.

Douville E, Downward J. 1997. EGF induced SOS phosphorylation in PC12 cells involves P90 RSK-2. *Oncogene* **15**:373–383.

Ebisuya M, Kondoh K, Nishida E. 2005. The duration, magnitude and compartmentalization of ERK MAP kinase activity: mechanisms for providing signaling specificity. *J Cell Sci* **118**:2997–3002.

Eblen ST. 2018. Extracellular-regulated kinases: signaling from Ras to ERK substrates to control biological outcomes. *Adv Cancer Res* **138**:99–142.

Etoc F, Metzger J, Ruzo A, Kirst C, Yoney A, Ozair MZ, Brivanlou AH, Siggia ED. 2016. A Balance between Secreted Inhibitors and Edge Sensing Controls Gastruloid Self-Organization. *Dev Cell* **39**:302–315.

Fukuchi-Shimogori T, Grove EA. 2001. Neocortex patterning by the secreted signaling molecute FGF8. *Science (80-)* **294**:1071–1074.

Geva-Zatorsky N, Rosenfeld N, Itzkovitz S, Milo R, Sigal A, Dekel E, Yarnitzky T, Liron Y, Polak P, Lahav G, Alon U. 2006. Oscillations and variability in the p53 system. *Mol Syst Biol* **2**:2006.0033.

Goglia AG, Wilson MZ, Jena SG, Silbert J, Basta LP, Devenport D, Toettcher JE. 2020. A Live-Cell Screen for Altered Erk Dynamics Reveals Principles of Proliferative Control. *Cell Syst* **10**:240-253.e6.

Göke J, Chan Y-S, Yan J, Vingron M, Ng H-H. 2013. Genome-wide kinase-chromatin

interactions reveal the regulatory network of ERK signaling in human embryonic stem cells. *Mol Cell* **50**:844–855.

Goldsmith ZG, Dhanasekaran DN. 2007. G Protein regulation of MAPK networks. *Oncogene* **26**:3122–3142.

Gonzalez FA, Raden DL, Davis RJ. 1991. Identification of substrate recognition determinants for human ERK1 and ERK2 protein kinases. *J Biol Chem* **266**:22159–22163.

Gruenheit N, Parkinson K, Brimson CA, Kuwana S, Johnson EJ, Nagayama K, Llewellyn J, Salvidge WM, Stewart B, Keller T, van Zon W, Cotter SL, Thompson CRL. 2018. Cell Cycle Heterogeneity Can Generate Robust Cell Type Proportioning. *Dev Cell* **47**:494-508.e4.

Gut G, Herrmann MD, Pelkmans L. 2018. Multiplexed protein maps link subcellular organization to cellular states. *Science (80-)* **361**.

Hatano N, Mori Y, Oh-hora M, Kosugi A, Fujikawa T, Nakai N, Niwa H, Miyazaki J, Hamaoka T, Ogata M. 2003. Essential role for ERK2 mitogen-activated protein kinase in placental development. *Genes to Cells* **8**:847–856.

Hiratsuka T, Fujita Y, Naoki H, Aoki K, Kamioka Y, Matsuda M. 2015. Intercellular propagation of extracellular signal-regulated kinase activation revealed by in vivo imaging of mouse skin. *Elife* **2015**:1–18.

Hoffmann A, Levchenko A, Scott ML, Baltimore D. 2002. The IκB-NF-κB Signaling Module: Temporal Control and Selective Gene Activation. *Science (80-)* **298**:1241 LP – 1245.

Itoh N, Ornitz DM. 2008. Functional evolutionary history of the mouseFgf gene family. *Dev Dyn* **237**:18–27.

Julian LM, Carpenedo RL, Rothberg JLM, Stanford WL. 2016. Formula G1: Cell cycle in the driver's seat of stem cell fate determination. *BioEssays* **38**:325–332.

Kang M, Garg V, Hadjantonakis A-KK. 2017. Lineage Establishment and Progression within the Inner Cell Mass of the Mouse Blastocyst Requires FGFR1 and FGFR2. *Dev Cell* **41**:496-510.e5.

Kang M, Piliszek A, Artus J, Hadjantonakis A-K. 2013. FGF4 is required for lineage restriction and salt-and-pepper distribution of primitive endoderm factors but not their initial expression in the mouse. *Development* **140**:267–79.

Keller G. 2005. Embryonic stem cell differentiation: Emergence of a new era in biology and medicine. *Genes Dev* **19**:1129–1155.

Kholodenko BN. 2009. Spatially distributed cell signalling. *FEBS Lett* **583**:4006–4012.

Kim Y, Paroush Z, Nairz K, Hafen E, Jiménez G, Shvartsman SY. 2011. Substrate-dependent control of MAPK phosphorylation in vivo. *Mol Syst Biol* **7**:467.

Kitano H. 2004. Biological robustness. *Nat Rev Genet* **5**:826–837.

Komatsu N, Aoki K, Yamada M, Yukinaga H, Fujita Y, Kamioka Y, Matsuda M. 2011. Development of an optimized backbone of FRET biosensors for kinases and GTPases. *Mol Biol Cell* **22**:4647–4656.

Kouhara H, Hadari YR, Spivak-Kroizman T, Schilling J, Bar-Sagi D, Lax I, Schlessinger J. 1997. A lipid-anchored Grb2-binding protein that links FGF-receptor activation to the Ras/MAPK signaling pathway. *Cell* **89**:693–702.

Kramer BA, Pelkmans L. 2019. Cellular state determines the multimodal signaling response of single cells. *bioRxiv*.

Kunath T, Saba-El-Leil MK, Almousailleakh M, Wray J, Meloche S, Smith A. 2007. FGF stimulation of the Erk1/2 signalling cascade triggers transition of pluripotent embryonic stem cells from self-renewal to lineage commitment. *Development* **134**:2895–902.

Lahav G, Rosenfeld N, Sigal A, Geva-Zatorsky N, Levine AJ, Elowitz MB, Alon U. 2004. Dynamics of the p53-Mdm2 feedback loop in individual cells. *Nat Genet* **36**:147–150.

Lake D, Corrêa SAL, Müller J. 2016. Negative feedback regulation of the ERK1/2 MAPK pathway. *Cell Mol Life Sci* **73**:4397–4413.

Lavoie H, Gagnon J, Therrien M. 2020. ERK signalling: a master regulator of cell behaviour, life and fate. *Nat Rev Mol Cell Biol* **21**:607–632.

Lavoie H, Therrien M. 2015. Regulation of RAF protein kinases in ERK signalling. *Nat Rev Mol Cell Biol* **16**:281–298.

Leitch HG, McEwen KR, Turp A, Encheva V, Carroll T, Grabole N, Mansfield W, Nashun B, Knezovich JG, Smith A. 2013. Naive pluripotency is associated with global DNA hypomethylation. *Nat Struct Mol Biol* **20**:311.

Levine JH, Lin Y, Elowitz MB. 2013. Functional roles of pulsing in genetic circuits. *Science (80-)* **342**:1193–1200.

Lin Y, Sohn CH, Dalal CK, Cai L, Elowitz MB. 2015. Combinatorial gene regulation by modulation of relative pulse timing. *Nature* **527**:54–58.

Marshall CJ. 1995. Specificity of receptor tyrosine kinase signaling: Transient versus sustained extracellular signal-regulated kinase activation. *Cell*.

Martello G, Smith A. 2014. The Nature of Embryonic Stem Cells. *Annu Rev Cell Dev Biol* **30**:647–675.

Mayr V, Sturtzel C, Stadler M, Grissenberger S, Distel M. 2018. Fast dynamic in vivo monitoring of Erk activity at single cell resolution in DREKA zebrafish. *Front Cell Dev Biol* **6**:111.

Molotkov A, Mazot P, Brewer JR, Cinalli RM, Soriano P. 2017. Distinct Requirements for FGFR1 and FGFR2 in Primitive Endoderm Development and Exit from Pluripotency. *Dev Cell* **41**:511-526.e4.

Mönke G, Cristiano E, Finzel A, Friedrich D, Herzel H, Falcke M, Loewer A. 2017. Excitability in the p53 network mediates robust signaling with tunable activation thresholds in single cells. *Sci Rep* **7**:46571.

Morgani SM, Saiz N, Garg V, Raina D, Simon CS Kang M, Arias AM, Nichols J, Schröter C, Hadjantonakis A-KA-K. 2018. A Sprouty4 reporter to monitor FGF/ERK signaling activity in ESCs and mice. *Dev Biol* **441**:104–126.

Morris SA, Teo RTY, Li H, Robson P, Glover DM, Zernicka-Goetz M. 2010. Origin and formation of the first two distinct cell types of the inner cell mass in the mouse embryo. *Proc Natl Acad Sci U S A* **107**:6364–6369.

Morrison DK. 2012. MAP kinase pathways. *Cold Spring Harb Perspect Biol* **4**:a011254.

Mossahebi-Mohammadi M, Quan M, Zhang JS, Li X. 2020. FGF Signaling Pathway: A Key Regulator of Stem Cell Pluripotency. *Front Cell Dev Biol* **8**:79.

Nett IR, Mulas C, Gatto L, Lilley KS, Smith A. 2018. Negative feedback via RSK modulates Erk-dependent progression from naïve pluripotency. *EMBO Rep* **19**:1–15.

Nichols J, Smith A. 2009. Naive and Primed Pluripotent States. *Cell Stem Cell* **4**:487–492.

Niwa H, Ogawa K, Shimosato D, Adachi K. 2009. A parallel circuit of LIF signalling pathways maintains pluripotency of mouse ES cells. *Nature* **460**:118–22.

Novák B, Tyson JJ. 2008. Design principles of biochemical oscillators. *Nat Rev Mol Cell Biol* **9**:981–991.

Ornitz DM, Itoh N. 2015. The fibroblast growth factor signaling pathway. *Wiley Interdiscip Rev Dev Biol* **4**:215–266.

Pagès G, Guérin S, Grall D, Bonino F, Smith A, Anjuere F, Auberger P, Pouysségur J. 1999. Defective Thymocyte Maturation in p44 MAP Kinase (Erk 1) Knockout Mice. *Science (80-)* **286**:1374 LP – 1377.

Pauklin S, Vallier L. 2013. The Cell-Cycle State of Stem Cells Determines Cell Fate Propensity. *Cell* **155**:135–147.

Pellegrini L, Burke DF, Von Delft F, Mulloy B, Blundell TL. 2000. Crystal structure of fibroblast growth factor receptor ectodomain bound to ligand and heparin. *Nature* **407**:1029–1034.

Pokrass MJ, Ryan KA, Xin T, Pielstick B, Timp W, Greco V, Regot S. 2020. Cell-Cycle-Dependent ERK Signaling Dynamics Direct Fate Specification in the Mammalian Preimplantation Embryo. *Dev Cell* **55**:1–13.

Purba E, Saita E, Maruyama I. 2017. Activation of the EGF Receptor by Ligand Binding and Oncogenic Mutations: The "Rotation Model." *Cells* **6**:13.

Purvis JE, Karhohs KW, Mock C, Batchelor E, Loewer A, Lahav G. 2012. p53 dynamics control cell fate. *Science (80-)* **336**:1440–1444.

Purvis JEE, Lahav G. 2013. Encoding and decoding cellular information through signaling dynamics. *Cell* **152**:945–956.

Raina D, Fabris F, Morelli LG, Schröter C. 2020a. Intermittent ERK oscillations downstream of FGF in mouse embryonic stem cells. *bioRxiv*.

Raina D, Stanoev A, Bahadori A, Protzek M, Koseska A, Schröter C. 2020b. Cell-cell communication through FGF4 generates and maintains robust proportions of differentiated cell fates in embryonic stem cells. *bioRxiv*.

Regot S, Hughey JJ, Bajar BT, Carrasco S, Covert MW. 2014. Resource High-Sensitivity Measurements of Multiple Kinase Activities in Live Single Cells. *Cell* **157**:1724–1734.

Robbins DJ, Zhen E, Owaki H, Vanderbilt CA, Ebert D, Geppert TD, Cobb MH. 1993. Regulation and properties of extracellular signal-regulated protein kinases 1 and 2 in vitro. *J Biol Chem* **268**:5097–5106.

Rueden CT, Schindelin J, Hiner MC, DeZonia BE, Walter AE, Arena ET, Eliceiri KW. 2017. ImageJ2: ImageJ for the next generation of scientific image data. *BMC Bioinformatics* **18**:1–26.

Saiz N, Williams KM, Seshan VE, Hadjantonakis A-K. 2016. Asynchronous fate decisions by single cells collectively ensure consistent lineage composition in the mouse blastocyst. *Nat Commun* **7**:13463.

Santos SDM, Verveer PJ, Bastiaens PIH. 2007. Growth factor-induced MAPK network topology shapes Erk response determining PC-12 cell fate. *Nat Cell Biol* **9**:324–330.

Schlaepfer DD, Broome MA, Hunter T. 1997. Fibronectin-stimulated signaling from a focal adhesion kinase-c-Src complex: involvement of the Grb2, p130cas, and Nck adaptor proteins. *Mol Cell Biol* **17**:1702–1713.

Schlessinger J, Plotnikov AN, Ibrahimi OA, Eliseenkova A V., Yeh BK, Yayon A, Linhardt RJ, Mohammadi M. 2000. Crystal structure of a ternary FGF-FGFR-heparin complex reveals a dual role for heparin in FGFR binding and dimerization. *Mol Cell* **6**:743–750.

Selimkhanov J, Taylor B, Yao J, Pilko A, Albeck J, Hoffmann A, Tsimring L, Wollman R. 2014. Accurate information transmission through dynamic biochemical signaling networks. *Science* **346**:1370–3.

Shankaran H, Ippolito DL, Chrisler WB, Resat H, Bollinger N, Opresko LK, Wiley HS. 2009. Rapid and sustained nuclear-cytoplasmic ERK oscillations induced by epidermal growth factor. *Mol Syst Biol* **5**:332.

Simon CS, Rahman S, Raina D, Schröter C, Hadjantonakis A-K. 2020. Live Visualization of ERK Activity in the Mouse Blastocyst Reveals Lineage-Specific Signaling Dynamics. *Dev Cell* **55**:1–13.

Singh AM, Chappell J, Trost R, Lin L, Wang T, Tang J, Wu H, Zhao S, Jin P, Dalton S. 2013. Cell-Cycle Control of Developmentally Regulated Transcription Factors Accounts for Heterogeneity in Human Pluripotent Cells. *Stem Cell Reports* **1**:532–544.

Sparta B, Pargett M, Minguet M, Distor K, Bell G, Albeck JG. 2015. Receptor level mechanisms are required for epidermal growth factor (EGF)-stimulated extracellular signal-regulated kinase (ERK) activity pulses. *J Biol Chem* **290**:24784–24792.

Sun X, Meyers EN, Lewandoski M, Martin GR. 1999. Targeted disruption of Fgf8 causes failure of cell migration in the gastrulating mouse embryo. *Genes Dev* **13**:1834–1846.

Tay S, Hughey JJ, Lee TK, Lipniacki T, Quake SR, Covert MW. 2010. Single-cell NF-κB dynamics reveal digital activation and analogue information processing. *Nature* **466**:267–271.

Tee WW, Shen SS, Oksuz O, Narendra V, Reinberg D. 2014. Erk1/2 activity promotes chromatin features and RNAPII phosphorylation at developmental promoters in mouse ESCs. *Cell* **156**:678–690.

ter Huurne M, Chappell J, Dalton S, Stunnenberg HG. 2017. Distinct Cell-Cycle Control in Two Different States of Mouse Pluripotency. *Cell Stem Cell* **21**:449-455.e4.

Terrell EM, Morrison DK. 2019. Ras-Mediated Activation of the Raf Family Kinases. *Cold Spring Harb Perspect Med* **9**.

Tinevez J, Perry N, Schindelin J, Hoopes GM, Reynolds GD, Laplantine E, Bednarek SY, Shorte SL, Eliceiri KW. 2017. TrackMate: An open and extensible platform for single-particle tracking. *Methods* **115**:80–90.

Tsai TYC, Yoon SC, Ma W, Pomerening JR, Tang C, Ferrell JE. 2008. Robust, tunable biological oscillations from interlinked positive and negative feedback loops. *Science (80-)* **321**:126–139.

Tyson JJ, Chen KC, Novak B. 2003. Sniffers, buzzers, toggles and blinkers: Dynamics of regulatory and signaling pathways in the cell. *Curr Opin Cell Biol* **15**:221–231.

Ünal EB, Uhlitz F, Blüthgen N. 2017. A compendium of ERK targets. *FEBS Lett* **591**:2607–2615.

Vantaggiato C, Formentini I, Bondanza A, Bonini C, Naldini L, Brambilla R. 2006. ERK1 and ERK2 mitogen-activated protein kinases affect Ras-dependent cell signaling differentially. *J Biol* **5**:1–15.

Vartak N, Bastiaens P. 2010. Spatial cycles in G-protein crowd control. *EMBO J* **29**:2689–2699.

Wiesmann C, Ultsch MH, Bass SH, De Vos AM. 1999. Crystal structure of nerve

growth factor in complex with the ligand- binding domain of the TrkA receptor. *Nature* **401**:184–188.

Williams RL, Hilton DJ, Pease S, Willson TA, Stewart CL, Gearing DP, Wagner EF, Metcalf D, Nicola NA, Gough NM. 1988. Myeloid leukaemia inhibitory factor maintains the developmental potential of embryonic stem cells. *Nature* **336**:684–687.

Wilson MZ, Ravindran PT, Lim WA, Toettcher JE. 2017. Tracing Information Flow from Erk to Target Gene Induction Reveals Mechanisms of Dynamic and Combinatorial Control. *Mol Cell* **67**:757-769.e5.

Yamaguchi TP, Harpal K, Henkemeyer M, Rossant J. 1994. Fgfr-1 Is Required for Embryonic Growth and Mesodermal Patterning During Mouse Gastrulation. *Genes Dev* **8**:3032–3044.

Yang SH, Sharrocks AD, Whitmarsh AJ. 2003. Transcriptional regulation by the MAP kinase signaling cascades. *Gene* **320**:3–21.

Yang VS, Carter SA, Hyland SJ, Tachibana-Konwalski K, Laskey RA, Gonzalez MA. 2011. Geminin Escapes degradation in G1 of mouse pluripotent cells and mediates the expression of Oct4, Sox2, and Nanog. *Curr Biol* **21**:692–699.

Ying Q-L, Nichols J, Chambers I, Smith A. 2003. BMP Induction of Id Proteins Suppresses Differentiation and Sustains Embryonic Stem Cell Self-Renewal in Collaboration with STAT3. *Cell* **115**:281–292.

Ying Q-L, Ying Q-L, Wray J, Wray J, Nichols J, Nichols J, Batlle-Morera L, Batlle-Morera L, Doble B, Doble B, Woodgett J, Woodgett J, Cohen P, Cohen P, Smith A, Smith A. 2008. The ground state of embryonic stem cell self-renewal. *Nature* **453**:519–23.

Young JW, Locke JCW, Elowitz MB. 2013. Rate of environmental change determines stress response specificity. *Proc Natl Acad Sci* **110**:4140 LP – 4145.

Yuzawa S, Opatowsky Y, Zhang Z, Mandiyan V, Lax I, Schlessinger J. 2007. Structural Basis for Activation of the Receptor Tyrosine Kinase KIT by Stem Cell Factor. *Cell* **130**:323–334.

Zakrzewska M, Haugsten EM, Nadratowska-Wesolowska B, Oppelt A, Hausott B, Jin Y, Otlewski J, Wesche J, Wiedlocha A. 2013. ERK-mediated phosphorylation of fibroblast growth factor receptor 1 on Ser777 inhibits signaling. *Sci Signal* **6**.

Zhang YE. 2009. Non-Smad pathways in TGF-beta signaling. *Cell Res* **19**:128–139.

6 Appendix – Tables

Table T 1: Measured timescales of ERK dynamics

'IPI' and 'Pulse width' values for the first 5 rows are (μ±S.D) from GMM fit estimates, and median values for all remaining rows. Median values are printed for 'Pulse frequency', 'Max windowed pulse rate', and 'Pulse likelihood' for all rows. Where possible, values are compared with values obtained by alternate analysis methods published in Raina et al., 2020a. Pulse width estimated in this thesis is approximately 0.55 times the true pulse width, and should be adjusted accordingly before comparison.

Experimental condition		**IPI (min)**		**Pulse width (min)**		**Pulse freq. (hr^{-1})**		**Max pulse rate (hr^{-1})**	**Fraction of clustered pulses**
		this thesis	*Raina & Fabris et al 2021*	*this thesis*	*Raina & Fabris et al 2021*	*this thesis*	*Raina & Fabris et al 2021*		
S+L (serum containing)		6.7±1.2 12.9±3.9	7.67	3.5± 1.1	6.33	3.6	-	6	0.67
N2Ch (serum-free / paracrine only)		5.6±1.3 12.9±5.0	-	2.8±1.0	-	3.6	-	7	0.71
Steady-state stimulation N2Ch+ exogenous FGF4 (ng/mL)	2.5	6.4±1.2 11.7±3.1	6.67	3.5±1.2	6.33	2.1	~2.2	4	0.5
	5	6.5±1.4 14.2±5.4	6.67	3.2±0.9	6.33	3.5	~3.5	8	0.71
	20	6.2±1.2 12.7±4.5	6.67	3.0±0.9	5.67	3.6	~4.1	8	0.75
Transient stimulation N2Ch+ exogenous FGF4 (ng/mL)	2.5	-		14.0	-	-		2	-
	5			14.5				2	
	10			14.1				1	
	20			15.7				2	

Table T 2: Gaussian Mixture Model fits

μ1-3 refers to the mean of the fit of the fit components 1-3. σ1-3 refers to the standard deviation of the fit components 1-3. %data1-3 refers to the percentage of datapoints explained by each of the fit components 1-3.

Interpulse intervals (min)

Figure	Treatment	μ1	σ1	%data1	μ2	σ2	%data2	μ3	σ3	%data3	AIC	BIC
Fig 3.2.2	ESL	6.7	1.2	37	12.9	3.9	48	27.2	12.0	15	2076.4	2106.8
Fig 3.2.5	N2Ch	5.6	1.3	57	12.9	5.0	32	39.7	25.0	11	4209.8	4246.0
Fig 3.4.3	2.5 ng/mL FGF4	6.4	1.2	38	11.7	3.1	37	27.3	11.0	25	788.4	810.7
Fig 3.4.3	5 ng/mL FGF4	6.5	1.4	53	14.2	5.4	40	42.9	20.9	7	2198.2	2229.2
Fig 3.4.3	20 ng/mL FGF4	6.2	1.2	55	12.7	4.5	32	30.4	16.6	12	2717.2	2750.2

Pulse durations (min)

Figure	Treatment	μ1	σ1	%data1	μ2	σ2	%data2	AIC	BIC
Fig 3.2.2	ESL	3.5	1.1	91	8.2	3.6	9	1438.9	1458.9
Fig 3.2.5	N2Ch	2.8	1.0	87.6	8.9	6.5	12.4	2679.9	2702.9
Fig 3.4.3	2.5 ng/mL FGF4	3.5	1.2	92	12.1	9.4	8	635.1	650.6
Fig 3.4.3	5 ng/mL FGF4	3.2	0.9	91	8.3	5.1	9	1360.4	1380.5
Fig 3.4.3	20 ng/mL FGF4	3.0	0.9	91	8.0	4.3	9	1681.8	1703.1

Table T 3: phospho-ERK staining values

Whole-cell phospho-ERK immunostaining values used to construct **Fig 3.5.1b,c**. Raw intensity values are min-max normalised by setting the median value at 0 ng/mL to 0 and the median value at 20 ng/mL to 1.

	FGF concentration (ng/mL)				
	0	2.5	5	10	20
Replicate #1					
25th percentile	-0.18	-0.11	0.29	0.37	0.72
median	**0.00**	**0.08**	**0.59**	**0.67**	**1.00**
75th percentile	0.22	0.32	0.91	1.00	1.38
Replicate #2					
25th percentile	-0.04	0.19	0.51	0.43	0.67
median	**0.00**	**0.34**	**0.75**	**0.58**	**1.00**
75th percentile	0.05	0.64	1.06	0.85	1.40
Replicate #3					
25th percentile	-0.10	0.39	0.43	0.80	0.61
median	**0.00**	**0.64**	**0.86**	**1.22**	**1.00**
75th percentile	0.14	1.00	1.41	1.91	1.72

Table T 4: Summary of timescales reported in literature

Study	Sensor	Cell line / organism	Cell type	Pulse rate	Pulse width	Stimulation	Model	Notes
Shankaran 2009	ERK-GFP	HMEC 184A1	Mammary epithelial	~6 hr^{-1}	~10 min	EGF	ultrasensitivity + neg. feedback (Kholodenko 2000)	Pulse width doesn't change, but frequency does
Aoki 2013	EKAREV-NLS	MDCK; NRK-52E	Kidney epithelial; Kidney epithelial	~0.4 - 0.8 hr^{-1}	~ 20 min	Serum, cell density	neg. + pos. feedback	Pulse width doesn't change, but frequency does
Albeck 2013	EKAREV	MCF10A	Mammary epithelial	~0.5 - 1 hr^{-1} (not quantified in study)	~20 - 30 min (not quantified in study)	EGF	-	Low [EGF] induced 'bursts' of pulses; Pulse width doesn't change until high conc.
Hiratsuka 2015	EKAREV-NLS	Eisuke mice	Ear epithelial	-	~20-30 min	-	-	Propagating waves of ERK activity

Sparta 2015	EKAREV EKAR3 ERK-KTR	MCF10A	Mammary epithelial		~ 20 – 30 min (not quantified in study)	EGF	-	Acute EGFRi (gefitinib) immediately stops pulsing, suggesting that continuous signalling is required.
de la Cova, 2017	ERK-KTR	C.elegans	Epithelial, P6.p Vulval precursor cells	~ 3 hr^{-1}	~10 – 20 min (not quantified in study)	Endogenous EGF	-	Imaging at 2 min intervals
Aoki 2017	EKAREV-NLS	MDCK cysts	Canine kidney epithelial	-	~1 hr	Endogenous EGF	-	Cells migrate in the opposite direction to ERK wave
Wilson 2017	BFP-ERK	NIH-3T3		-	-	-	-	All under an ERK induction system
Meyr 2018	DREKA (KTR)	Zebrafish	Epithelial and muscle cells	-	-	-	-	Cells show a ~30 min pulse of ERK activity in response to tissue wound
Deathridge 2019	EKAREV	Mouse ESCs	Pluripotent stem cells	-	-	MEKi release	-	-

Goglia 2020	ERK-KTR	MCF 10A; Mouse	Mammary epithelial; Primary keratinocytes	0.5 hr^{-1} MCF10A; 1-2 h^{r-1} Keratinocyte (not quantified in study)	~1 hr MCF10A; ~30 min Keratinocytes (not quantified in study)	EGF	-	Performed a screen for inhibitors of ERK dynamics. bRaf inhibitors can alter ERK pulsing dynamics
Simon 2020	ERK-KTR	Mouse	Pluripotent cells	0 – 1 hr^{-1}	~10 - 20 min	Endogenous FGF	-	Imaging at 5 min intervals

7 Appendix – Complete cell tracks

For all tracks shown below, cells are maintained in the indicated medium conditions. Red inverted triangles represent identified peaks, and the number above a cell track corresponds to its identification number in the primary data. Cell tracks are sorted based on the number of peaks detected. Discontinous tracks represent cells tracked over a division event.

7.1 ERK-KTR cells in S+L

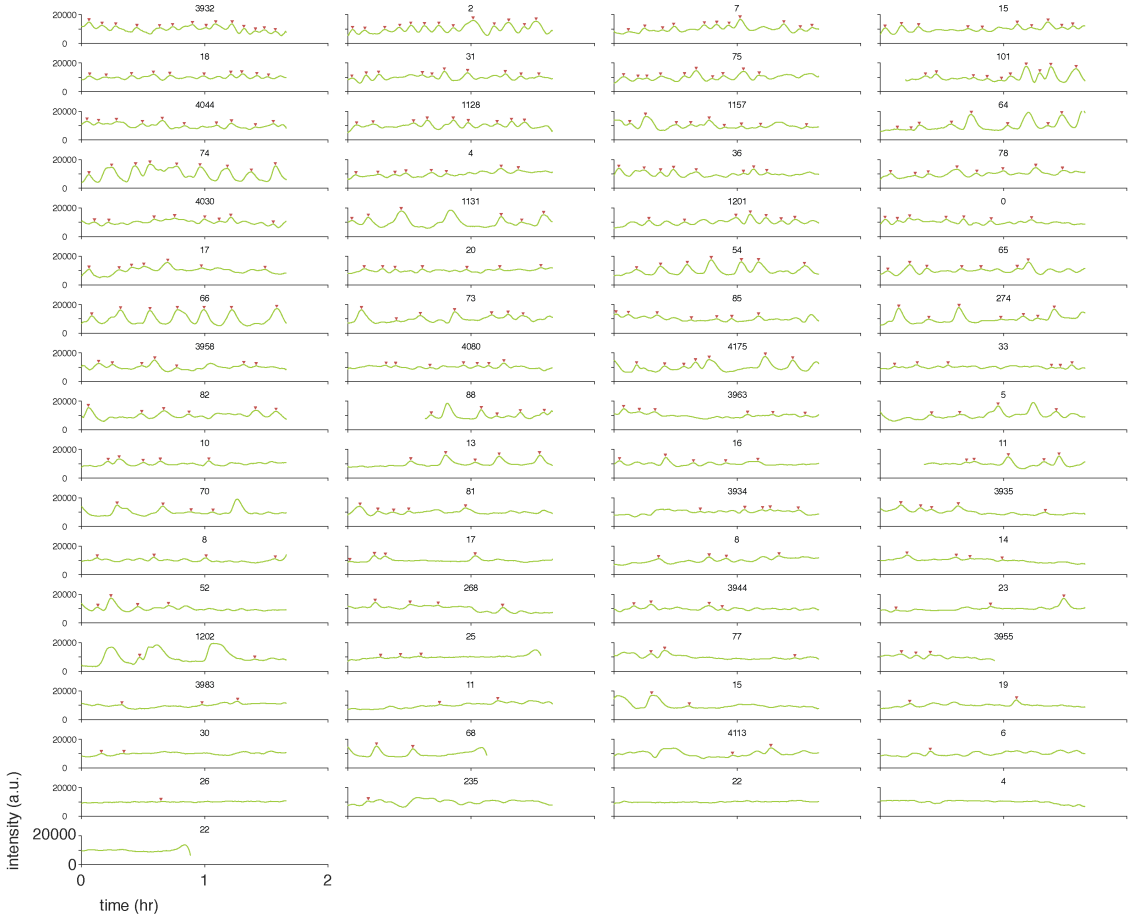

7.2 ERK-KTR cells in S+L+MEKi

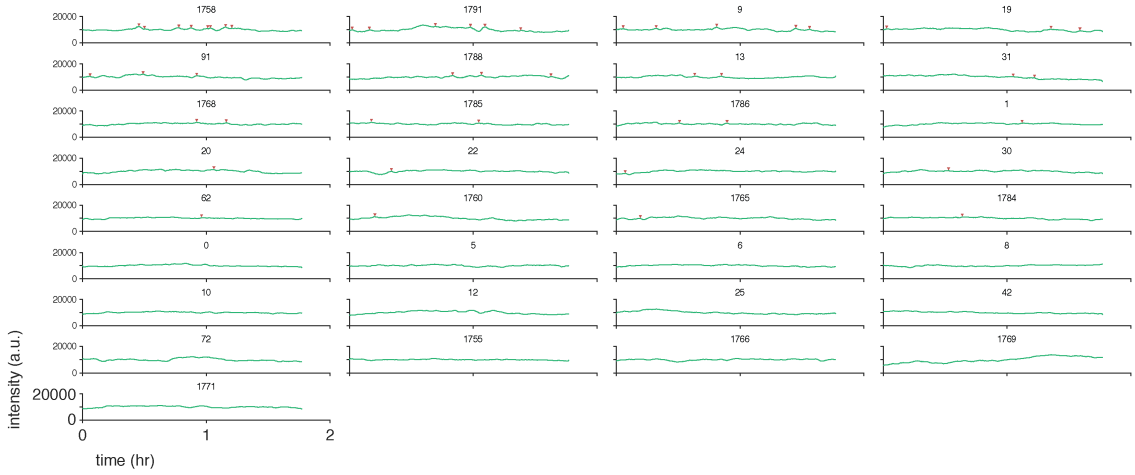

7.3 ERK-KTR cells in N2Ch

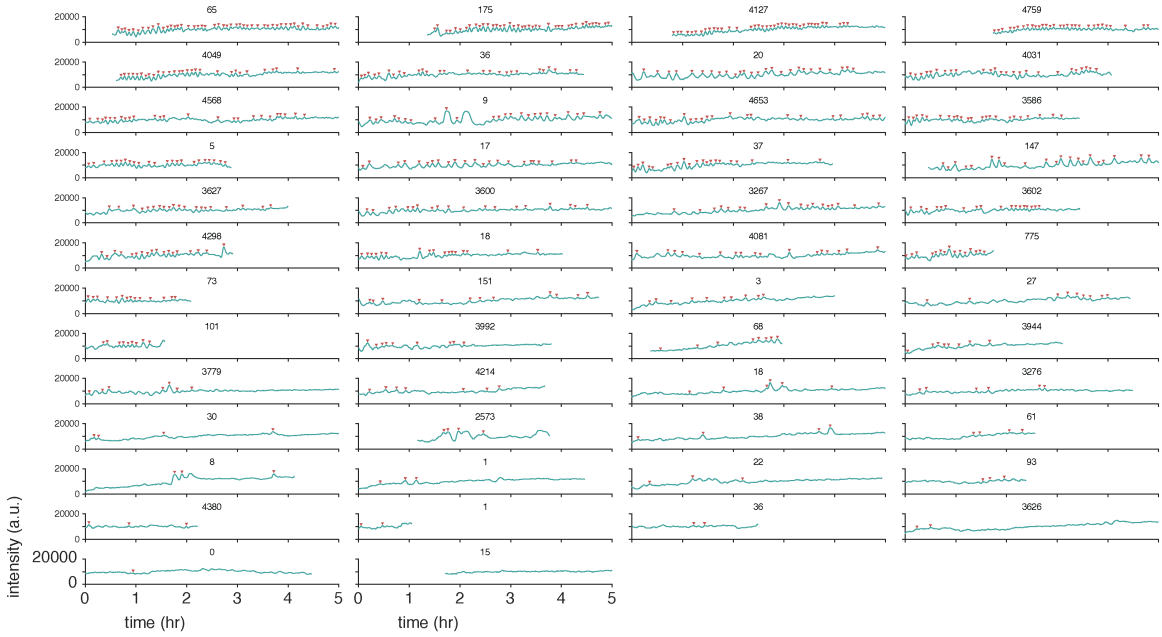

7.4 ERK-KTR cells in N2Ch+MEKi

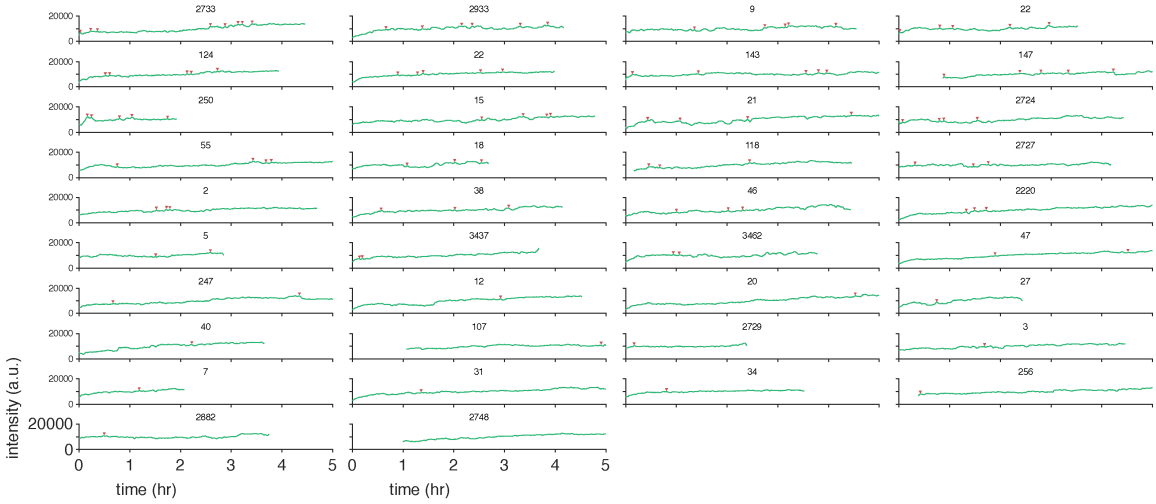

7.5 ERK-KTR *Fgf4* mutant cells in N2Ch + 0 ng/mL FGF4

7.6 ERK-KTR *Fgf4* mutant cells in N2Ch + 2.5 ng/mL FGF4

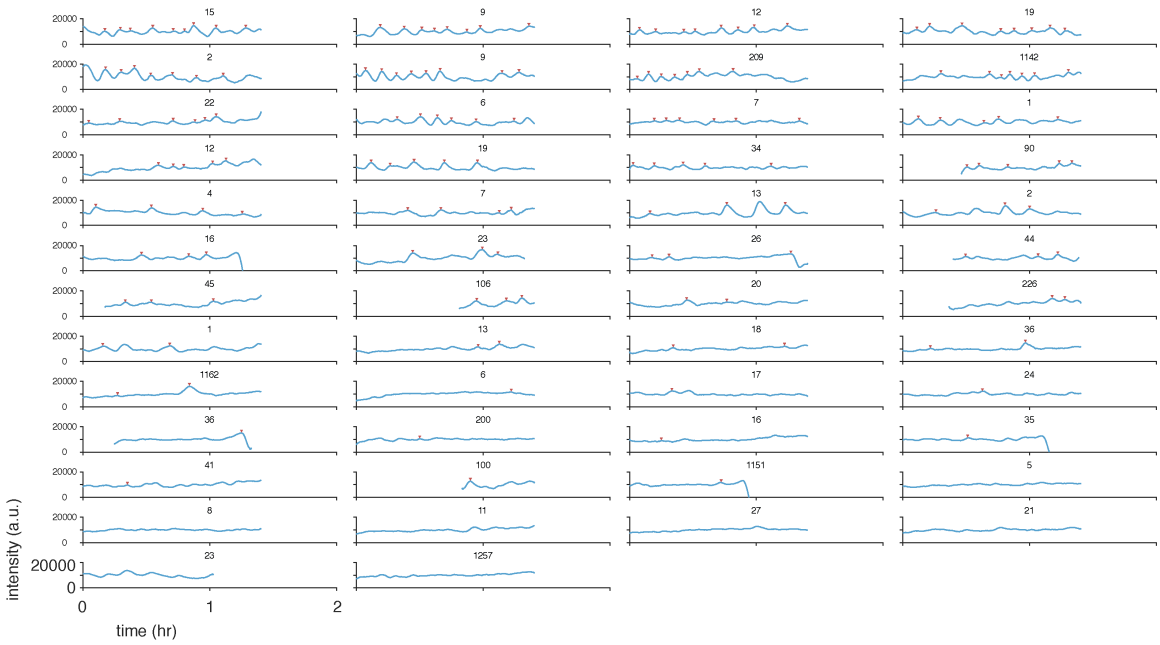

7.7 ERK-KTR *Fgf4* mutant cells in N2Ch + 5 ng/mL FGF4

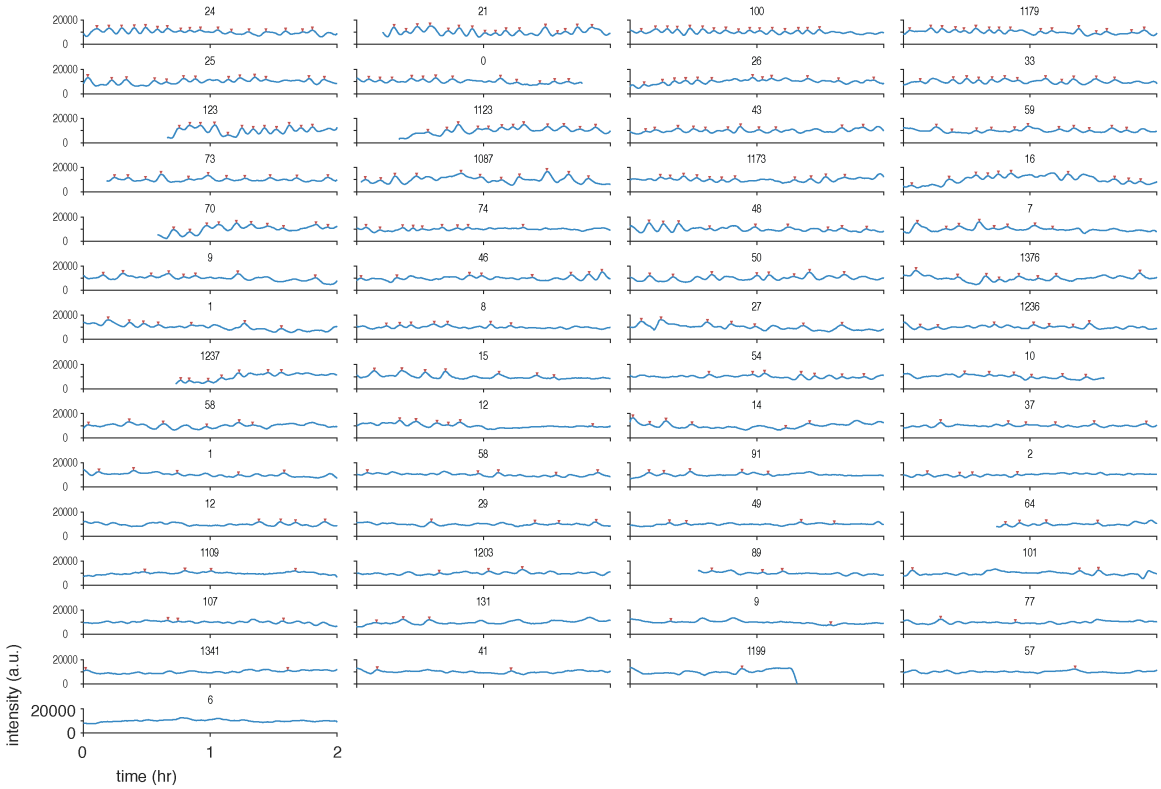

7.8 ERK-KTR *Fgf4* mutant cells in N2Ch + 20 ng/mL FGF4

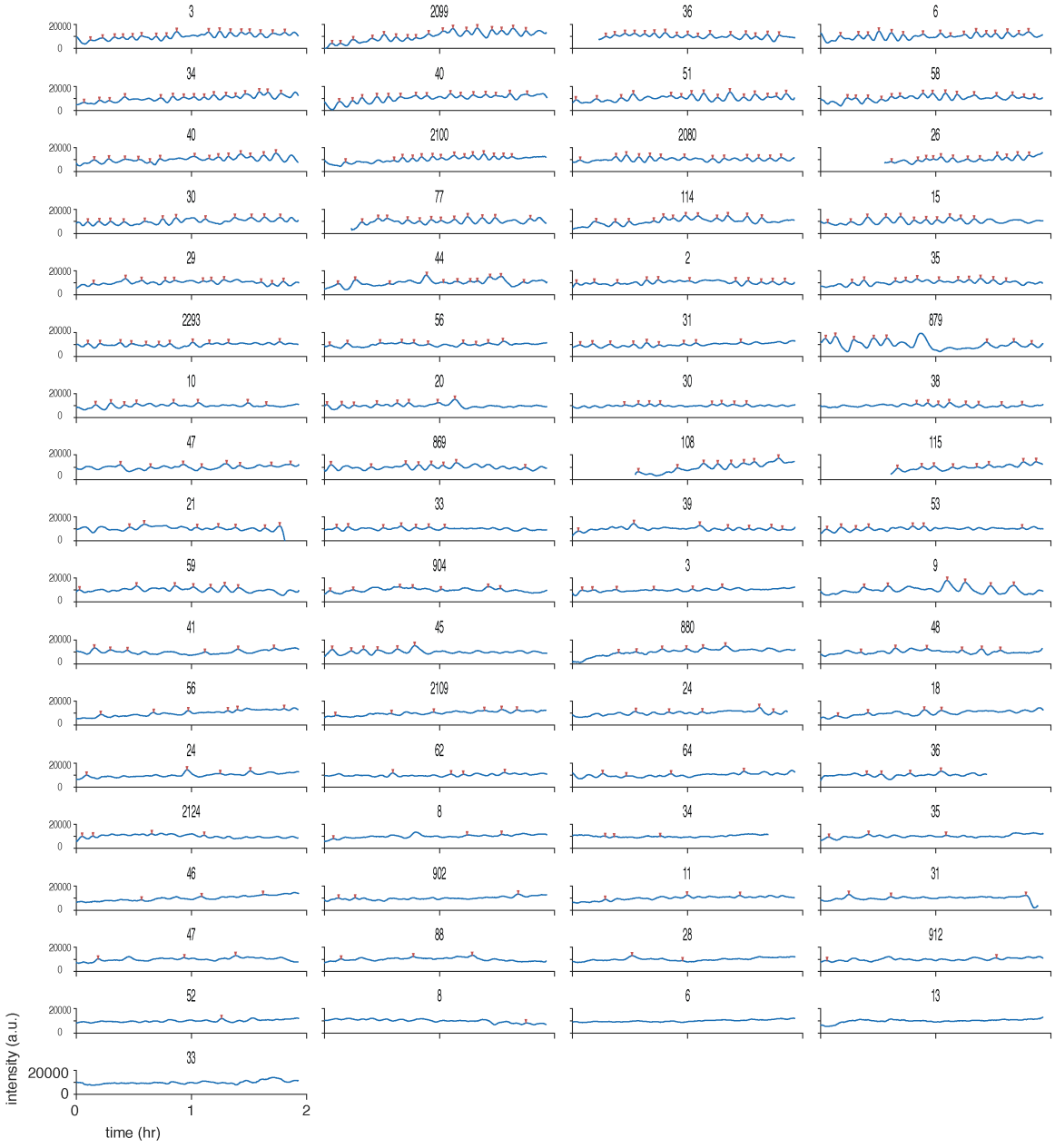

7.9 ERK-KTR *Fgf4* mutant cells after acute stimulation with 0 ng/mL FGF4

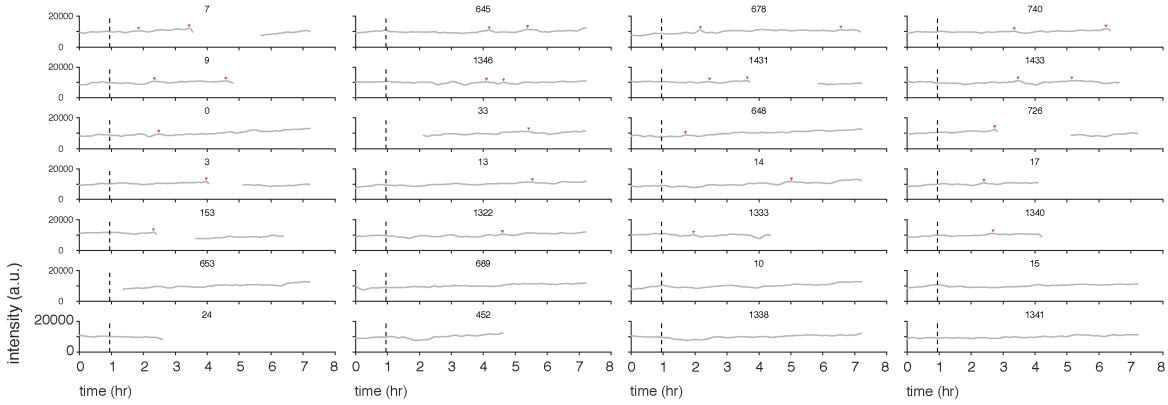

7.10 ERK-KTR Fgf4 mutant cells after acute stimulation with 2.5 ng/mL FGF4

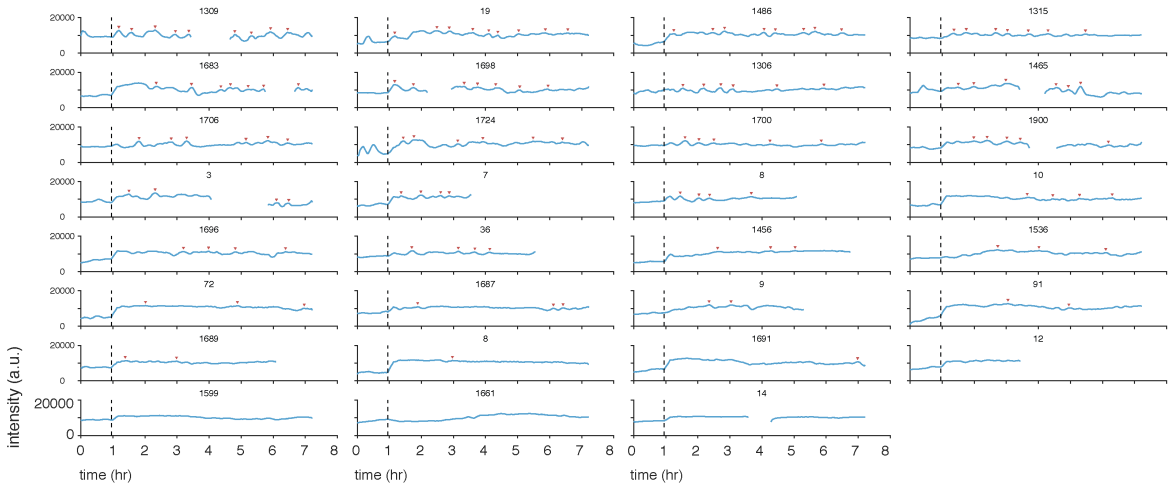

7.11 ERK-KTR *Fgf4* mutant cells after acute stimulation with 5 ng/mL FGF4

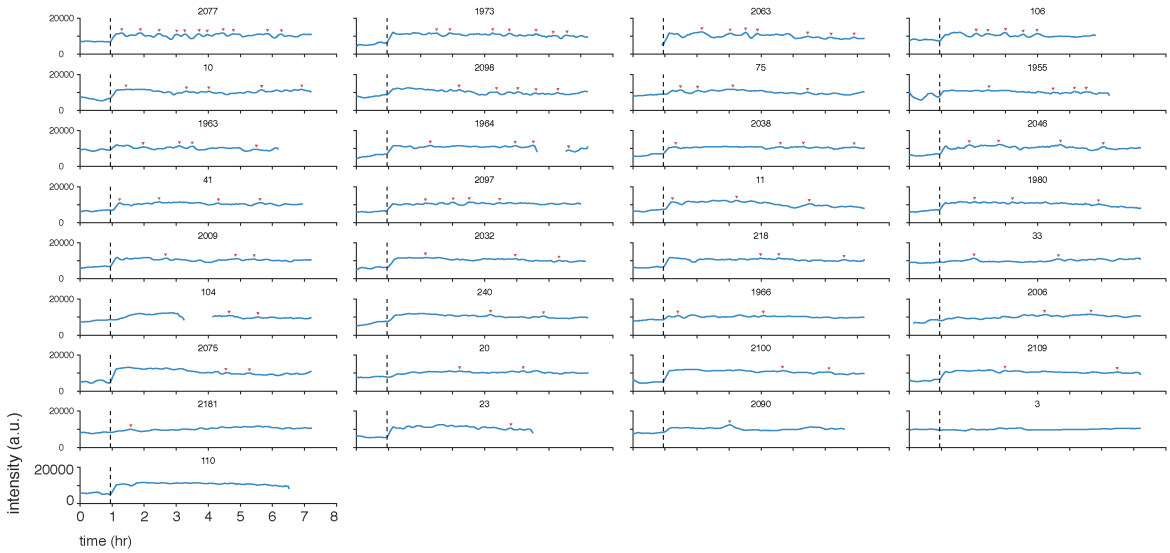

7.12 ERK-KTR *Fgf4* mutant cells after acute stimulation with 10 ng/mL FGF4

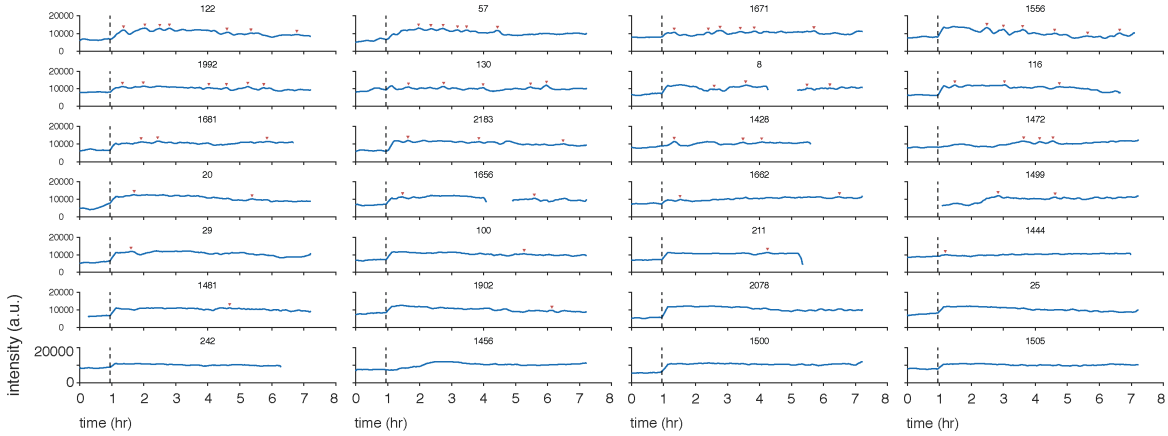

7.13 ERK-KTR *Fgf4* mutant cells after acute stimulation with 20 ng/mL FGF4